# FINDING ORDER IN CHAOS:

# RESONANT ORBITS AND POINCARÉ SECTIONS

A Thesis

Submitted to the Faculty

of

Purdue University

by

Maaninee Gupta

In Partial Fulfillment of the

Requirements for the Degree

of

Master of Science in Aeronautics and Astronautics

May 2020

Purdue University

West Lafayette, Indiana

# THE PURDUE UNIVERSITY GRADUATE SCHOOL
# STATEMENT OF THESIS APPROVAL

Dr. Kathleen C. Howell, Chair

School of Aeronautics and Astronautics

Dr. Carolin Frueh

School of Aeronautics and Astronautics

Dr. David A. Spencer

School of Aeronautics and Astronautics

**Approved by:**

Dr. Gregory Blaisdell

Associate Head of Graduate Program of Aeronautics and Astronautics

*To Nanu-Nani & Amma-Baba.*

# ACKNOWLEDGMENTS

First, I would like to thank my family: Papa, Mumma, and Bubba. Your love, support, and encouragement have made everything possible. Thank you for believing in me. Papa, thank you for making Bubba and I believe that we could achieve anything, and for ingraining the value of learning in us from an early age. Mumma, thank you for being there for me every day, and for everything you do for our family. Bubba, you are the hardest-working person I know. You have, and always will be, my best friend. I hope to always make the three of you proud.

Next, I would like to thank my boyfriend, Andrew. I cannot put into words how understanding and supportive you are of me and my goals. Thank you for being there for me, for helping me, and for being the voice of reason when times got rough. I am forever grateful for your love and for everything you do, and I will always be there for you.

I would also like to thank my advisor, Prof. Howell. Thank you for all your guidance and support, and for letting me be a part of your research group. You are, truly, an inspiration for me and for all women in STEM. I look forward to continuing this journey under your leadership.

I am immensely grateful to the past and current members of the Multi-Body Dynamics Research Group: Andrew C., Andrew M., Beom, Bonnie, Brian, Collin, David, Emily, Fouad, Juan, Kenza, Nadia, Nick, Paige, Ricardo, RJ, Robert, Rohith, Stephen, and Vivek. Your feedback and insight have been invaluable, and I appreciate all the help everyone has given me these past two years.

I would like to thank my committee members, Prof. Carolin Frueh and Prof. David Spencer. I am grateful for the time you took to review my thesis and for all the feedback you provided. I would also like to thank Purdue University for awarding me the Charles C. Chappelle Fellowship. Finally, I would like to thank the Purdue

School of Aeronautics and Astronautics and the Purdue Engineering Honors Program for financial support through teaching assistantships.

TABLE OF CONTENTS

Page

LIST OF TABLES . . . . . viii

LIST OF FIGURES . . . . . x

ABSTRACT . . . . . xiii

1 INTRODUCTION . . . . . 1
1.1 Previous Contributions . . . . . 2
1.1.1 Multi-Body Dynamics . . . . . 2
1.1.2 Resonant Orbits . . . . . 3
1.2 Thesis Overview . . . . . 4

2 BACKGROUND – THE CIRCULAR RESTRICTED THREE-BODY PROBLEM . . . . . 6
2.1 The General $\mathcal{N}$-Body Problem . . . . . 6
2.2 The Circular Restricted Three-Body Problem . . . . . 8
2.2.1 Assumptions to Simplify the Relative Three-Body Problem . . . 9
2.2.2 Equations of Motion . . . . . 10
2.2.3 Integrals of Motion . . . . . 15
2.2.4 Equilibrium Points . . . . . 16
2.2.5 Zero Velocity Curves . . . . . 19
2.3 The State Transition Matrix . . . . . 24
2.4 Differential Corrections . . . . . 27
2.4.1 Single Shooting . . . . . 29
2.4.2 Natural Parameter Continuation . . . . . 31
2.5 Coordinate Transformation . . . . . 33

3 BACKGROUND – RESONANT ORBITS . . . . . 37
3.1 Introduction to Resonance . . . . . 37
3.1.1 Orbital Resonance . . . . . 37
3.1.2 Resonance in the Two-Body Model . . . . . 38
3.2 Resonance in the CR3BP . . . . . 43
3.3 Families of Planar Resonant Orbits . . . . . 45
3.3.1 End of a Family . . . . . 50
3.4 Stability of Periodic Orbits . . . . . 51
3.5 Bifurcations . . . . . 54
3.6 Three-Dimensional Resonant Orbits . . . . . 55
3.7 Invariant Manifold Theory . . . . . 56

Page
3.7.1 Manifolds of Fixed Points . . . 59
3.7.2 Manifolds of Periodic Orbits . . . 63
3.7.3 Computation of Manifolds for Resonant Orbits . . . 64
3.8 Poincaré Maps . . . 67

4 RESONANT ORBITS FOR TRAJECTORY DESIGN . . . 73
4.1 Relevant Physical Parameters and CR3BP Quantities . . . 73
4.2 Theoretical Minimum $\Delta$V . . . 74
4.3 Transfers Incorporating Resonant Arcs . . . 76
4.3.1 Tour of the Mars-Deimos System . . . 80
4.4 Transfers Utilizing Resonant Orbit Manifolds . . . 81
4.5 Similarities in Invariant Manifold Structure . . . 87
4.6 Homoclinic and Heteroclinic Connections . . . 92
4.6.1 Homoclinic Connections in the Saturn-Titan System . . . 92
4.6.2 Heteroclinic Connections in the Saturn-Titan System . . . 94
4.7 Resonant Orbit Chains . . . 94

5 CONCLUDING REMARKS . . . 100
5.1 Summary . . . 100
5.2 Recommendations for Future Work . . . 102

REFERENCES . . . 103

# LIST OF TABLES


| Table | | Page |
|---|---|---|
| 2.1 | Values of Jacobi Constant for Libration Points in the Earth-Moon, Saturn-Titan, and Mars-Deimos Systems. | 21 |
| 3.1 | Orbital Parameters of the Moon in the Two-Body Model. | 40 |
| 3.2 | Initial Conditions for Selected Planar Resonant Orbits in the Earth-Moon System. | 47 |
| 3.3 | Eigenvalues of the Monodromy Matrix of the 3:4 Resonant Orbit in the Earth-Moon System. | 53 |
| 3.4 | Initial Conditions for Selected Spatial Resonant Orbits in the Earth-Moon System. | 57 |
| 4.1 | Physical Parameters for Relevant Bodies. | 74 |
| 4.2 | CR3BP Quantities Corresponding to Relevant Systems. | 74 |
| 4.3 | Initial Conditions and Jacobi Constant Values for the Departure and Arrival Orbits. | 76 |
| 4.4 | Initial Conditions and Jacobi Constant Value for the Selected 2:3 Resonant Orbit in the Earth-Moon System. | 78 |
| 4.5 | Departure and Arrival Maneuver Magnitudes for Transfer using a 2:3 Resonant Orbit Arc in the Earth-Moon System. | 79 |
| 4.6 | Initial Conditions and Jacobi Constant Values for the 3:1 and 2:1 Resonant Orbits. | 81 |
| 4.7 | Initial Conditions and Jacobi Constant Value for the 5:6 Resonant Orbit in the Saturn-Titan System. | 82 |
| 4.8 | Initial Conditions and Jacobi Constant Values for the $L_1$ and $L_2$ Lyapunov Orbits in the Saturn-Titan System. | 85 |
| 4.9 | Initial Conditions and Jacobi Constant Values for the 3:5 and 3:4 Resonant Orbits in the Saturn-Titan System. | 88 |
| 4.10 | Initial Conditions and Jacobi Constant Value for the 3:5 Resonant Homoclinic Connection in the Saturn-Titan System. | 93 |

Table Page

4.11 Initial Conditions and Jacobi Constant Value for the 3:4 Resonant Homoclinic Connection in the Saturn-Titan System. . . . . 96

4.12 Initial Conditions and Jacobi Constant Value for the 3:5 Resonant Homoclinic Connection in the Saturn-Titan System. . . . . 99

# LIST OF FIGURES


Figure Page

2.1 The Inertial Frame in the $\mathcal{N}$-body System. . . . . 7

2.2 The Inertial and Rotating Frames in the CR3BP. . . . . 11

2.3 The Equilibrium Points in the CR3BP Rotating Frame. . . . . 17

2.4 ZVS and ZVC for $C > C_{L_1}$ in the Earth-Moon System. . . . . 21

2.5 ZVS and ZVC for $C = C_{L_1}$ in the Earth-Moon System. . . . . 21

2.6 ZVS and ZVC for $C_{L_2} < C < C_{L_1}$ in the Earth-Moon System. . . . . 22

2.7 ZVS and ZVC for $C = C_{L_2}$ in the Earth-Moon System. . . . . 22

2.8 ZVS and ZVC for $C_{L_3} < C < C_{L_2}$ in the Earth-Moon System. . . . . 22

2.9 ZVS and ZVC for $C = C_{L_3}$ in the Earth-Moon System. . . . . 23

2.10 ZVS and ZVC for $C_{L_{4,5}} < C < C_{L_3}$ in the Earth-Moon System. . . . . 23

2.11 ZVS and ZVC for $C = C_{L_{4,5}}$ in the Earth-Moon System. . . . . 23

2.12 ZVS and ZVC for $C < C_{L_{4,5}}$ in the Earth-Moon System. . . . . 24

2.13 Schematic for a Variable Time Position Targeter. . . . . 30

2.14 An $L_1$ Lyapunov Periodic Orbit in the Earth-Moon System. . . . . 32

2.15 Representative Members from the Family of $L_1$ Lyapunov Periodic Orbits in the Earth-Moon System. . . . . 33

3.1 The 3:4 Resonant Orbit in the Earth-Moon Two-Body Inertial Frame. . . . 41

3.2 The 3:4 Resonant Orbit in the Earth-Moon Two-Body Rotating Frame. . . 42

3.3 The 3:4 Resonant Orbit in the Earth-Moon CR3BP Rotating Frame. . . . 46

3.4 Members of Planar Resonant Orbit Families in Configuration Space in the Earth-Moon CR3BP Rotating Frame. . . . . 48

3.5 Members of Planar Resonant Orbit Families in Configuration Space in the Earth-Moon CR3BP Rotating Frame. . . . . 49

3.6 Possible Locations of $\lambda_j$ in the Complex Plane. . . . . 53

3.7 Change in Eigenvalue Structure associated with each type of Bifurcation. . 55

Figure Page

3.8 Members of Spatial Resonant Orbit Families in the Earth-Moon CR3BP Rotating Frame. . . . . 58

3.9 Stable and Unstable Local Manifolds for $L_2$ in the Earth-Moon System. . . 62

3.10 Stable and Unstable Global Manifolds for the 3:4 Resonant Orbit in the Earth-Moon System. . . . . 66

3.11 Poincaré Map of an Autonomous Section. . . . . 69

3.12 Poincaré Map Returns for Stable, Unstable, and Chaotic Cases. . . . . 69

3.13 Poincaré Map for Stable and Unstable Manifold Returns of the 3:4 Resonant Orbit in the Earth-Moon System. . . . . 71

3.14 Zoomed in Views of the Poincaré Map for the 3:4 Resonant Orbit in the Earth-Moon System. . . . . 72

4.1 The $L_3$ Lyapunov and DRO for Departure and Arrival in the Earth-Moon System. . . . . 77

4.2 Resonant Orbit Perpendicular Crossings for Intermediate Arc Selection. . . 78

4.3 2:3 Resonant Orbit as an Intermediate Transfer Arc in the Earth-Moon System. . . . . 79

4.4 Transfer between $L_3$ Lyapunov Orbit and DRO employing a 2:3 Resonant Orbit Arc in the Earth-Moon System. . . . . 80

4.5 3:2 and 2:1 Resonant Tour Trajectory in the Mars-Deimos System. . . . . 82

4.6 Double-Loop 5:6 Resonant Orbit in the Saturn-Titan System. . . . . 83

4.7 Poincaré Map for the Stable Manifolds (Blue) and Unstable Manifolds (Magenta) of the 5:6 Resonant Orbit in the Saturn-Titan System. . . . . 84

4.8 $L_1$ and $L_2$ Lyapunov Orbits at $C = 3.0013$ in the Saturn-Titan System. . . 85

4.9 Transfer from a 5:6 Resonant Orbit to an $L_1$ Lyapunov Orbit in the Saturn-Titan System. . . . . 86

4.10 Transfer from a 5:6 Resonant Orbit to an $L_2$ Lyapunov Orbit in the Saturn-Titan System. . . . . 87

4.11 The 3:5 and 3:4 Resonant Orbits at $C = 3.0013$ in the Saturn-Titan System. 88

4.12 Poincaré Map for the Stable Manifolds (Blue) and Unstable Manifolds (Pink) of the 3:5 Resonant Orbit in the Saturn-Titan System. . . . . 90

4.13 Poincaré Map for the Stable Manifolds (Cyan) and Unstable Manifolds (Orange) of the 3:4 Resonant Orbit in the Saturn-Titan System. . . . . 90

Figure Page

4.14 Poincaré Map for the Stable Manifolds (Blue) and Unstable Manifolds (Gold) of the $L_1$ Lyapunov Orbit in the Saturn-Titan System. . . . . 91

4.15 Poincaré Map for the Stable Manifolds (Green) and Unstable Manifolds (Red) of the $L_2$ Lyapunov Orbit in the Saturn-Titan System. . . . . 91

4.16 Homoclinic Connection for the 3:5 Resonant Orbit in the Saturn-Titan System. . . . . 93

4.17 Poincaré Map for the Stable Manifolds (Blue) of the 5:6 Resonant Orbit and the Unstable Manifolds (Orange) of the 3:4 Resonant Orbit. . . . . 95

4.18 Heteroclinic Connection between the 3:4 and the 5:6 Resonant Orbits in the Saturn-Titan System. . . . . 95

4.19 Poincaré Section for the Stable and Unstable Manifolds of the 3:4 Resonant Orbit with the Fixed Point for the 9:8 Resonant Orbit. . . . . 97

4.20 Homoclinic Connection for the 3:4 Resonant Orbit in the Saturn-Titan System. . . . . 97

4.21 Family of the 3:4-9:8 Resonant Orbit Chain in the Saturn-Titan System. . 98

4.22 Poincaré Section for the Stable and Unstable Manifolds of the 3:5 Resonant Orbit with the Fixed Point for the 9:10 Resonant Orbit. . . . . 98

4.23 Homoclinic Connection for the 3:5 Resonant Orbit in the Saturn-Titan System. . . . . 99

4.24 Family of the 3:5-9:10 Resonant Orbit Chain in the Saturn-Titan System. . 99

# ABSTRACT

Gupta, Maaninee M.S.A.A., Purdue University, May 2020. Finding Order in Chaos: Resonant Orbits and Poincaré Sections. Major Professor: Kathleen C. Howell.

Resonant orbits in a multi-body environment have been investigated in the past to aid the understanding of perceived chaotic behavior in the solar system. The invariant manifolds associated with resonant orbits have also been recently incorporated into the design of trajectories requiring reduced maneuver costs. Poincaré sections are now also extensively utilized in the search for novel, maneuver-free trajectories in various systems. This investigation employs dynamical systems techniques in the computation and characterization of resonant orbits in the higher-fidelity Circular Restricted Three-Body model. Differential corrections and numerical methods are widely leveraged in this analysis in the determination of orbits corresponding to different resonance ratios. The versatility of resonant orbits in the design of low cost trajectories to support exploration for several planet-moon systems is demonstrated. The efficacy of the resonant orbits is illustrated via transfer trajectory design in the Earth-Moon, Saturn-Titan, and the Mars-Deimos systems. Lastly, Poincaré sections associated with different resonance ratios are incorporated into the search for natural, maneuver-free trajectories in the Saturn-Titan system. To that end, homoclinic and heteroclinic trajectories are constructed. Additionally, chains of periodic orbits that mimic the geometries for two different resonant ratios are examined, i.e., periodic orbits that cycle between different resonances are determined. The tools and techniques demonstrated in this investigation are useful for the design of trajectories in several different systems within the CR3BP.

# 1. INTRODUCTION

As human interest in spaceflight evolves over time, so must the capabilities and technologies that support these goals. One such novel idea in trajectory design is recently being adopted for implementation on spaceflight missions is resonance. Conceptually, resonant orbits and their invariant manifolds are familiar in the design of significantly low-cost and unusual trajectories in several planet-moon systems. The inherent stability of some resonant orbits is understood for long-term mission design, while the intrinsically unstable trajectories are recognized for application to transfer trajectory design for low propellant usage. This investigation aims to compute and apply resonant orbits and the associated natural flow towards trajectory design in the Circular Restricted Three-Body model. In addition to the dynamical systems theory, Poincaré sections are exploited to aid in the understanding of the complex, 'tangled' structures that result from resonant orbits.

From a historical standpoint, the mission to explore the moons of Jupiter – Europa, Ganymede, and Callisto – named the Jupiter Icy Moons Orbiter (JIMO), is designed leveraging the multi-body spacecraft environment [1]. Specifically, resonances with the moons of Jupiter are utilized to transfer the spacecraft to desired orbits, resulting in a significant reduction of propellant usage throughout the duration of the mission. Similarly, the Jupiter Ganymede Orbiter mission, a component of the Europa Jupiter System Mission (EJSM), is expected to accomplish multiple resonant flybys of Callisto in its approach to Ganymede [2]. The incorporation of resonant orbits in these mission trajectories motivated research into understanding the underlying dynamics of flow resulting from resonant orbits [3], [4].

For applications in the multi-body regime, the Interstellar Boundary Explorer (IBEX), launched in 2008 into a highly elliptical Earth orbit, originally experienced significant quasiperiodic oscillations in its radius of periapsis as a result of Moon

encounters. Consequently, the mission team elected to transfer into a more stable, spatial orbit in 3:1 resonance with the Moon around the Earth, thereby guaranteeing orbital stability for at least two decades [5]. In 2018, the Transiting Exoplanet Survey Satellite (TESS), directly launched into a spatial 2:1 resonant orbit in the Earth-Moon system, owing to the stability of the orbit and the successful transition of IBEX to a resonant orbit, [6], [7]. The selected TESS orbit is expected to retain its stability for decades before orbit maintenance maneuvers are necessary [8].

With growing interest in resonant orbits as efficient options for trajectory design, this investigation aims to: (1) compute and catalog orbits of various resonances in several planet-moon systems in the solar system, (2) highlight the versatility of resonant orbits and their invariant manifolds for transfer trajectory design, and (3) incorporate Poincaré sections associated with resonant orbit manifolds into the search for novel trajectories. With these goals, the inherent characteristics of resonant orbits are exploited for applications in trajectory design.

## 1.1 Previous Contributions

### 1.1.1 Multi-Body Dynamics

The publication of *Astronomia Nova* by Johannes Kepler in 1609, in which he derived the three laws of planetary motion using empirical methods, cemented his legacy in celestial mechanics [9]. Since the laws were purely empirical, they did not offer a physical rationale to support the resulting behavior. Only in 1687, when Isaac Newton derived the inverse square force law, Kepler's laws were confirmed to be a consequence of the natural force of gravitation [10]. In his publication, Newton also formulated his three laws of motion, which have, coupled with the universal law of gravitation, shaped current understanding of the mechanics of the universe. Unsuccessfully, Newton also attempted to solve the $\mathcal{N}$-body problem, later pursued by Leonhard Euler in 1772. Euler formulated the three-body problem, formulating the motion of three planetary bodies in a rotating coordinate frame [11]. Joseph

Lagrange, in the same year, computed equilibrium solutions in the three-body model, contributing additional insight into the problem. In 1836, Jacobi demonstrated that the combining the conservation of energy and angular momentum renders an integral of motion, termed the Jacobi integral [11]. Only in 1893, Henri Poincaré termed the three-body problem *restricted*, and offered a qualitative assessment of the problem. The work by Poincaré forms the basis of chaos theory and the theory of dynamical systems. In 1881, Poincaré introduced Poincaré mapping as a tool for the visualization of complex dynamical behaviour [11]. Due to the lack of technological capabilities until the $20^{th}$ century, the methods presented by Poincaré are only recently being adopted for solar system applications.

### 1.1.2 Resonant Orbits

The phenomenon of orbital resonance is well observed in the solar system and has long been used to explain trends in seemingly chaotic behavior. Specifically, the orbits of comets in resonance with Jupiter are validated via resonance and associated transitions [4]. In 1997, Belbruno and Marsden discussed the motion of short-period comets under the effect of resonance, illustrating the temporary capture of the 3:2 and 2:3 resonant comets around Jupiter [12]. In 2000, Koon, et al. theoretically demonstrated the role of invariant manifolds in the low energy, planar resonant transfers and capture mechanisms for the Jupiter family of comets [13]. In 2001, Howell, Marchand, and Lo numerically confirmed those results and extended the analysis to spatial transfers [14]. In 2010, Vaquero employed Poincaré sections and dynamical systems techniques in understanding the relationships between the invariant manifolds of the 3:4 and 5:6 unstable resonant orbits in the Jupiter-Europa system [3]. Vaquero, in 2013, also demonstrated the role of resonant orbits in the design of planar and spatial transfer scenarios, along with cataloging resonant orbits in the Saturn-Titan system [15]. In 2018, Vutukuri employed resonances as transfer tools in the design of trajectories between non-resonant, stable periodic orbits [16].

## 1.2 Thesis Overview

This investigation expands on the work by Vaquero and Vutukuri for application in the Earth-Moon, Saturn-Titan, and Mars-Deimos systems. The chapters in this document are summarized as follows:

- **Chapter 2**: In this chapter, the general $\mathcal{N}$-body model is introduced. The complexities associated with that model are presented, followed by simplifications that reduce the model to three bodies. The underlying assumptions that result in the Circular Restricted Three-Body Problem (CR3BP) are then described. The equations of motion of the CR3BP are derived, and the mathematical framework for the model is detailed. Equilibrium solutions and zero velocity curves in the CR3BP are then presented within the context of the Earth-Moon system. The state transition matrix is introduced, and the information offered by the matrix is utilized in the development of differential corrections schemes. A single shooting algorithm is detailed and employed in the computation of periodic orbits in the CR3BP. A natural parameter continuation scheme is introduced for the computation of families of periodic orbits in the Earth-Moon system. Finally, coordinate transformations between the inertial and rotating CR3BP frames is derived.

- **Chapter 3**: This chapter introduces the concept of resonance, with emphasis on orbital resonance. Resonant orbits in the two-body model are derived and visualized in both the inertial and the rotating frames. The concepts of interior and exterior resonances, as well as sidereal and synodic periods, are introduced. The methodology of translating the initial conditions corresponding to two-body resonant orbits into resonant orbits in the CR3BP is discussed. The technique of natural parameter continuation is implemented for the computation of families of planar resonant orbits in the Earth-Moon system. Various different resonance ratios and their associated geometries are introduced. The definition of the termination of a family of periodic orbits is then presented. Next, the

concept of stability of periodic orbits is detailed within the context of resonant orbits, followed by the different types of bifurcations in the CR3BP. Spatial resonant orbit families emanating from planar resonant orbits in the Earth-Moon system are described. The invariant manifold theory is then presented, with details regarding the computation of manifolds for fixed points, periodic orbits, and resonant orbits. Finally, Poincaré maps are introduced and applied in the visualization of the chaotic dynamics associated with resonant orbits.

- **Chapter 4**: The tools and concepts introduced in the previous chapters are applied towards trajectory design in the CR3BP. The physical parameters and CR3BP quantities associated with the relevant planet-moon systems are first introduced. The concept of the theoretical minimum $\Delta$V is then detailed. Transfer scenarios incorporating resonant orbits as intermediate transfer arcs are presented in the Earth-Moon and Mars-Deimos systems. Then, transfer scenarios incorporating resonant orbit manifolds as transfer arcs from resonant orbits to libration point orbits are detailed in the Saturn-Titan system. Poincaré sections are employed in the construction of these transfer scenarios. The similarities in the manifold structure for several different orbits at a given value of Jacobi constant in the Saturn-Titan system is noted. Homoclinic and heteroclinic connections between different resonant orbits are illustrated, and natural, maneuver-free transfers between orbits are computed. Finally, chains of periodic orbits that cycle between multiple resonance ratios are determined, and families of such chains of orbits are computed.

- **Chapter 5**: This chapter details the conclusions of this study. The efficacy of resonant orbits for trajectory design is summarized. The recommendations for future work in the investigation of resonant orbits are suggested.

# 2. BACKGROUND – THE CIRCULAR RESTRICTED THREE-BODY PROBLEM

The concept of resonance in any gravitational model requires an understanding of the underlying dynamics. Although a discrete number of resonant orbits are available in the two-body problem, an infinite number of resonant orbits actually exist in the three-body problem. Thus, the three-body problem serves as the foundation of this analysis. Thus, the general $\mathcal{N}$-body problem is introduced, along with the accompanying assumptions that reduce the model to the circular restricted three-body problem (CR3BP). The assumptions, equations of motion, and the resulting mathematical framework for the CR3BP are detailed. The equilibrium solutions are computed and the bounds on the behavior in this gravitational model are investigated. Finally, the methods involved in the numerical computation of solutions in the CR3BP are discussed.

## 2.1 The General $\mathcal{N}$-Body Problem

The $\mathcal{N}$-body problem is the most general model employed in celestial mechanics to illustrate the interaction of bodies under their mutual gravitational attraction. Each point mass is assumed to be under the gravitational influence of the remaining $\mathcal{N}-1$ bodies. Let $P_i$ be defined as one of the $\mathcal{N}$ bodies; each $P_i$ possesses mass $m_i$. Define an inertial frame by dextral orthonormal unit vectors $\hat{X}-\hat{Y}-\hat{Z}$, as illustrated in Figure 2.1. Let the point $O$ be inertially fixed such that it serves as a reference point to locate each body in space. Then, $\bar{r}_i$ represents the vector from point $O$ to the body $P_i$. From Newton's law of universal gravitation [10], the force exerted on each body is modeled as,

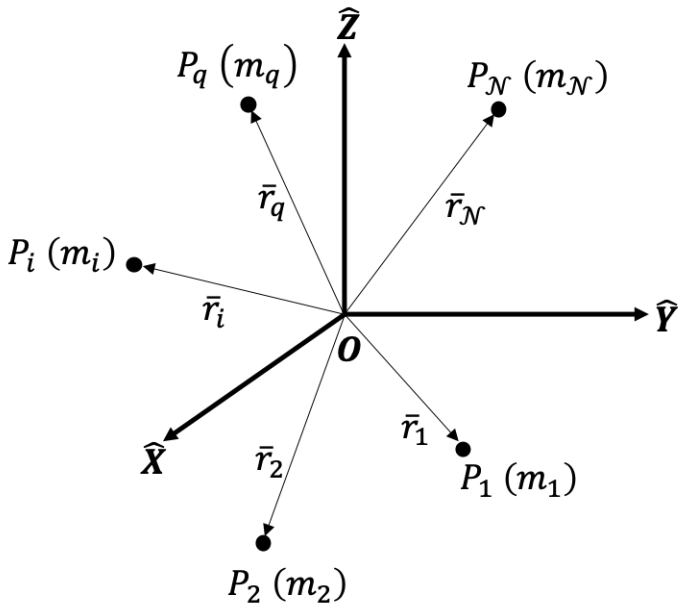


Figure 2.1. The Inertial Frame in the $\mathcal{N}$-body System.

$$\bar{F}_i = -Gm_i \sum_{\substack{j=1 \\ j\neq i}}^{\mathcal{N}} \frac{m_j}{r_{ji}^3} \bar{r}_{ji} \tag{2.1}$$

where $G$ is the universal gravitational constant, and $\bar{r}_{ji}$ is the relative position vector of body $i$ with respect to body $j$. Note that overbars denote vectors. Assuming that the masses in the system are not variable, the vector equation of motion governing the behavior of each particle $P_i$ as a result of the gravitational influence of other bodies is produced as,

$$m_i \bar{r}_i'' = -G \sum_{\substack{j=1 \\ j\neq i}}^{\mathcal{N}} \frac{m_i m_j}{r_{ji}^3} \bar{r}_{ji} \tag{2.2}$$

The primes indicate that the derivative is taken with respect to dimensional time and the observer is inertial. The vector second-order differential equation in Equation (2.2) is rewritten as six scalar first-order differential equations. Thus, for each particle in the $\mathcal{N}$-body system, there exist 6 scalar nonlinear differential equations that reflect the translational degrees of freedom. In total, there are then $6\mathcal{N}$ coupled scalar nonlinear

differential equations that govern the dynamics of the $\mathcal{N}$-body system. Thus, an analytical solution requires $6\mathcal{N}$ integrals of motion. However, only ten integrals of motion are currently known: six arise from conservation of linear momentum, three from conservation of angular momentum, and one from conservation of energy. So, the general $\mathcal{N}$-body problem cannot be solved in a closed analytical form.

To seek a more representative formulation, the $\mathcal{N}$-body problem is straightforwardly reformulated in terms of relative motion. Express the position of a body $P_i$ relative to a central body $P_q$ as $\bar{r}_{qi}$. The vector equation of motion is then derived as,

$$\bar{r}''_{qi} + \frac{G(m_i + m_q)}{r^3_{qi}}\bar{r}_{qi} = G\sum_{\substack{j=1 \\ j\neq i,q}}^{n} m_j \left(\frac{\bar{r}_{ij}}{r^3_{ji}} - \frac{\bar{r}_{qj}}{r^3_{qj}}\right) \tag{2.3}$$

The right side of Equation (2.3) is the perturbing accelerations on the motion of $P_i$ and $P_q$ due to other bodies in the system. When $\mathcal{N} = 2$, i.e., the more familiar 2-body model, the perturbing terms in Equation (2.3) are zero. In such a case, there exists a closed form analytical solution that governs the relative motion of two bodies. However, when $\mathcal{N} > 2$, this result no longer holds, and numerical techniques are necessary to explore the gravitational interactions between bodies.

## 2.2 The Circular Restricted Three-Body Problem

The general three-body problem is formulated by considering the motion of three bodies: $P_1$, $P_2$, and $P_3$ of masses $m_1$, $m_2$, and $m_3$ respectively. Letting $\mathcal{N} = 3$, Equation (2.2) is rewritten as,

$$m_3\bar{r_3}'' = -G\frac{m_3 m_1}{r^3_{13}}\bar{r}_{13} - G\frac{m_3 m_2}{r^3_{23}}\bar{r}_{23} \tag{2.4}$$

The solution for Equation (2.4) requires knowledge of the position vectors $\bar{r}_1(t)$ and $\bar{r}_2(t)$. These position vectors are not available since $P_1$ and $P_2$ are influenced by the motion of $P_3$ and its instantaneous position. Solving for all three position vectors

simultaneously requires 18 integrals of motion; only 10 constants of the motion are available. Reformulating the problem in terms of relative motion affords additional insight in the two-body problem. Consider, then, the motion of $P_3$ relative to the motion of $P_1$ and with respect to $P_2$ as,

$$\bar{r}_{13}'' + \frac{G(m_1 + m_3)}{r_{13}^3}\bar{r}_{13} = Gm_2\left(\frac{\bar{r}_{32}}{r_{32}^3} - \frac{\bar{r}_{12}}{r_{12}^3}\right) \tag{2.5}$$

$$\bar{r}_{23}'' + \frac{G(m_2 + m_3)}{r_{23}^3}\bar{r}_{23} = Gm_1\left(\frac{\bar{r}_{31}}{r_{31}^3} - \frac{\bar{r}_{21}}{r_{21}^3}\right) \tag{2.6}$$

This formulation results in two second-order vector differential equations, that, together, serve as the dynamical model for the time history governing $\bar{r}_{13}$ and $\bar{r}_{23}$. However, the analytical solution is unavailable since this formulation requires 12 constants. Although the problem does not possess a closed form analytical solution, great insight is gained by introducing some simplifying assumptions that make the problem more tractable. This simplified problem is termed the circular restricted three-body problem (CR3BP).

### 2.2.1 Assumptions to Simplify the Relative Three-Body Problem

The CR3BP is a stepping stone in orbital mechanics that builds upon insights from the two-body model while incorporating some of the complexities of the $\mathcal{N}$-body model. The three bodies that comprise the system are $P_1$ and $P_2$, labelled the primaries, and the third body, $P_3$, representing a spacecraft or a smaller celestial body. Assuming that the body of interest is $P_3$, the critical assumptions that form the basis of the CR3BP are:

- The mass of $P_3$ is infinitesimal relative to the masses of $P_1$ and $P_2$, such that $m_3 << m_2 < m_1$. This relationship is a reasonable assumption when modeling the motion of a spacecraft ($P_3$) under the influence of a set of larger primaries, for instance, a planet and a moon. This assumption implies that $P_3$ does not influence the motion of the two primaries.

- Being independent of $P_3$, the motion of the primaries are modeled as an isolated two-body system. The solution of the system is known to be conic, and for most relevant applications, a closed conic.

- The primaries $P_1$ and $P_2$ move on circular orbits about their mutual barycenter. The mutual plane of motion of the two primaries is fixed. However, $P_3$ is free to move in any spatial dimension.

The simplified model resulting from these assumptions is illustrated in Figure 2.2. The inertial reference frame is represented by the unit vectors $\hat{X} - \hat{Y} - \hat{Z}$. The frame rotates with the motion of the primaries and is represented by $\hat{x} - \hat{y} - \hat{z}$; the two primaries lie on the $\hat{x}$-axis. The origins of both the frames lie at the system barycenter, $B$. The angle $\theta$ represents the orientation of the rotating frame with respect to the inertial frame and is measured in the plane of motions of the primaries. The rate of change of $\theta$, i.e., $\dot{\theta}$, represents the angular velocity of the primary system, which is constant for the circular orbits of the primaries. This rate is also equal to the mean motion of the orbits of the primaries, $N$, in dimensional units.

### 2.2.2 Equations of Motion

Once the assumptions associated with the CR3BP are satisfied, it is convenient to nondimensionalize the equations of motion associated with the system. Time is replaced as the independent variable in the problem and the new formulation offers greater insight over a larger range of problems. To nondimensionalize, characteristic quantities are first identified; let $l^*, m^*$, and $t^*$, be defined as the characteristic length, characteristic mass, and characteristic time, respectively. These quantities are defined as,

$$l^* = \|\bar{r}_1\| + \|\bar{r}_2\| \tag{2.7}$$

$$m^* = m_1 + m_2 \tag{2.8}$$

$$t^* = \sqrt{\frac{l^{*3}}{Gm^*}} \tag{2.9}$$

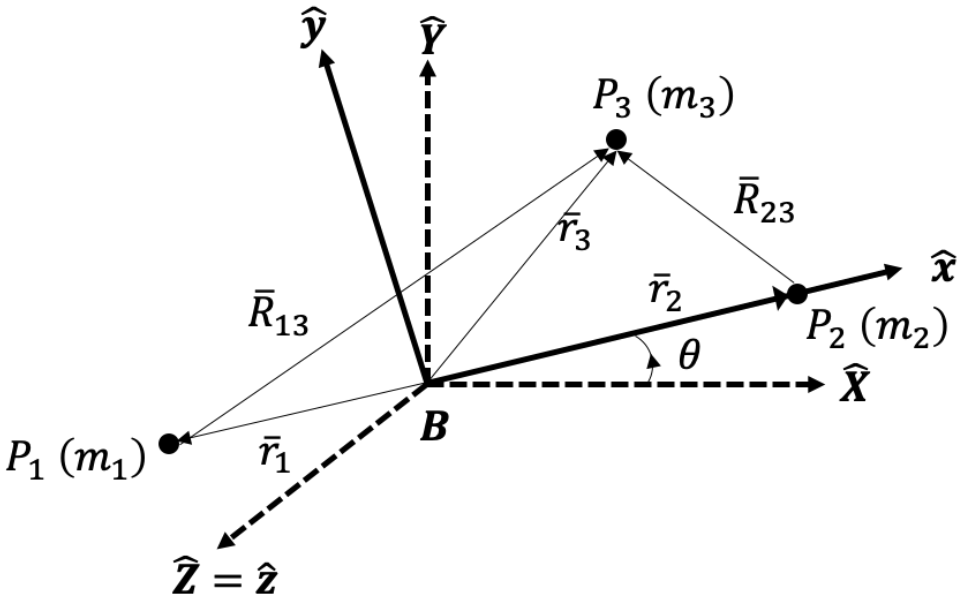


Figure 2.2. The Inertial and Rotating Frames in the CR3BP.

Additionally, other useful nondimensional parameters are also defined using the characteristic quantities. The nondimensional mean motion, $n$, is then,

$$n = Nt^* \tag{2.10}$$

where $N$ is the dimensional mean motion associated with the primaries. For $n$ as evaluated in Equation (2.10), the nondimensional value is equal to 1. Next, the nondimensional time variable $\tau$ is defined as,

$$\tau = \frac{t}{t^*} \tag{2.11}$$

Next, a nondimensional mass parameter $\mu$ is defined for convenience such that,

$$\mu = \frac{m_2}{m^*} \tag{2.12}$$

Finally, the vectors that represent the location of $P_3$ with respect to the barycenter and each of the two primaries are nondimensionalized using the characteristic quantity $l^*$ as,

$$\bar{\rho} = \frac{\bar{r}_3}{l^*} = x\hat{x} + y\hat{y} + z\hat{z} \tag{2.13}$$

$$\bar{d} = \frac{\bar{R}_{13}}{l^*} = (x+\mu)\hat{x} + y\hat{y} + z\hat{z} \tag{2.14}$$

$$\bar{r} = \frac{\bar{R}_{23}}{l^*} = (x-1+\mu)\hat{x} + y\hat{y} + z\hat{z} \tag{2.15}$$

These nondimensional quantities yield a straightforward approach for the derivation of the equations of motion associated with the CR3BP.

Recall from Equation (2.4), the motion of $P_3$ as expressed in terms of the masses of the primaries and the relative position vectors. This equation is rewritten in terms of the vectors defined in the rotating CR3BP frame as,

$$m_3\bar{r}_3'' = -G\frac{m_3m_1}{R_{13}^3}\bar{R}_{13} - G\frac{m_3m_2}{R_{23}^3}\bar{R}_{23} \tag{2.16}$$

Cancelling out the $m_3$ term from both sides of Equation (2.16) and substituting the nondimensional characteristic quantities and variables, the vector equation reduces to,

$$\ddot{\bar{\rho}} = -(1-\mu)\frac{\bar{d}}{d^3} - \mu\frac{\bar{r}}{r^3} \tag{2.17}$$

The dots indicate the derivative with respect to nondimensional time, $\tau$. In Equation (2.17), the values of $d$ and $r$ are defined as,

$$d = \sqrt{(x+\mu)^2 + y^2 + z^2} \tag{2.18}$$

$$r = \sqrt{(x-1+\mu)^2 + y^2 + z^2} \tag{2.19}$$

To construct the left side of Equation (2.17), i.e., the double derivative of $\rho$ as expressed in rotating coordinates but viewed with respect to the inertial frame, the Basic

Kinematic Equation is employed. First, define the angular velocity of the rotating frame with respect to the inertial frame,

$$ {}^{I}\bar{\omega}^{R} = n\hat{z} \tag{2.20} $$

The superscripts $I$ and $R$ denote the inertial and rotating frames, respectively. Using the expression for angular velocity in Equation (2.20), the first derivative of $\rho$ is evaluated as,

$$ {}^{I}\dot{\bar{\rho}} = {}^{R}\dot{\bar{\rho}} + ({}^{I}\bar{\omega}^{R} \times {}^{R}\bar{\rho}) \tag{2.21} $$

Substituting the relevant values into Equation (2.21) results in,

$$ {}^{I}\dot{\bar{\rho}} = (\dot{x} - ny)\hat{x} + (\dot{y} + nx)\hat{y} + (\dot{z})\hat{z} \tag{2.22} $$

Differentiating Equation (2.22) results in the following kinematic expansion for $\ddot{\bar{\rho}}$,

$$ {}^{I}\ddot{\bar{\rho}} = {}^{R}\ddot{\bar{\rho}} + ({}^{I}\bar{\omega}^{R} \times {}^{R}\dot{\bar{\rho}}) \tag{2.23} $$

$$ {}^{I}\ddot{\bar{\rho}} = (\ddot{x} - 2n\dot{y} - n^2x)\hat{x} + (\ddot{y} + 2n\dot{x} - n^2y)\hat{y} + (\ddot{z})\hat{z} \tag{2.24} $$

Equation (2.24) represents the left side of Equation (2.17) in terms of rotating coordinates. The right side of Equation (2.17) is decomposed further as follows,

$$ \begin{aligned} \ddot{\bar{\rho}} = & \left( \frac{-(1-\mu)(x+\mu)}{d^3} - \frac{\mu(x-1+\mu)}{r^3} \right) \hat{x} \\ & + \left( \frac{-(1-\mu)y}{d^3} - \frac{\mu y}{r^3} \right) \hat{y} \\ & + \left( \frac{-(1-\mu)z}{d^3} - \frac{\mu z}{r^3} \right) \hat{z} \end{aligned} \tag{2.25} $$

Combining Equations (2.24) and (2.25), the three scalar, second-order nondimensional differential equations of motion for $P_3$, under the gravitational influence of the two primaries, are obtained as,

$$\ddot{x} - 2n\dot{y} - n^2 x = \frac{-(1-\mu)(x+\mu)}{d^3} - \frac{\mu(x-1+\mu)}{r^3} \tag{2.26}$$

$$\ddot{y} + 2n\dot{x} - n^2 y = \frac{-(1-\mu)y}{d^3} - \frac{\mu y}{r^3} \tag{2.27}$$

$$\ddot{z} = \frac{-(1-\mu)z}{d^3} - \frac{\mu z}{r^3} \tag{2.28}$$

Since the time variable does not appear explicitly in these equations, the system is autonomous. These second-order nondimensional scalar differential equations are rewritten as six first-order differential equations and numerically integrated using specified initial conditions.

Since the formulation is developed in the rotating frame, the integral of the differential equations yields a potential function $U^*$ that is actually an augmented potential function. This new potential, called the *pseudo-potential*, is defined as,

$$U^* = U + \frac{n^2(x^2+y^2)}{2} \tag{2.29}$$

Simplifying Equation (2.29) and substituting the value of nondimensional mean motion $n$, the pseudo-potential function becomes,

$$U^* = \frac{(1-\mu)}{d} + \frac{\mu}{r} + \frac{(x^2+y^2)}{2} \tag{2.30}$$

The differential equations of motion can then be rewritten in terms of $U^*$ as,

$$\ddot{x} - 2\dot{y} = \frac{\partial U^*}{\partial x} \tag{2.31}$$

$$\ddot{y} + 2\dot{x} = \frac{\partial U^*}{\partial y} \tag{2.32}$$

$$\ddot{z} = \frac{\partial U^*}{\partial z} \tag{2.33}$$

These equations, in theory, supply a sufficient number of scalar differential equations to solve for the motion of $P_3$ mathematically. However, since the equations are coupled and nonlinear, no general closed form solution is available. Analysis of the properties of the differential equations yields useful particular solutions.

### 2.2.3 Integrals of Motion

Since the system modeled by the CR3BP is conservative, there may exist an energy-like quantity that is constant for the problem formulation in the rotating frame. To compute this energy integral, first consider the velocity vector in the rotating frame,

$$^{R}\bar{v} = \dot{\bar{\rho}} = \dot{x}\hat{x} + \dot{y}\hat{y} + \dot{z}\hat{z} \tag{2.34}$$

Then, the dot product between the velocity vector in Equation (2.34) and the vector form of the Equations (2.31)-(2.33) yields,

$$\dot{x}\ddot{x} - 2\dot{x}\dot{y} = \frac{\partial U^*}{\partial x}\dot{x} \tag{2.35}$$

$$\dot{y}\ddot{y} + 2\dot{y}\dot{x} = \frac{\partial U^*}{\partial y}\dot{y} \tag{2.36}$$

$$\dot{z}\ddot{z} = \frac{\partial U^*}{\partial z}\dot{z} \tag{2.37}$$

Next, add these three scalar equations, i.e.,

$$\dot{x}\ddot{x} + \dot{y}\ddot{y} + \dot{z}\ddot{z} = \frac{\partial U^*}{\partial x}\dot{x} + \frac{\partial U^*}{\partial y}\dot{y} + \frac{\partial U^*}{\partial z}\dot{z} \tag{2.38}$$

Since $U^*$ is only a function of position, the right side of Equation (2.38) is equal to the total derivative $\frac{dU^*}{d\tau}$. Finally, integrate Equation (2.38) with respect to nondimensional time $\tau$ to yield the integration constant of interest, $C$:

$$\frac{1}{2}(\dot{x}^2 + \dot{y}^2 + \dot{z}^2) = U^* - \frac{C}{2} \tag{2.39}$$

Rearranging the terms in Equation (2.39) results in the following definition of the integration constant $C$, hereby termed the Jacobi constant:

$$C = 2U^* - v^2 \tag{2.40}$$

where $v$ is the magnitude of the relative velocity vector in the rotating frame. While the existence of one integral of motion is not sufficient for a clear, closed-form solution, it does aid numerical analysis.

### 2.2.4 Equilibrium Points

Equilibrium solutions offer practical insight into the behavior of a system. These equilibrium solutions are determined by investigating the locations at which the velocity and acceleration relative to the rotating frame are zero in the differential equations that represent the CR3BP. Specifically, solve the following scalar equations,

$$\frac{\partial U^*}{\partial x} = \frac{\partial U^*}{\partial y} = \frac{\partial U^*}{\partial z} = 0 \tag{2.41}$$

If $P_3$ is placed at any of equilibrium solution locations without any initial velocity or acceleration relative to the rotating frame, the gravitational and centrifugal forces cancel and it maintains its position relative to that frame. Joseph Lagrange, in 1772, determined the five solutions to Equation (2.41) and hence, the equilibrium solutions are termed Lagrange points, libration points, or equilibrium points [11]. These solutions are located in the CR3BP rotating frame, as illustrated in Figure 2.3. All five of the equilibrium points lie in the plane of motion of the primaries, i.e., the $\hat{z}$ component of their positions is zero. Three of these points, namely $L_1, L_2$, and $L_3$, are collinear and lie along the $\hat{x}$-axis. Although the numbering of these points is arbitrary, in this work, the point to the left of $P_2$ is $L_1$, to the right of $P_2$ is $L_2$, and the point to the left of $P_1$ is $L_3$. The remaining two points, $L_4$ and $L_5$, form equilateral triangles with the two primaries, where $L_4$ is defined with a positive $\hat{y}$

component and $L_5$ corresponds to a negative $\hat{y}$ component. To locate the equilibrium points with respect to the primaries, define the distances $\gamma_1$, $\gamma_2$, and $\gamma_3$, also denoted in Figure 2.3.

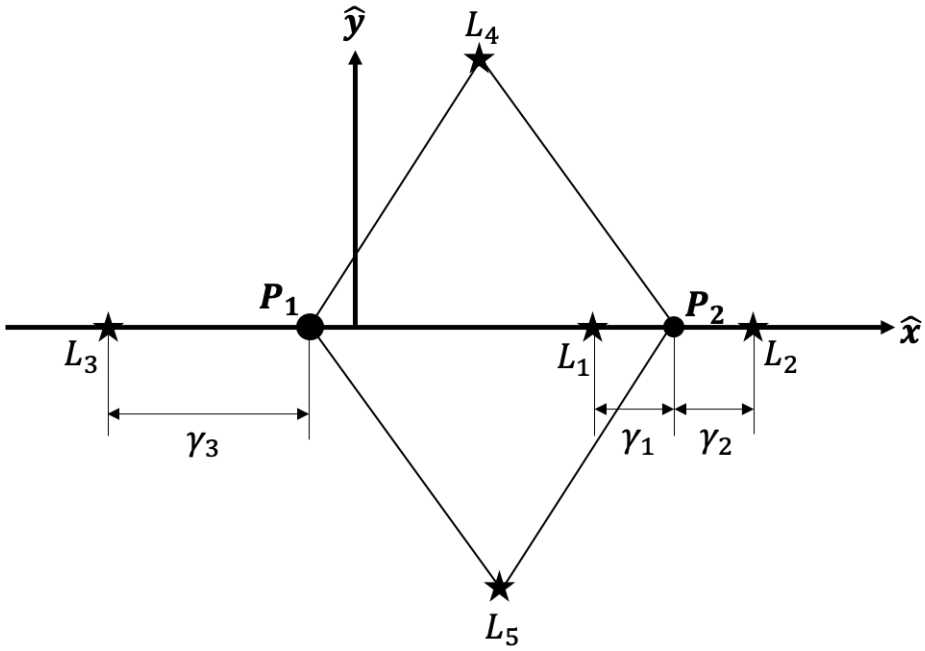


Figure 2.3. The Equilibrium Points in the CR3BP Rotating Frame.

Given that the $\hat{y}$ and $\hat{z}$ components of the collinear libration points are equal to zero, only a solution for their $x$ components is necessary. The expression for the partial derivative of the pseudo-potential function with respect to $x$ equals zero,

$$x_{eq} - \frac{(1-\mu)(x_{eq}+\mu)}{d^3} - \frac{\mu(x_{eq}-1+\mu)}{r^3} = 0 \tag{2.42}$$

Recall that the distances $d$ and $r$ are defined as,

$$d = \sqrt{(x+\mu)^2 + y^2 + z^2} \tag{2.43}$$

$$r = \sqrt{(x-1+\mu)^2 + y^2 + z^2} \tag{2.44}$$

Next, define the $\hat{x}$ components of the location for the collinear libration points as $x_{L_i}$ for $i = 1, 2, 3$. In terms of $\gamma_i$, these components are expressed as,

$$x_{L_1} = 1 - \mu - \gamma_1 \tag{2.45}$$

$$x_{L_2} = 1 - \mu + \gamma_2 \tag{2.46}$$

$$x_{L_3} = -\mu - \gamma_3 \tag{2.47}$$

Equations (2.45)-(2.47) are substituted into Equation (2.42) and result in three fifth-order equations for the three collinear libration points; these are then iteratively solved for the values of $\gamma_i$ for $i = 1, 2, 3$.

A similar approach is adopted to compute the locations of the remaining two libration points, $L_4$ and $L_5$. However, in this case, the $\hat{y}$ components of their locations are not equal to zero. Thus, in addition to Equation (2.42), $\frac{\partial U^*}{\partial y}$ also equals zero. The following expression is then obtained,

$$y\left(1 - \frac{(1-\mu)}{d^3} - \frac{\mu}{r^3}\right) = 0 \tag{2.48}$$

Equating $d = r = 1$ results in the term in the parentheses being equal to zero. Consequently, the two off-axis libration points form equilateral triangles with the two primaries. The components of these points are equal to,

$$x_{L_{4,5}} = \frac{1}{2} - \mu \tag{2.49}$$

$$y_{L_{4,5}} = \pm\frac{\sqrt{3}}{2} \tag{2.50}$$

where $\mu$ is the characteristic quantity associated with the system. With the known locations of the libration points, the dynamics of the system relative to these solutions is insightful.

### 2.2.5 Zero Velocity Curves

An important consequence of the existence of both the equilibrium solutions and the Jacobi constant on the motion of $P_3$ is reflected in the zero velocity curves. Consider the expression for Jacobi constant, in Equation (2.40). Rearranging and expanding the pseudo-potential terms results in,

$$v^2 = (x^2 + y^2) + \frac{2(1-\mu)}{d} + \frac{2\mu}{r} - C \tag{2.51}$$

If the relative velocity in the rotating frame, $v$, is equal to zero, Equation (2.51) reduces to,

$$C = (x^2 + y^2) + \frac{2(1-\mu)}{d} + \frac{2\mu}{r} \tag{2.52}$$

Equation (2.52) implies that, for a given value of Jacobi constant, all locations at which the relative velocity is zero are straightforwardly identified. Since an infinite number of sets of $x$, $y$, and $z$ values satisfy Equation (2.52), all solutions together represent a surface in 3D space. The existence of this zero velocity surface (ZVS) essentially bounds the motion of $P_3$ for a given value of $C$. For solely planar motion, these surfaces are termed zero velocity curves (ZVC); ZVC also reflect a slice of the ZVS through $z = 0$. The region outside the bounds of allowable motion of $P_3$ is denoted a *forbidden region*, and at a given value of Jacobi constant, the particle $P_3$ cannot cross into this region. To move into a forbidden region requires a change in velocity and, consequently, a shift in the Jacobi constant value and the ZVS. Further analysis of these surfaces at any given energy level offers great insight into the dynamical environment.

The libration points corresponding to a specific CR3BP system must always lie on these zero velocity surfaces since, by definition, these equilibrium solutions require the relative velocity and acceleration to be zero. For reference, the values of the Jacobi constant associated with the libration points in the Earth-Moon, Saturn-Titan, and Mars-Deimos systems are summarized in Table 2.1. Figures 2.4-2.12 represent the zero

velocity surfaces and curves in the Earth-Moon system for various values of the Jacobi constant. The two primaries and the libration points are labelled in Figure 2.4(b) for reference. The larger, cylindrical surface in each case represents the exterior region. Moving inwards, the solid white region is inaccessible and reflects the forbidden region. Finally, two additional spherical surfaces surround the two primaries. As the value of Jacobi constant decreases, these two interior surfaces expand and eventually merge to form a single interior region. At the same time, the outer surface contracts, as is evident in Figures 2.4-2.12.

In reference to the zero velocity curves in Figures 2.4-2.12, the white region represents the forbidden region, while the purple surfaces highlight the boundaries of the accessible regions in different views. When the Jacobi constant value is greater than the Jacobi value corresponding to $L_1$, two distinct interior regions emerge, bounding the motion of $P_3$ to the vicinity of either primary, as illustrated in Figure 2.5. As the Jacobi value decreases to the value of $C_{L_1}$, the interior surfaces around $P_1$ and $P_2$ expand and converge to the location of $L_1$, as plotted in Figure 2.6. Decreasing the Jacobi constant further causes the surfaces to merge, opening a *gateway* linking the regions around the primaries. At this value of the Jacobi constant and lower, $P_3$ moves in the interior region between $P_1$ and $P_2$ in the plane of motion without restrictions. Decreasing the Jacobi value to equal that of $C_{L_2}$ results in an expansion of the interior region and further contraction of the exterior region, as apparent in Figure 2.7, converging at the location of $L_2$. At further lower values, the $L_2$ gateway opens, as observed in Figure 2.8. Continuing to decrease the value of the Jacobi constant further, as evident in Figures 2.9 and 2.10, the forbidden region shrinks rapidly, opening the $L_3$ gateway as well. When the Jacobi value is below $C_{L_{4,5}}$, the zero velocity curves disappear in the $x - y$ plane, thus, $P_3$ is free to move around the primaries or exit the system, as illustrated in Figures 2.11 and 2.12. However, inaccessible regions remain beyond the $x - y$ plane, as evident in Figure 2.12(a).

Table 2.1. Values of Jacobi Constant for Libration Points in the Earth-Moon, Saturn-Titan, and Mars-Deimos Systems.

| **System** | $L_1$ | $L_2$ | $L_3$ | $L_4$ | $L_5$ |
|---|---|---|---|---|---|
| Earth-Moon | 3.18834 | 3.17216 | 3.01215 | 2.98799 | 2.98799 |
| Saturn-Titan | 3.01576 | 3.01545 | 3.00024 | 2.99976 | 2.99976 |
| Mars-Deimos | 3.00001 | 3.00001 | 3.00000 | 2.99999 | 2.99999 |

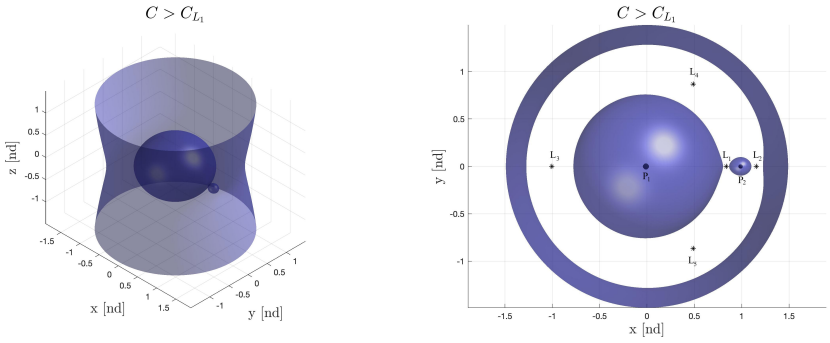


(a) ZVS for $C = 3.2000$ (b) ZVC for $C = 3.2000$

Figure 2.4. ZVS and ZVC for $C > C_{L_1}$ in the Earth-Moon System.

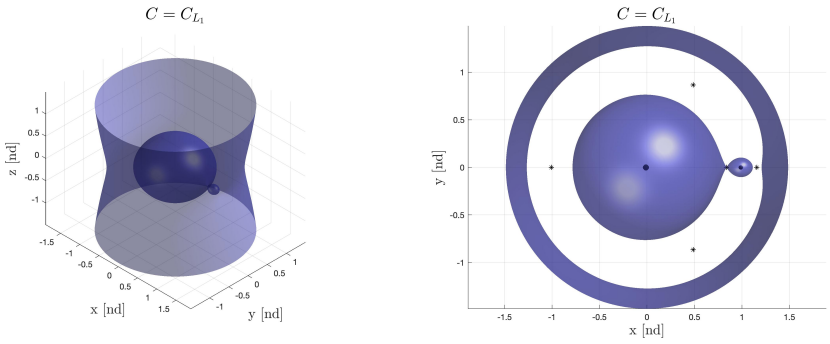


(a) ZVS for $C = 3.1883$ (b) ZVC for $C = 3.1883$

Figure 2.5. ZVS and ZVC for $C = C_{L_1}$ in the Earth-Moon System.

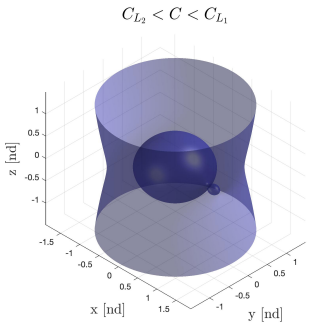


(a) ZVS for $C = 3.1800$

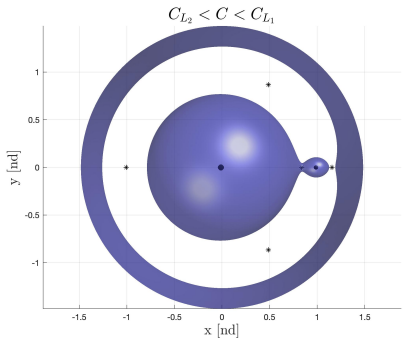


(b) ZVC for $C = 3.1800$

Figure 2.6. ZVS and ZVC for $C_{L_2} < C < C_{L_1}$ in the Earth-Moon System.

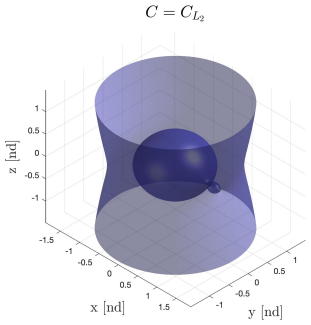


(a) ZVS for $C = 3.1722$

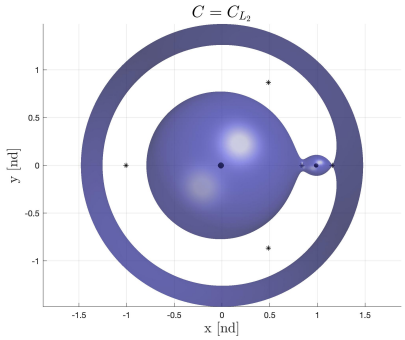


(b) ZVC for $C = 3.1722$

Figure 2.7. ZVS and ZVC for $C = C_{L_2}$ in the Earth-Moon System.

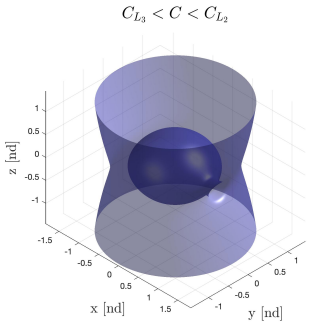


(a) ZVS for $C = 3.0800$

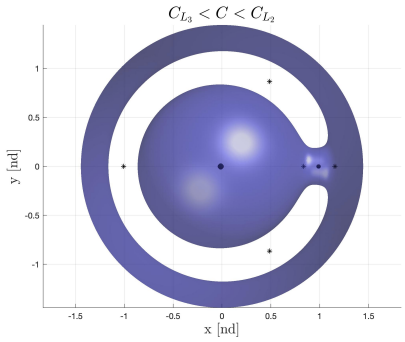


(b) ZVC for $C = 3.0800$

Figure 2.8. ZVS and ZVC for $C_{L_3} < C < C_{L_2}$ in the Earth-Moon System.

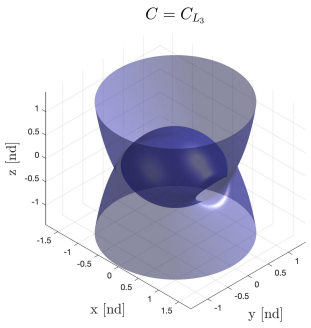


(a) ZVS for $C = 3.0122$

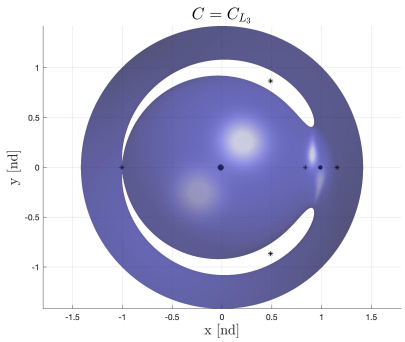


(b) ZVC for $C = 3.0122$

Figure 2.9. ZVS and ZVC for $C = C_{L_3}$ in the Earth-Moon System.

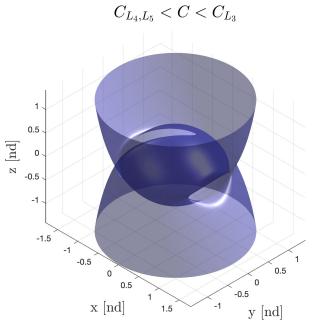


(a) ZVS for $C = 3.0000$

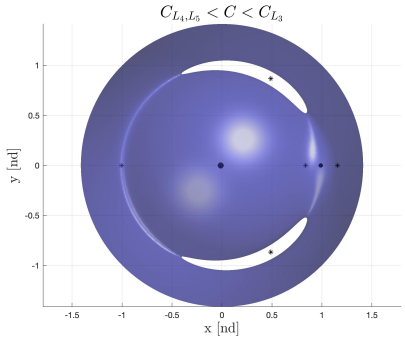


(b) ZVC for $C = 3.0000$

Figure 2.10. ZVS and ZVC for $C_{L_{4,5}} < C < C_{L_3}$ in the Earth-Moon System.

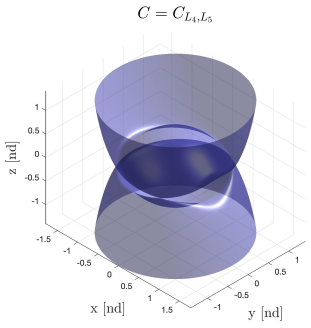


(a) ZVS for $C = 2.9879$

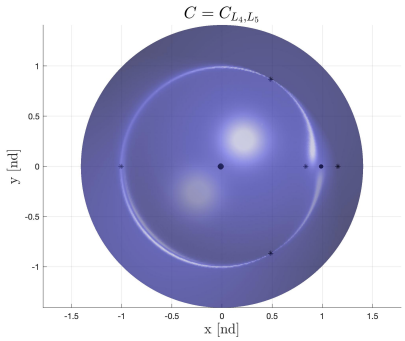


(b) ZVC for $C = 2.9879$

Figure 2.11. ZVS and ZVC for $C = C_{L_{4,5}}$ in the Earth-Moon System.

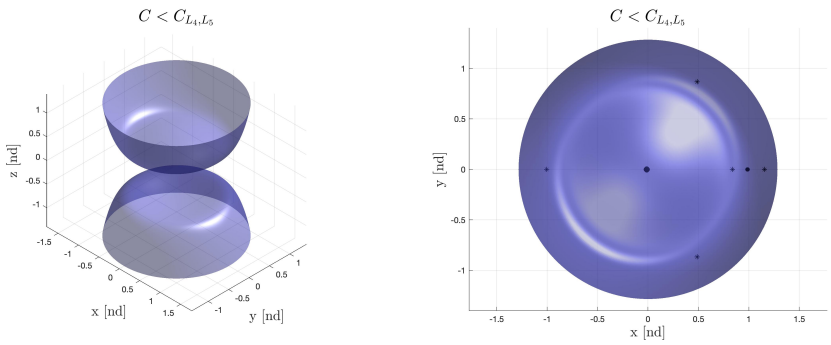


(a) ZVS for $C = 2.7000$ (b) ZVC for $C = 2.7000$

Figure 2.12. ZVS and ZVC for $C < C_{L_{4,5}}$ in the Earth-Moon System.

## 2.3 The State Transition Matrix

The application of numerical methods towards constructing solutions in the CR3BP requires the introduction of the State Transition Matrix (STM). This matrix, also labelled the Sensitivity Matrix or Guidance Matrix, approximates the behavior of a particle in a nonlinear system with respect to a reference solution. Given the variational equations relative to a reference solution, for a state perturbed at any given initial time, the STM provides a linear estimate for the final state at some future time. This information is useful in achieving desired nonlinear behavior in the CR3BP and assessing the associated characteristics, e.g., stability.

To determine the STM, first consider the variational equations. The nonlinear system of differential equations is represented in first-order form as,

$$\dot{\bar{x}} = \bar{f}(\bar{x}, t) \tag{2.53}$$

where the six-element state vector is represented as $\bar{x} = [x\ y\ z\ \dot{x}\ \dot{y}\ \dot{z}]^T$. Let a set of initial conditions in the CR3BP produce a solution or an arc along a trajectory $\bar{x}^*(t)$ over time $t$, as evaluated with the full set of nonlinear differential equations. Then,

with a variation from this solution denoted by $\delta\bar{x}(t)$, a nearby trajectory is expressed as,

$$\bar{x}(t) = \bar{x}^*(t) + \delta\bar{x}(t) \tag{2.54}$$

The definition in Equation (2.54) is employed with Equation (2.53) as,

$$\dot{\bar{x}}^*(t) + \delta\dot{\bar{x}}(t) = \bar{f}(\bar{x}^* + \delta\bar{x}, t) \tag{2.55}$$

Expanding Equation (2.55) in a Taylor series about the reference solution $\bar{x}^*$ and neglecting higher-order terms results in the following linear approximation,

$$\delta\dot{\bar{x}}(t) \approx \left.\frac{\partial\bar{f}}{\partial\bar{x}}\right|_{\bar{x}^*(t)} \bar{x}(t) = A(t)\delta\bar{x}(t) \tag{2.56}$$

Equation (2.56) represents the linear, time-varying variational equations, where the matrix $A(t)$ is the $6 \times 6$ Jacobian matrix of the form,

$$A(t) = \begin{bmatrix} 0_{3\times3} & I_{3\times3} \\ U^*_{XX} & \Omega \end{bmatrix} \tag{2.57}$$

where the constant matrix $\Omega$ is defined as,

$$\Omega = \begin{bmatrix} 0 & 2 & 0 \\ -2 & 0 & 0 \\ 0 & 0 & 0 \end{bmatrix} \tag{2.58}$$

and the matrix $U_{XX}$ is comprised of the second partial derivatives of the pseudo-potential function $\frac{\partial^2 U^*}{\partial i \partial j}$,

$$U^*_{XX} = \begin{bmatrix} U^*_{xx} & U^*_{xy} & U^*_{xz} \\ U^*_{yx} & U^*_{yy} & U^*_{yz} \\ U^*_{zx} & U^*_{zy} & U^*_{zz} \end{bmatrix} \tag{2.59}$$

These partial derivatives are evaluated along the reference trajectory or arc. The solution to Equation (2.56) is then written as,

$$\delta\bar{x}(t) = \Phi(t, t_0)\delta\bar{x}(t_0) \tag{2.60}$$

where $\Phi(t, t_0)$ is the STM evaluated from time $t_0$ to $t$. The STM reflects variations in the state at a time $t$ as a result of any perturbations in the initial state at time $t_0$. Mathematically, the partials are represented as,

$$\Phi(t, t_0) = \frac{\partial\bar{x}(t)}{\partial\bar{x}(t_0)} \tag{2.61}$$

In the CR3BP, the STM is easily expanded as,

$$\Phi(t, t_0) = \begin{bmatrix} \frac{\partial x}{\partial x_o} & \frac{\partial x}{\partial y_o} & \frac{\partial x}{\partial z_o} & \frac{\partial x}{\partial \dot{x}_o} & \frac{\partial x}{\partial \dot{y}_o} & \frac{\partial x}{\partial \dot{z}_o} \\ \frac{\partial y}{\partial x_o} & \frac{\partial y}{\partial y_o} & \frac{\partial y}{\partial z_o} & \frac{\partial y}{\partial \dot{x}_o} & \frac{\partial y}{\partial \dot{y}_o} & \frac{\partial y}{\partial \dot{z}_o} \\ \frac{\partial z}{\partial x_o} & \frac{\partial z}{\partial y_o} & \frac{\partial z}{\partial z_o} & \frac{\partial z}{\partial \dot{x}_o} & \frac{\partial z}{\partial \dot{y}_o} & \frac{\partial z}{\partial \dot{z}_o} \\ \frac{\partial \dot{x}}{\partial x_o} & \frac{\partial \dot{x}}{\partial y_o} & \frac{\partial \dot{x}}{\partial z_o} & \frac{\partial \dot{x}}{\partial \dot{x}_o} & \frac{\partial \dot{x}}{\partial \dot{y}_o} & \frac{\partial \dot{x}}{\partial \dot{z}_o} \\ \frac{\partial \dot{y}}{\partial x_o} & \frac{\partial \dot{y}}{\partial y_o} & \frac{\partial \dot{y}}{\partial z_o} & \frac{\partial \dot{y}}{\partial \dot{x}_o} & \frac{\partial \dot{y}}{\partial \dot{y}_o} & \frac{\partial \dot{y}}{\partial \dot{z}_o} \\ \frac{\partial \dot{z}}{\partial x_o} & \frac{\partial \dot{z}}{\partial y_o} & \frac{\partial \dot{z}}{\partial z_o} & \frac{\partial \dot{z}}{\partial \dot{x}_o} & \frac{\partial \dot{z}}{\partial \dot{y}_o} & \frac{\partial \dot{z}}{\partial \dot{z}_o} \end{bmatrix} \tag{2.62}$$

The STM satisfies the following differential equation for the evolution of the STM over time,

$$\dot{\Phi}(t, t_0) = A(t)\Phi(t, t_0) \tag{2.63}$$

To numerically integrate Equation (2.63) and produce the elements of $\Phi$, the STM at time $t_0$ is initialized as the $6 \times 6$ identity matrix. These 36 first-order scalar differential equations corresponding to each scalar element of the STM along with the six first-

order scalar equations of motion are simultaneously numerically simulated to yield solutions in the CR3BP.

## 2.4 Differential Corrections

A trajectory computed in this model may not always meet the desired criteria; differential corrections are then employed until the desired characteristics are achieved. The computation of the STM is critical in implementing such corrections schemes. Relevant to this investigation is the application of differential corrections towards constructing periodic orbits in the CR3BP. In theory, this method is simply a multi-dimensional version of a Newton-Raphson solver.

The design variable vector and the constraint vectors are first formulated as the initial step in developing a corrections algorithm. These vectors are chosen specific to the problem and the desired final state. In general, the design variable vector is represented by $\bar{X}$ and is of the form,

$$\bar{X} = \begin{bmatrix} X_1 \\ X_2 \\ X_3 \\ \vdots \\ X_n \end{bmatrix} \tag{2.64}$$

where $n$ is the number of free variables in the problem. The constraint vector is represented by $\bar{F}(\bar{X})$, and is defined as,

$$\bar{F}(\bar{X}) = \begin{bmatrix} F_1(\bar{X}) \\ F_2(\bar{X}) \\ F_3(\bar{X}) \\ \vdots \\ F_m(\bar{X}) \end{bmatrix} = \bar{0} \tag{2.65}$$

where $m$ is the number of scalar constraints equations. The goal in the problem is to determine a design vector $\bar{X}_c$ such that $\bar{F}(\bar{X}_c) = \bar{0}$. With $\bar{X}_0$ representing an initial guess for the design variable vector, $\bar{F}(\bar{X})$ is approximated using a first-order Taylor series expansion as,

$$\bar{F}(\bar{X}) \approx \bar{F}(\bar{X}_0) + D\bar{F}(\bar{X}_0) \cdot (\bar{X} - \bar{X}_0) \tag{2.66}$$

where $D(\bar{F})$ is an $m \times n$ matrix of partials evaluated at $\bar{X}_0$,

$$D\bar{F}(\bar{X}_0) = \frac{\partial \bar{F}}{\partial \bar{X}} = \begin{bmatrix} \frac{\partial F_1}{\partial X_1} & \frac{\partial F_1}{\partial X_2} & \cdots & \frac{\partial F_1}{\partial X_n} \\ \frac{\partial F_2}{\partial X_1} & \frac{\partial F_2}{\partial X_2} & \cdots & \frac{\partial F_2}{\partial X_n} \\ \vdots & \vdots & \ddots & \\ \frac{\partial F_m}{\partial X_1} & \frac{\partial F_m}{\partial X_2} & \cdots & \frac{\partial F_m}{\partial X_n} \end{bmatrix} \tag{2.67}$$

From Equations (2.65) and (2.66), an update equation to iteratively solve for $\bar{X}$ is formulated as,

$$\bar{F}(\bar{X}^j) + D\bar{F}(\bar{X}^j) \cdot (\bar{X}^{j+1} - \bar{X}^j) = \bar{0} \tag{2.68}$$

where $||(\bar{X}^{j+1})|| < ||\bar{F}(\bar{X}^j)||$. Equation (2.68) is iteratively solved for $\bar{X}^{j+1}$ until a certain tolerance $\varepsilon$ is met, i.e.,

$$||\bar{F}(\bar{X}^{j+1})|| < \varepsilon \tag{2.69}$$

The update equation represented in Equation (2.68) takes different forms depending on the number of design variables and number of constraint equations in the problem. When $n = m$, i.e., the number of design variables is equal to the number of constraints, the matrix $D\bar{F}(\bar{X}^j)$ is a square matrix and is invertible. Therefore, one solution exists that is obtained by solving for $\bar{X}^{j+1}$ such that,

$$\bar{X}^{j+1} = \bar{X}^j - D\bar{F}(\bar{X}^j)^{-1}\bar{F}(\bar{X}^j) \tag{2.70}$$

In the case when $n > m$, i.e., the number of design variables is greater than the number of constraints, infinitely many solutions exist. One method of producing a unique solution is the minimum norm approach, resulting in the following form of the update equation,

$$\bar{X}^{j+1} = \bar{X}^{j} - D\bar{F}(\bar{X}^{j})^{T}\left[D\bar{F}(\bar{X}^{j}) \cdot D\bar{F}(\bar{X}^{j})^{T}\right]^{-1}\bar{F}(\bar{X}^{j}) \tag{2.71}$$

In the case when $n < m$, i.e., the number of design variables is less than the number of constraints, the system is considered to be overdetermined and no solutions exist. However, with the application of the method of least squares, an approximate solution is obtained [17]. In solving these equations iteratively, issues of importance include the radius of convergence, the speed of convergence, and the efficiency of the process; the number of iterations for the solution to converge impacts the result significantly.

### 2.4.1 Single Shooting

One implementation of a targeting algorithm is the single shooting method, which involves correcting a single trajectory arc to reach a desired state. Single shooting algorithms target any state or combination of states, but the focus of this investigation is targeting position over a variable time of flight, as illustrated in Figure 2.13. For a given initial position vector $\bar{r}_0 = [x_0\ y_0\ z_0]^T$ and initial velocity vector $\bar{v}_0 = [\dot{x}_0\ \dot{y}_0\ \dot{z}_0]^T$ at initial time $t_0$, the goal is to determine the $\Delta\bar{v}_0$ necessary to achieve the desired position $\bar{r}_d = [x_d\ y_d\ z_d]^T$ in time $t$. The state at the end of each propagation for time $t$ is denoted $\bar{x}_t = \bar{x}(\bar{x}_0, t)$. The design vector $\bar{X}$ for this example is then equal to,

$$\bar{X} = \begin{bmatrix} \dot{x}_0 \\ \dot{y}_0 \\ \dot{z}_0 \\ t \end{bmatrix} \tag{2.72}$$

and the constraint vector is given as,

$$\bar{F}(\bar{X}) = \begin{bmatrix} x_t - x_d \\ y_t - y_d \\ z_t - z_d \end{bmatrix} = \bar{0} \tag{2.73}$$

In this formulation, the Jacobian matrix $D\bar{F}(\bar{X})$ is a $3 \times 4$ matrix,

$$D\bar{F}(\bar{X}) = \begin{bmatrix} \frac{\partial x_t}{\partial x_0} & \frac{\partial x_t}{\partial y_0} & \frac{\partial x_t}{\partial z_0} & \frac{\partial x_t}{\partial t} \\ \frac{\partial y_t}{\partial x_0} & \frac{\partial y_t}{\partial y_0} & \frac{\partial y_t}{\partial z_0} & \frac{\partial y_t}{\partial t} \\ \frac{\partial z_t}{\partial x_0} & \frac{\partial z_t}{\partial y_0} & \frac{\partial z_t}{\partial z_0} & \frac{\partial t}{\partial t} \end{bmatrix} \tag{2.74}$$

In terms of the elements of the STM, this Jacobian matrix is rewritten as,

$$D\bar{F}(\bar{X}) = \begin{bmatrix} \phi_{14} & \phi_{15} & \phi_{16} & \dot{x}_t \\ \phi_{24} & \phi_{25} & \phi_{26} & \dot{y}_t \\ \phi_{34} & \phi_{35} & \phi_{36} & \dot{z}_t \end{bmatrix} \tag{2.75}$$

Since the number of design variables is greater than the number of constraints, a minimum norm solution is employed, and iterations ensue on the update equation represented in Equation (2.71) until the required tolerance is met.

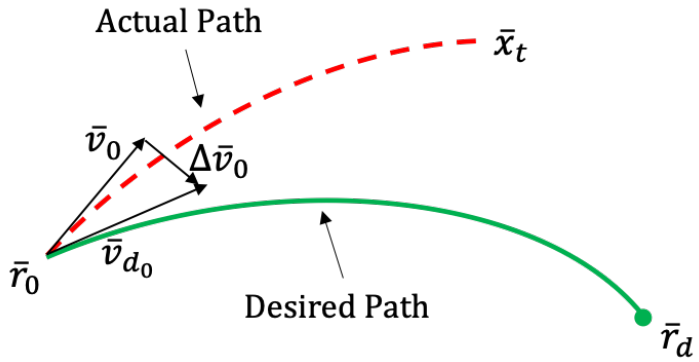


Figure 2.13. Schematic for a Variable Time Position Targeter.

**Computation of Symmetric Periodic Orbits**

Periodic solutions for the motion of the spacecraft in the vicinity of libration points are computed numerically by employing a similar targeting scheme. In a planar scenario, such periodic orbits, also labelled Lyapunov orbits, are symmetric across the $\hat{x}$-axis. The Mirror theorem, which states that if $n$-point masses are moving under their mutual gravitational forces, their orbits are periodic if – at two separate epochs – a mirror configuration occurs, aids in the computation of these orbits [18]. A consequence of this theorem is that the orbits only require propagation for half their periods, initiated at a perpendicular crossing where $\dot{x}_0$ and $y_0$ are equal to zero. Thus, the initial state vector is represented as $\bar{x}_0 = [x_0 \ 0 \ 0 \ 0 \ \dot{y}_0 \ 0]^T$. Then, the design vector and the constraint vectors are formulated as,

$$\bar{X} = [\dot{y}_0 \quad t] \tag{2.76}$$

$$\bar{F}(\bar{X}) = [\dot{x}_f \quad y_f] \tag{2.77}$$

where $t$ is the propagation time. The resulting Jacobian matrix for this problem is given as,

$$D\bar{F}(\bar{X}) = \begin{bmatrix} \frac{\partial \dot{x}_f}{\partial \dot{y}_0} & \frac{\partial \dot{x}_f}{\partial t} \\ \frac{\partial y_f}{\partial \dot{y}_0} & \frac{\partial y_f}{\partial t} \end{bmatrix} \tag{2.78}$$

Equation (2.70) is employed to iteratively solve for the design variables, since the number of constraints and design variables is equal. Figure 2.14 illustrates a corrected $L_1$ Lyapunov orbit in purple, along with the initial guess arc plotted in black.

### 2.4.2 Natural Parameter Continuation

The existence of a single periodic orbit as an isolated trajectory is not as insightful or useful towards trajectory design as a group of orbits with similar characteristics or geometries. Poincaré states that the computation of a single periodic orbit can lead to the determination of a set of periodic orbits, typically denoted a *family* [19]. Note that

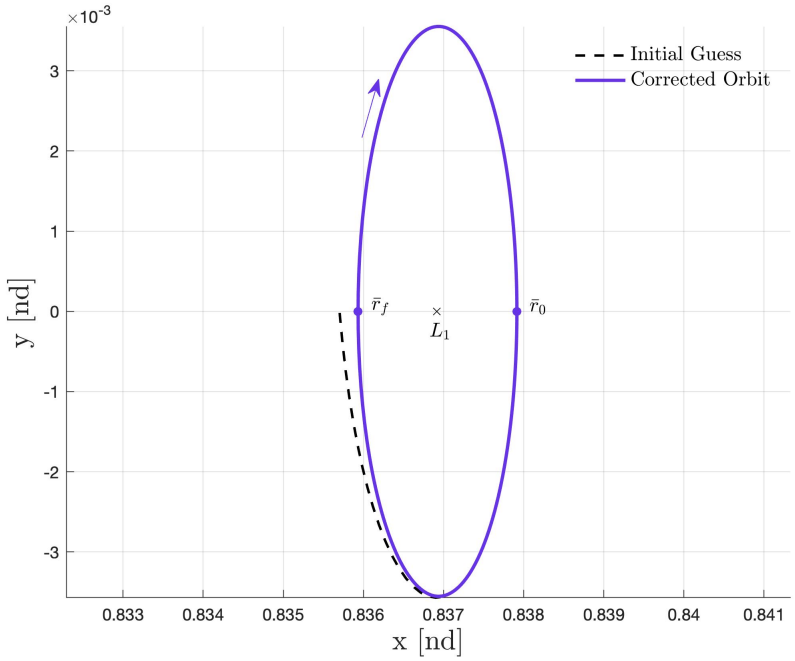


Figure 2.14. An $L_1$ Lyapunov Periodic Orbit in the Earth-Moon System.

a 'family' is certainly not unique. The process of continuation to produce a family of orbits offers valuable insight into the evolution of stability and energy characteristics across the orbits. The initial conditions corresponding to each member of a family of periodic orbits seeds the initial guess for each subsequent orbit. For instance, consider the $L_1$ Lyapunov orbit represented in Figure 2.14. Selecting the initial $x$ position as the natural parameter of interest, a sufficiently small perturbation in $x_0$ is applied to determine the next member in the family of $L_1$ Lyapunov orbits. This initial value of $x_0$ typically remains constant throughout the iteration process. Representative members of the $L_1$ Lyapunov Family are illustrated in Figure 2.15, with the color scheme corresponding to the value of Jacobi constant of each orbit.

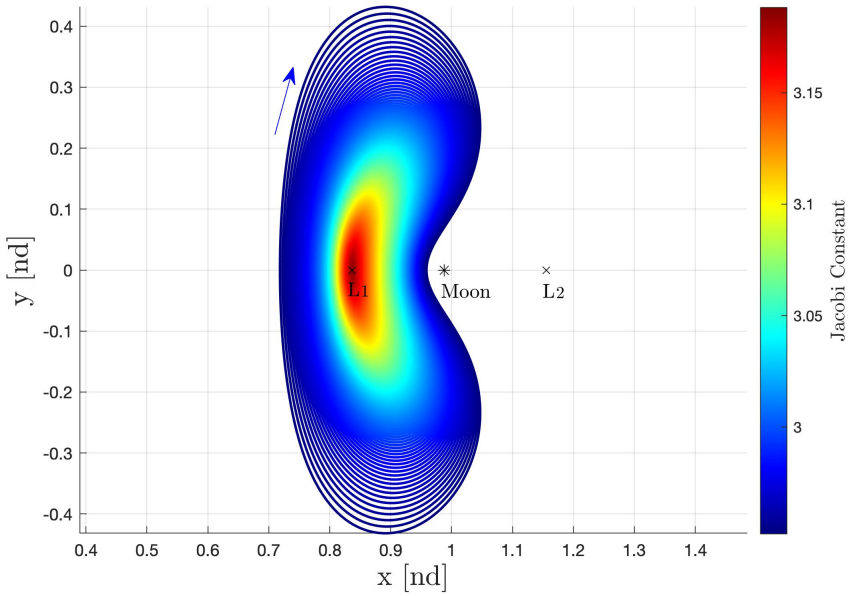


Figure 2.15. Representative Members from the Family of $L_1$ Lyapunov Periodic Orbits in the Earth-Moon System.

## 2.5 Coordinate Transformation

Although a major focus of this investigation is the visualization of trajectories in the rotating frame, the capability to plot in the inertial frame offers additional critical insight into the geometry of the trajectories [3], [4]. Recall the inertial and rotating frames defined in Figure 2.2, where the inertial frame $I$ is represented by the $\hat{X} - \hat{Y} - \hat{Z}$ axes and the rotating frame $R$ by the $\hat{x} - \hat{y} - \hat{z}$ axes. In the rotating frame, the position vector locating the body $P_3$ with respect to the barycenter $B$, in nondimensional coordinates, is defined as,

$$^{R}\bar{\rho} = x\hat{x} + y\hat{y} + z\hat{z} \tag{2.79}$$

The subscript $R$ in Equation (2.79) indicates the rotating frame. Similarly, in inertial coordinates, this position vector is expressed as,

$$^{I}\bar{\rho} = X\hat{X} + Y\hat{Y} + Z\hat{Z} \tag{2.80}$$

Also recall that the angle $\theta$ orients the rotating frame with respect to the inertial frame. Since the angular velocity of the primary system in the CR3BP, $\dot{\theta}$, is constant, the angle $\theta$ is rewritten in terms of nondimensional mean motion $n$ and nondimensional time $\tau$ as,

$$\theta = n(\tau - \tau_0) \tag{2.81}$$

where $\tau_0$ is the initial nondimensional time. The nondimensional mean motion is, by definition, equal to one, and that allows Equation (2.81) to be written explicitly in terms of nondimensional time. Next, the scalar inertial position coordinates $[X\ Y\ Z]^T$ are expressed in terms of the rotating coordinates as,

$$\begin{aligned} X &= xcos(\tau - \tau_0) - ysin(\tau - \tau_0) \\ Y &= xsin(\tau - \tau_0) + ycos(\tau - \tau_0) \\ Z &= z \end{aligned} \tag{2.82}$$

The direction cosine matrix $^{I}C^{R}(\tau)$ summarizes the relationship between the inertial and rotating coordinates and is formulated as,

$$\begin{bmatrix} \hat{X} \\ \hat{Y} \\ \hat{Z} \end{bmatrix} = {}^{I}C^{R}(\tau) \begin{bmatrix} \hat{x} \\ \hat{y} \\ \hat{z} \end{bmatrix} \tag{2.83}$$

where the matrix ${}^{I}C^{R}(\tau)$ is,

$$ {}^{I}C^{R}(\tau) = \begin{bmatrix} cos(\tau-\tau_0) & -sin(\tau-\tau_0) & 0 \\ sin(\tau-\tau_0) & cos(\tau-\tau_0) & 0 \\ 0 & 0 & 1 \end{bmatrix} \tag{2.84} $$

The velocity vector is transformed from rotating to inertial coordinates as well, but with the application of the Basic Kinematic Equation, as discussed in Equations (2.20)-(2.22). In terms of rotating and inertial coordinates, the expression for the inertial velocity vector is,

$$ {}^{I}\dot{\bar{\rho}} = \dot{X}\hat{X} + \dot{Y}\hat{Y} + \dot{Z}\hat{Z} \tag{2.85} $$

$$ {}^{I}\dot{\bar{\rho}} = (\dot{x}-y)\hat{x} + (\dot{y}+x)\hat{y} + \dot{z}\hat{z} \tag{2.86} $$

still expressed in terms of rotating coordinates. Employing again the direction cosine matrix ${}^{I}C^{R}(\tau)$, the velocity vector is transformed from rotating coordinates to inertial coordinates as,

$$ \begin{bmatrix} \dot{X} \\ \dot{Y} \\ \dot{Z} \end{bmatrix} = {}^{I}C^{R}(\tau) \begin{bmatrix} (\dot{x}-y) \\ (\dot{y}+x) \\ \dot{z} \end{bmatrix} \tag{2.87} $$

To transform a full six-element state vector from rotating to inertial coordinates, the ${}^{I}\dot{C}^{R}(\tau)$ matrix is first defined as,

$$ {}^{I}\dot{C}^{R}(\tau) = \dot{\theta} \begin{bmatrix} -sin(\tau-\tau_0) & -cos(\tau-\tau_0) & 0 \\ cos(\tau-\tau_0) & -sin(\tau-\tau_0) & 0 \\ 0 & 0 & 0 \end{bmatrix} \tag{2.88} $$

Here, recall that $\dot{\theta}$ is equal to the nondimensional mean motion and is, therefore, equal to one. Therefore, the transformation of position and velocity states together

from rotating coordinates to inertial coordinates is conveniently determined using one $6 \times 6$ matrix as,

$$\begin{bmatrix} X \\ Y \\ Z \\ \dot{X} \\ \dot{Y} \\ \dot{Z} \end{bmatrix} = \begin{bmatrix} {}^{I}C^{R}(\tau) & 0_{3\times3} \\ {}^{I}\dot{C}^{R}(\tau) & {}^{I}C^{R}(\tau) \end{bmatrix} \begin{bmatrix} x \\ y \\ z \\ \dot{x} \\ \dot{y} \\ \dot{z} \end{bmatrix} \tag{2.89}$$

where $0_{3\times3}$ is a zero matrix. To perform a coordinate transformation from inertial to rotating coordinates, the inverse of the $6 \times 6$ block matrix in Equation (2.89) is utilized.

# 3. BACKGROUND – RESONANT ORBITS

This investigation involves an in-depth analysis of resonant orbits and their characteristics in the CR3BP. The concept of resonance is introduced in this chapter, followed by the computation of resonant orbits in the two-body and three-body models. The difference between synodic and sidereal periods is also discussed. The methods involved in the calculation of families of planar and spatial resonant orbits are described, along with the theory of bifurcations and stability changes in the CR3BP. Finally, the invariant manifold theory and Poincaré maps are introduced.

## 3.1 Introduction to Resonance

The phenomenon of resonance is a direct consequence of subtle gravitational effects that determine the dynamical structure of the solar system. In general, resonance in a system occurs when there exists a simple numerical relationship between frequencies or periods [9], [15]. Within the scope of orbital mechanics, it is useful to analyze this relationship between planetary bodies and leverage it towards identifying favorable orbital characteristics. The basic theory behind orbital resonance is reviewed, along with the existence of resonant orbits in the two-body model and the various ways that these orbits are categorized.

### 3.1.1 Orbital Resonance

Orbital resonance is a result of any combination of orbital parameters, such as eccentricity and semi-major axis, or eccentricity and inclination. The impact of resonance on an orbit is observed on shorter time frames, such as the period of an orbit, or longer term, such as thousands or even millions of years. Some of the known

types of orbital resonances include mean motion resonance, Laplace resonance, Kozai resonance, and secular resonance [20]. The focus of this investigation is the phenomenon of orbit-orbit resonance, which occurs when the orbital periods of two or more bodies exist in a simple integer ratio. For two bodies in orbit-orbit resonance, the phenomenon is also labelled *mean motion resonance*; for three or more orbiting bodies that possess a simple integer ratio of their orbital periods, the phenomenon is termed *Laplace resonance*. These types of resonances occur among planets, satellites, and even asteroids with commensurate periods [9].

Consider two bodies $A$ and $B$, each of arbitrary mass orbiting a central body. Then, an orbit-orbit resonance is said to exist if the orbital periods of these bodies are described by a simple integer ratio $p : q$, or $T_B : T_A$, where $T_A$ and $T_B$ are the periods of bodies $A$ and $B$, respectively. The occurrence of resonance in a system can lead to long term stabilization of the orbits involved or, in some cases, destabilize the orbits. Within our solar system, stabilization has been observed in the orbits of Pluto and the Plutinos, which are a group of trans-Neptunian objects that form the inner part of the Kuiper belt. In spite of crossing the orbit of Neptune, the stable orbits of the Plutinos are attributed to a 2:3 orbit-orbit resonance with Neptune. This resonance ratio implies that for every two revolutions of a Plutino around the Sun, Neptune orbits the Sun three times. In another example, destabilization due to resonance accounts for the Kirkwood gaps in the asteroid belt between Mars and Jupiter, the locations corresponding to 3:1, 2:1, 5:2, and 7:3 mean-motion resonances with Jupiter [21]. The same phenomenon is also observed in the Cassini Division in the rings of Saturn, cleared out due to a 2:1 resonance with Saturn's moon Mimas.

### 3.1.2 Resonance in the Two-Body Model

Resonance in the two-body model serves as a foundation prior to moving on to the higher fidelity CR3BP. Closed-form solutions in the two-body model consist of elliptic, parabolic, and hyperbolic conic sections. For the purpose of this investigation,

elliptical orbits are the focus, that is, closed orbits in the inertial frame. Consider two massless bodies $A$ and $B$ in orbit around a central body with orbital periods equal to $T_A$ and $T_B$, respectively. In this instance, consider the central body to be the Earth, and let the body $A$ be the Moon. Define body $B$ as a spacecraft on an elliptical orbit around the Earth. Then, the spacecraft is moving in orbital resonance with the Moon around the Earth if the spacecraft completes $p$ orbits around the Earth in the same time that the Moon completes $q$ revolutions around the Earth, where $p$ and $q$ are positive integers. Mathematically, this relationship is expressed as,

$$\frac{p}{q} = \frac{N_p}{N_q} = \frac{T_q}{T_p} \tag{3.1}$$

where $T_q$ corresponds to the period of the Moon and $T_p$ corresponds to the period of the spacecraft. The values of $N_p$ and $N_q$ are the mean motions of the spacecraft and the Moon, respectively. In terms of two-body dimensional parameters, the mean motion $N_i$ for a conic section is defined as,

$$N_i = \sqrt{\frac{GM}{a_i^3}} \tag{3.2}$$

where $GM$ is the gravitational parameter associated with the central body, and $a_i$ is the semi-major axis of the associated orbit. Equations (3.1) and (3.2) yield a relationship between the resonance ratio and the semi-major axes of the two bodies in resonance:

$$\frac{p}{q} = \frac{N_p}{N_q} = \sqrt{\frac{a_q^3}{a_p^3}} \tag{3.3}$$

In the case of the Moon in resonance with a spacecraft orbiting the Earth, the knowledge of the semi-major axis of the Moon, $a_q$, aids in the computation of the semi-major axis of the spacecraft orbit, $a_p$, for a given resonance ratio $p : q$. The value of $a_p$ is then evaluated as,

$$a_p = \left(\frac{q^2 a_q^3}{p^2}\right)^{\frac{1}{3}} \tag{3.4}$$

To compute a resonant orbit in the two-body model, consider a spacecraft orbiting the Earth in a planar 3:4 mean motion resonance with the Moon. Since the focus is the two-body model, recall that the Moon is modeled as massless and does not influence the motion of the Earth. For reference, the two-body parameters corresponding to the lunar orbit are summarized in Table 3.1. Assume that the gravitational parameter value of the central body, Earth, to be equal to 398600.448 $km^3/s^2$. Then, the semi-major axis of the spacecraft orbit, $a_p$, is computed using Equation (3.4) with the ratio $p : q$ equal to 3:4. The value of $a_p$ is calculated to be 465653.11 km.

Table 3.1. Orbital Parameters of the Moon in the Two-Body Model.

| **Parameter** | **Value** |
|---|---|
| Semi-major Axis, $a_q$ | $384,338.174$ km |
| Period, $T_q$ | 27.45 days |
| Inclination, $i_q$ | $0^\circ$ |
| Eccentricity, $e_q$ | 0 |

The initial state vector for the resonant orbit in the two-body inertial frame is of the form ${}^I\bar{X}_{0,2B} = [X_0\ Y_0\ Z_0\ \dot{X}_0\ \dot{Y}_0\ \dot{Z}_0]^T$. Since the resonant orbit is planar, the initial values $Z_0$ and $\dot{Z}_0$ are equal to 0. Assuming that at $t = 0$, the spacecraft is located at one of the apses; the initial position in the $\hat{Y}_{2B}$ direction and the initial velocity in the $\hat{X}_{2B}$ direction are equal to 0, i.e., $Y_0 = 0$ and $\dot{X}_0 = 0$. The eccentricity of the orbit of the spacecraft is selected such that at the initial time, the spacecraft lies between the Earth and the Moon. In this case, the eccentricity is selected as $e_p = 0.7853$, which corresponds to a spacecraft periapsis distance of $r_{p_q} = 100000\ km$. Thus, the initial position along the $\hat{X}_{2B}$ direction is $X_0 = 100000\ km$. Then, the magnitude of the initial velocity is determined as,

$$v_0 = \sqrt{2GM\left(\frac{1}{r_0} - \frac{1}{2a_p}\right)} \tag{3.5}$$

where $GM$ is the gravitational parameter associated with the Earth, and $r_0$ is the magnitude of initial position. Recall that the components of velocity in the $\hat{X}_{2B}$ and $\hat{Z}_{2B}$ directions are zero. Thus, using Equation (3.5), the final component of the initial state vector, $\dot{Y}_0$, is determined to be equal to 2.6676 $km/s$. The resonant orbit that results from these initial states in the two-body inertial frame is illustrated in Figure 3.1. The orbit of the spacecraft is plotted in purple, while the dashed black curve represents the orbit of the Moon. A distinct geometry, however, arises when the resonant orbit is viewed in the rotating frame. The $\hat{x}_{2B}$ axis in the rotating frame is defined along the position vector from the Earth to the Moon, $\hat{z}_{2B}$ is defined parallel to the angular momentum vector, and $\hat{y}_{2B}$ completes the dextral orthogonal triad. The initial state is then transformed into rotating coordinates using Equation (2.74), and the resulting geometry is illustrated in Figure 3.2. In the rotating view, the orbit of the spacecraft appears in purple. As a consequence of the definition of the rotating frame, the lunar orbit appears as a fixed point.

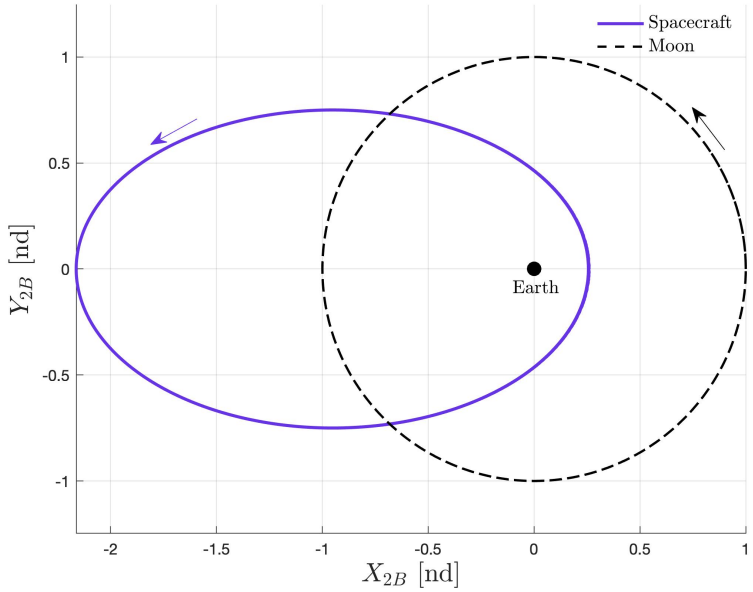


Figure 3.1. The 3:4 Resonant Orbit in the Earth-Moon Two-Body Inertial Frame.

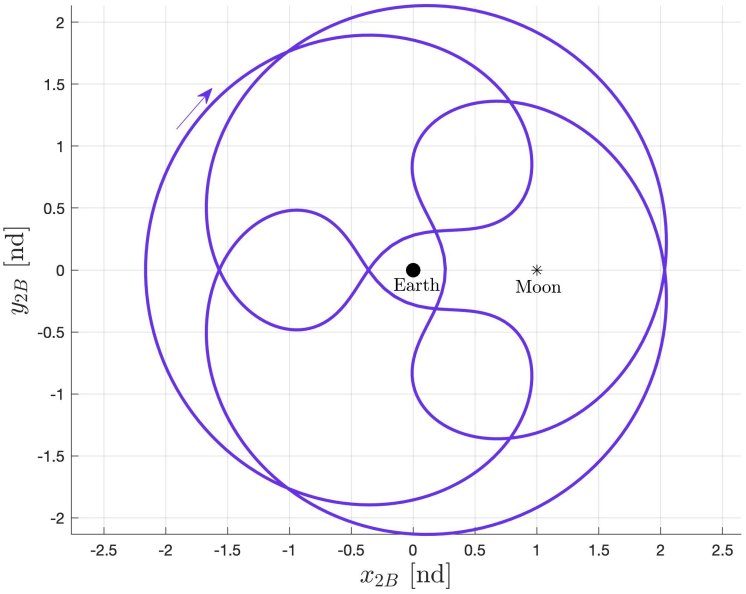


Figure 3.2. The 3:4 Resonant Orbit in the Earth-Moon Two-Body Rotating Frame.

Recall that for a 3:4 resonance ratio, the spacecraft orbits the Earth three times in the same interval required for the Moon to orbit the Earth four times. A stark difference between the inertial and rotating frame views of the resonant orbit is the formation of loops in the latter. The three loops in the orbit correspond to the value of $p$ in the $p:q$ resonant ratio for this orbit, and represent the periapse passes along the orbit. At the location of these loops, the velocity of the spacecraft around the Earth is faster than the velocity of the Moon in its orbit, a fact that renders the spacecraft to seemingly reverse its direction of motion in orbit. Another important feature of the rotating view is associated to the relative alignment of the Earth, the Moon, and the spacecraft. This phenomenon is termed a conjunction, and it occurs when the three bodies are aligned. The rotating view offers insight into the frequency of these conjunctions, which occur when the spacecraft intersects the $\hat{x}$-axis.

### Interior and Exterior Resonances

Depending on the resonance ratio, resonant orbits are classified as *interior* or *exterior* resonances. For an integer resonance ratio of $p : q$, orbits with $p > q$ are labelled interior resonant orbits and their orbital periods are smaller than the period of the Moon. For cases where $p < q$, the orbits are denoted exterior resonant orbits and their periods are larger than the period of the Moon.

### Sidereal and Synodic Periods

Another category of resonant orbits originates from the type of orbital period in consideration. The two types of periods are *sidereal* and *synodic* periods [22]. The sidereal period is the time required for a celestial body to complete a 360° revolution around its central axis in the inertial frame, while a synodic period is defined as the time interval necessary for a celestial body to complete a revolution and return to the same orientation relative to another body. For instance, in the case of the Moon orbiting the Earth, the sidereal period is roughly 27.32 days. In contrast, the synodic period of the Moon is 29.53 days, and is equal to the length of time for the Moon to return to the same orientation with respect to the Sun. Depending on the period of the orbit, a sidereal or synodic resonance with another orbiting body might be available.

## 3.2 Resonance in the CR3BP

The determination of resonant orbits in the higher-fidelity CR3BP builds upon resonant orbits as computed in the two-body model. However, one major distinction that arises between resonant orbits in the two models is the difference in resonance ratios. For resonant orbits in the two-body model with perfect integer resonance ratios, the equivalent orbits in the CR3BP no longer possess precise integer ratios, but approximate rational fractions. Thus, for $p : q$ resonant orbits in the CR3BP, $P_3$

complete $p$ orbits around $P_1$ in *approximately* the time required for $P_2$ to complete $q$ orbits around $P_1$. However, it is noted that such orbits in the CR3BP are precisely periodic.

Consider the 3:4 resonant orbit in the Earth-Moon two-body rotating frame illustrated in Figure 3.2. The computation of the equivalent 3:4 resonant orbit in the Earth-Moon CR3BP rotating frame originates from the two-body orbit. However, recall that the two-body model assumes the Moon to be massless, which is no longer true in the CR3BP. Consequently, the additional gravitational effects of $P_2$ perturb the orbit in the CR3BP and initially results in an orbit that is not periodic. Therefore, the initial conditions corresponding to the periodic orbit in the two-body model require adjustments via differential corrections for the computation of its analog in the CR3BP. To illustrate this process, recall the six-element dimensional initial conditions for the 3:4 resonant orbit in the two-body inertial frame as computed earlier,

$$ {}^{I}\bar{X}_{0,2B} = [\ 100000\ km\ \ 0\ \ 0\ \ 0\ \ 2.6676\ km/s\ \ 0\ ]^T \tag{3.6} $$

These states, when converted to the two-body rotating frame, result in the state,

$$ {}^{R}\bar{X}_{0,2B} = [\ 100000\ km\ \ 0\ \ 0\ \ 0\ \ 2.4010\ km/s\ \ 0\ ]^T \tag{3.7} $$

The initial state vector in Equation (3.7) then is converted into rotating CR3BP nondimensional coordinates, along with a coordinate shift to the Earth-Moon barycenter at the origin. The characteristic quantities $l^*$, $m^*$, and $t^*$ are employed to nondimensionalize the states, and the origin is shifted by $\mu$ in the $-\hat{x}$-direction. The resulting nondimensional rotating CR3BP state is,

$$ {}^{R}\bar{x}_0 = [\ 0.2480\ \ 0\ \ 0\ \ 0\ \ 2.3435\ \ 0\ ]^T \tag{3.8} $$

Propagating the initial state in Equation (3.8) for one period, corresponding to the two-body resonant orbit, using the CR3BP nonlinear equations of motion results in a

trajectory that is neither closed nor periodic in the rotating frame. In several resonant orbits, there also exist multiple crossings of the $\hat{x}$-axis, not all perpendicular. To implement a targeting scheme to successfully compute an orbit with multiple $\hat{x}$-axis crossings sometimes requires knowledge of the geometry of the orbit; such information is available from the two-body generating orbit. The number of crossings are then seeded into the targeter, which terminates numerical propagation at the appropriate crossing. However, when this information is not available a priori, the approximate period of the resonant orbit is utilized to terminate integration at approximately half the period along the resonant orbit. The single shooting scheme employed in the computation of the $L_1$ Lyapunov orbits in Chapter 2 is adopted to correct resonant trajectories. The initial state represented in Equation (3.8) is employed as an initial guess for the targeter. Correcting the six-element nondimensional initial state in the CR3BP rotating frame yields,

$$^{R}\bar{x}_{0,corr} = [\ 0.2480 \quad 0 \quad 0 \quad 0 \quad 2.3496 \quad 0\ ]^T \tag{3.9}$$

In dimensional units, this initial state vector is rewritten as,

$$^{R}\bar{x}_{0,corr} = [\ 95329.46\ km \quad 0 \quad 0 \quad 0 \quad 2.4073\ km/s \quad 0\ ]^T \tag{3.10}$$

The corrected resonant orbit is illustrated in Figure 3.3. Note that the orbits are plotted on nondimensional axes. The corrected CR3BP orbit is plotted in purple, while the dashed orbit corresponds to the two-body initial guess propagated using the nonlinear CR3BP equations of motion. The corrected orbit possesses a period of 109.65 days and a Jacobi constant value equal to 2.168.

## 3.3 Families of Planar Resonant Orbits

The computation of one resonant orbit in the CR3BP guarantees the existence of a family of resonant orbits. The process of natural parameter continuation (in Section

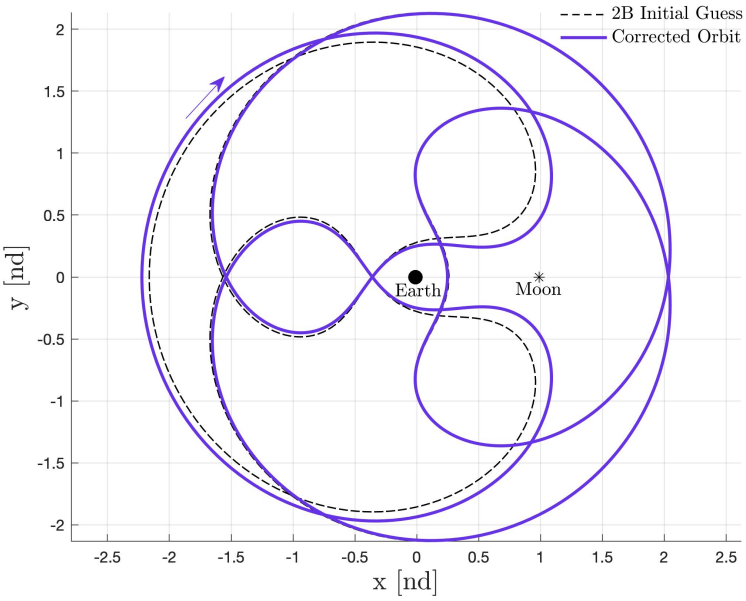


Figure 3.3. The 3:4 Resonant Orbit in the Earth-Moon CR3BP Rotating Frame.

2.4.2) is employed to generate families of resonant orbits, with the initial position in the $\hat{x}$ direction as the natural parameter of interest. A family of 3:4 resonant orbits in the Earth-Moon system, constructed with natural parameter continuation, is illustrated in Figure 3.5(c). The same continuation scheme, together with the corrections process leveraging two-body initial guesses for various resonant ratios in the CR3BP, is used to evolve several families of orbits corresponding to different resonances in the Earth-Moon system. Representative members of these resonant families are illustrated in Figures 3.4-3.5, with each member colored according to its value of Jacobi constant. The corrected nondimensional initial states, values of Jacobi constant, and dimensional periods for selected orbit members from each resonant family are summarized in Table 3.2.

Table 3.2. Initial Conditions for Selected Planar Resonant Orbits in the Earth-Moon System.

| **Resonance Ratio** | $x_0$ $[nd]$ | $\dot{y}_0$ $[nd]$ | $C$ | **Period [days]** |
|---|---|---|---|---|
| 1:1 | 0.16686 | 2.99389 | 2.13068 | 27.26688 |
| 1:2 | 0.17166 | 3.00312 | 1.78911 | 54.48454 |
| 1:3 | 3.34922 | -3.01527 | 2.72353 | 77.78698 |
| 1:4 | 4.18667 | -3.90141 | 2.78529 | 109.29229 |
| 2:1 | 0.19987 | 2.56951 | 2.78693 | 27.23629 |
| 2:3 | 0.27385 | 2.20322 | 2.16282 | 81.48373 |
| 3:1 | -0.87594 | 0.37515 | 2.92681 | 27.27912 |
| 3:2 | 0.44416 | 1.29134 | 2.90416 | 54.31372 |
| 3:4 | 0.33752 | 1.86475 | 2.32417 | 108.71706 |
| 3:5 | 0.487234 | 1.32669 | 2.48211 | 135.34218 |
| 4:1 | 0.10252 | 3.72303 | 3.40649 | 27.26631 |
| 4:3 | 1.18945 | -0.69908 | 2.69085 | 79.45508 |

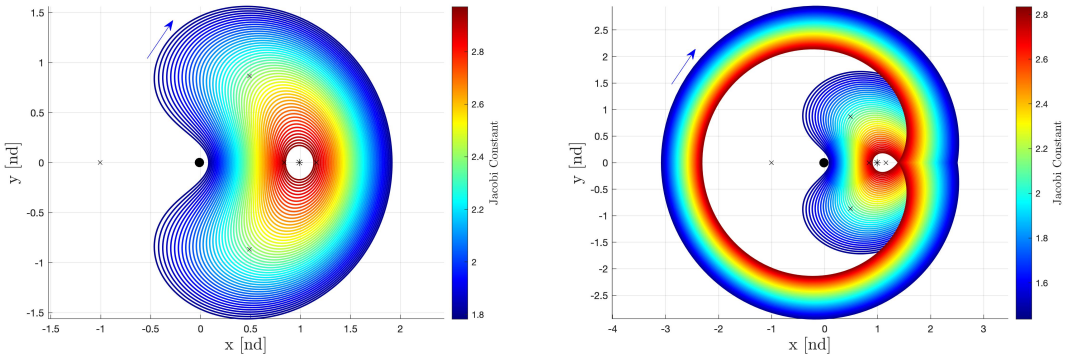


(a) 1:1 Resonance




(b) 1:2 Resonance

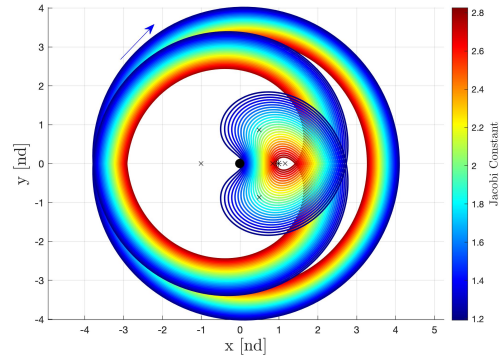


(c) 1:3 Resonance

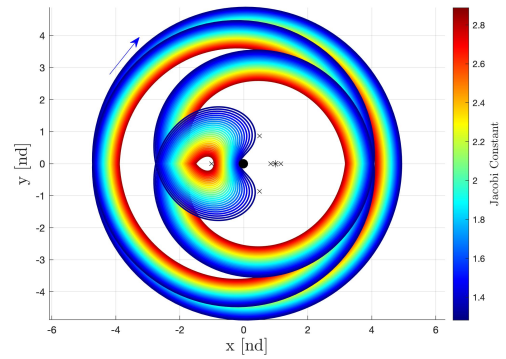


(d) 1:4 Resonance

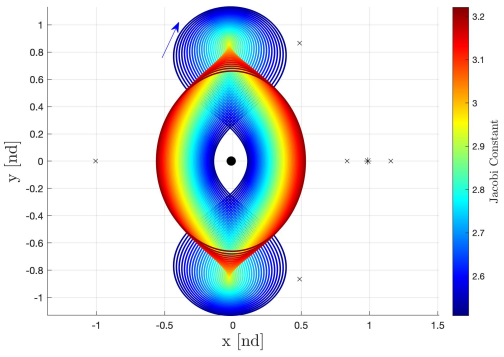


(e) 2:1 Resonance

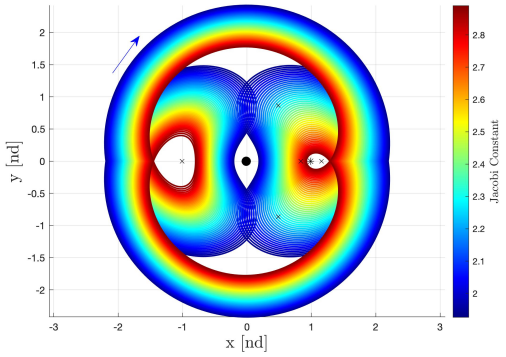


(f) 2:3 Resonance

Figure 3.4. Members of Planar Resonant Orbit Families in Configuration Space in the Earth-Moon CR3BP Rotating Frame.

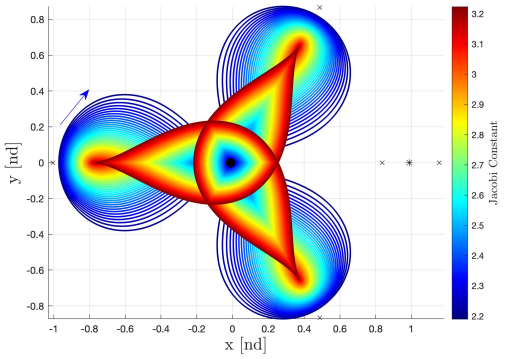


(a) 3:1 Resonance

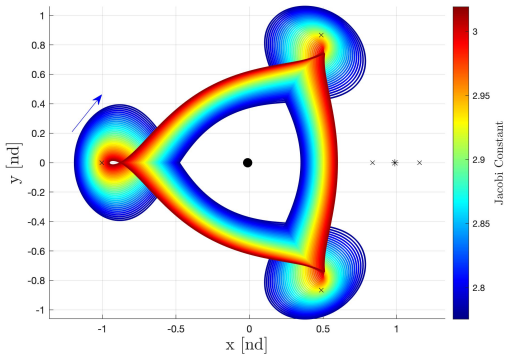


(b) 3:2 Resonance

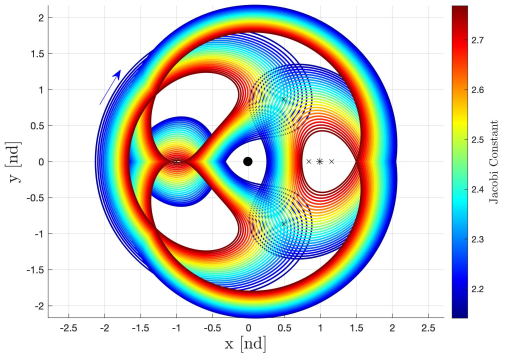


(c) 3:4 Resonance

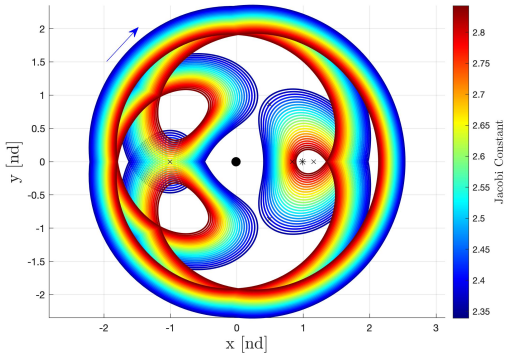


(d) 3:5 Resonance

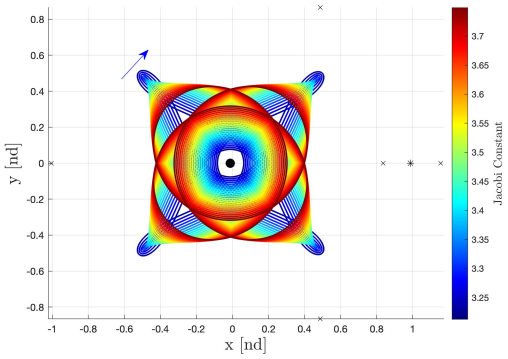


(e) 4:1 Resonance

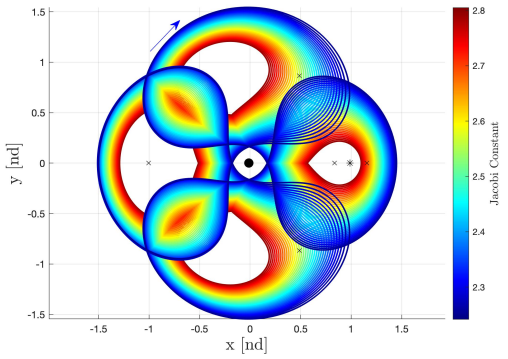


(f) 4:3 Resonance

Figure 3.5. Members of Planar Resonant Orbit Families in Configuration Space in the Earth-Moon CR3BP Rotating Frame.

### 3.3.1 End of a Family

The sections representing bounded regions along the resonant orbit families as illustrated in Figures 3.4-3.5 suggest an *end* to a family of orbits. To consider the possible outcomes that define the end of a family, first consider the visualization of an orbit hodograph. At a given value of $\mu$, the hodograph is defined such that each point represents a periodic orbit, and a family of periodic orbits is represented by a curve. This curve corresponding to a family of orbits in orbit space is termed a *characteristic*. Hénon [19] discusses that, upon continuing a family of orbits beyond a certain finite set, two cases arise in accordance with the Principle of Natural Termination [23]:

- The family closes in on itself. This occurs when the characteristic corresponding to the family is a closed curve; such families are termed closed families.
- For the evolution of quantities such as the Jacobi constant or the period along the family, those quantities grow without limits in each of the two directions. This infinite growth is denoted natural termination, and such families are labelled open families.

The Principle of Natural Termination applies to periodic solutions, and not specifically periodic orbits. In some cases, it might be observed that orbits in a family, especially those closer to the libration points, shrink into the points themselves. Analytically, however, the family may still be continued beyond the libration point, which returns the same periodic solutions with a shift in time by half the period of the orbit. Continuing the family further returns the same periodic solutions, and the family of orbits essentially returns over itself. This occurrence is termed a *reflection* of the family [24]. In theory, then, a family of periodic orbits can be characterized in four possible ways:

- A closed family with no reflections, where the characteristic is a closed curve.
- A closed family with two reflections, where the characteristic shifts back and forth along a finite curve as the family evolves.

- An open family with no reflections, where the characteristic goes to infinity in both directions.
- An open family with one reflection, where the characteristic goes to infinity in one direction and ends in a point in the other.

Characterizing orbit families as such provides useful insight into the evolution of orbital characteristics and quantities along a family.

## 3.4 Stability of Periodic Orbits

With the availability of periodic resonant orbits in the CR3BP, the next step is an understanding of the behavior of these orbits to leverage their characteristics towards spacecraft trajectory design. One variable that offers useful insight is the linear stability of an orbit and its evolution across a family. The linear stability of a periodic orbit is associated to its state transition matrix (STM), with elements that change along an orbit. Thus, it is necessary to investigate the properties of the full cycle STM, that is, the STM at precisely one full period along an orbit; it is also termed the monodromy matrix. For an orbit of period $T$, the monodromy matrix is represented as $\phi(T, 0)$ or $\phi(T + t_0, t_0)$. The matrix is computed originating from any point along an orbit. The six eigenvalues of the monodromy matrix, $\lambda_j$, possess a constant value along the orbit. Since the CR3BP is a time-invariant system, Lyapunov's Theorem applies, which is stated [25] as,

**Theorem 3.4.1 (Lyapunov's Theorem)** *If $\lambda$ is an eigenvalue of the monodromy matrix $\phi(T + t_0, t_0)$ of a time invariant system, then $\lambda^{-1}$ is also an eigenvalue, with the same structure of elementary divisors.*

At least one eigenvalue from the monodromy matrix in the CR3BP is equal to one, owing to the periodic nature of the orbit. Coupled with Theorem 3.4.1, it is apparent that at least two eigenvalues from the monodromy matrix of a periodic orbit are equal to one. This pair of eigenvalues is also identified as the trivial pair. Since the

monodromy matrix is real, if any of the four remaining eigenvalues are complex, they occur in complex conjugate pairs, represented as $\lambda_j = a \pm bi$. If the magnitude of the real part of such eigenvalues is greater than one, the resulting solution is unstable; if the magnitude of the real part is less than or equal to one, the resulting solution is labelled linearly stable. Solely imaginary eigenvalues of the form $\lambda_j = \pm bi$ correspond to oscillatory motion; the solution neither grows or decays over time [26], [16]. In summary, the following three cases occur that determine the linear stability of the periodic orbit:

- **Unstable Eigenvalues**: If $|\lambda_j| > 1$, then the eigenvalue is unstable, and the periodic orbit is defined as unstable. These eigenvalues lie outside the unit circle, and any perturbation along the orbit grows with time.
- **Stable Eigenvalues**: If $|\lambda_j| < 1$, then the eigenvalue is stable. These eigenvalues lie inside the unit circle, and any perturbation along the orbit tends to zero as time increases along the orbit.
- **Marginally Stable Eigenvalues**: If $|\lambda_j| = 1$, then the eigenvalue is marginally stable. These eigenvalues lie on the unit circle.

Figure 3.6 illustrates the location of each type of eigenvalue on the unit circle, as plotted on the complex plane. The green region corresponds to stable eigenvalues, the red to unstable eigenvalues, and the blue perimeter of the unit circle corresponds to marginally stable eigenvalues in the linear sense. Note that the existence of even one unstable eigenvalue renders the orbit unstable. For stability, however, all eigenvalues of the monodromy matrix are required to be stable. Nonetheless, due to the reciprocal nature of eigenvalues in the CR3BP, the existence of a stable eigenvalue guarantees the existence of a corresponding unstable eigenvalue. Therefore, only unstable and marginally stable orbits – those with all eigenvalues equal to one – are known to exist in the CR3BP. Consider the 3:4 resonant orbit plotted in Figure 3.3 in the Earth-Moon CR3BP rotating frame. The eigenvalues determined from the monodromy matrix for this orbit are listed in Table 3.3. Note that the eigenvalues do occur in reciprocal

pairs, with one pair of trivial eigenvalues. Since one of the eigenvalues, $\lambda_3$, is greater than unity in magnitude, the orbit is unstable.

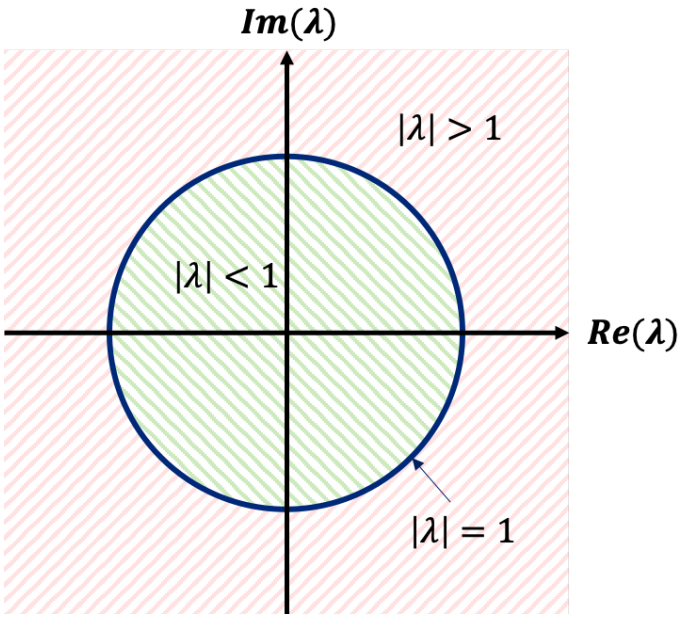


Figure 3.6. Possible Locations of $\lambda_j$ in the Complex Plane.

Table 3.3. Eigenvalues of the Monodromy Matrix of the 3:4 Resonant Orbit in the Earth-Moon System.

| | | | |
|---|---|---|---|
| $\lambda_1$ | 1.00000 | $\lambda_2$ | 1.00000 |
| $\lambda_3$ | 5.80849 | $\lambda_4$ | 0.17216 |
| $\lambda_5$ | $0.94686 + 0.32164$ | $\lambda_6$ | $0.94686 - 0.32164$ |

Another useful measure of the stability of an orbit is the *stability index*, $\nu$, which is a function of the eigenvalues from the monodromy matrix, $\lambda_j$ [27], [22]. The value of $\nu$ is computed as,

$$\nu = \frac{1}{2}\left(\lambda_j + \frac{1}{\lambda_j}\right) \tag{3.11}$$

For any periodic orbit, there exist three stability indices that arise from the six eigenvalues of the monodromy matrix. For the 3:4 resonant orbit in Figure 3.3, these three stability indices are computed as,

$$\begin{aligned} \nu_1 &= 1 \\ \nu_2 &= 2.99033 \\ \nu_3 &= 1.05201 \end{aligned} \tag{3.12}$$

The stability index is an insightful metric in evaluating the evolution of the nontrivial eigenvalues for each orbit across a family, since the evolution of stability is more apparent. The magnitude of the stability index itself is informative towards evolution of the stability properties of an orbit, where larger magnitudes indicate faster departure from the vicinity of the reference orbit.

## 3.5 Bifurcations

Analyzing the stability index for a family of periodic orbits leads to the concept of *bifurcations* and *bifurcating orbits*. By definition, a bifurcation occurs when there is a change in the form or character of the orbital stability across a family [26]. For instance, such changes occur when the stable or marginally stable eigenvalues of a periodic orbit cross the unit circle, causing the corresponding eigenvalues of orbits further along the family to become unstable. Qualitative changes such as these result in the formation of bifurcating orbits, possibly signaling new families of periodic solutions or, in some cases, delivering the end of a family of solutions. When a new family arises as a consequence of a bifurcation, the bifurcating orbit is common to both families. There are three ways [28] in which a change in the stability properties of a family of periodic orbits can signal the occurrence of a bifurcation:

- **Tangent Bifurcation:** A pair of eigenvalues moves along the unit circle and collides at the value +1 on the real axis, and then continues to the real axis, as

illustrated in Figure 3.7(a). One specific type of a tangent bifurcation, denoted a *cyclic fold*, does not result in the formation of a new family of periodic solutions.

- **Period Doubling Bifurcation:** A pair of eigenvalues moves along the unit circle and collides at the value -1 on the real axis; then the eigenvalue shifts to the real axis, as illustrated in Figure 3.7(b).
- **Secondary Hopf Bifurcation:** Two pairs of eigenvalues collide on the unit circle and split into the complex plane, as illustrated in Figure 3.7(c). This behavior is typically termed a Krien collision.

By investigating the eigenvalues from the monodromy matrix for various orbits along a family, bifurcations are identified.

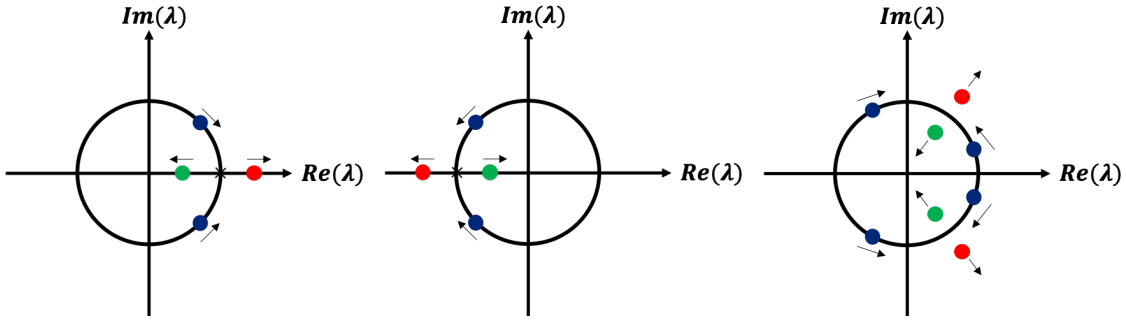


(a) Tangent Bifurcation (b) Period Doubling Bifurcation (c) Secondary Hopf Bifurcation

Figure 3.7. Change in Eigenvalue Structure associated with each type of Bifurcation.

## 3.6 Three-Dimensional Resonant Orbits

The computation of planar resonant orbit families and the determination of their stability properties enables the search for three-dimensional resonant orbit families [29]. The availability of such solutions opens additional dynamically viable regions for spacecraft pathways at a given value of the Jacobi constant. To determine spatial families of resonant orbits, the eigenvalue structure along their planar analogs is

investigated in search of bifurcating orbits. Specifically, certain tangent bifurcations from planar resonant families are known to bifurcate into spatial resonant families [15].

Once the bifurcating orbit is identified, a slight perturbation in the initial state corresponding to the orbit is introduced in the $z$-direction. Then, the initial state to construct the first spatial orbit is of the form $\bar{x}_0 = [x_0 \;\; 0 \;\; \Delta z \;\; 0 \;\; \dot{y}_0 \;\; 0]^T$, where $\Delta z$ is the slight perturbation in the $z$-direction. This perturbed state is corrected for periodicity using a three-dimensional targeting scheme focused on perpendicular crossings, during which the value of the initial position in the $z$-direction is fixed at a constant value. Following a strategy of natural parameter continuation, as employed in the computation of planar families of resonant orbits, families of spatial resonant orbits are produced as well. Each subsequent orbit in the family is incremented by a fixed value in the $z$-direction, and the resulting initial state is corrected. Increments in the positive $z$-direction result in *northern* spatial resonant orbits, while stepping in the negative $z$-direction results in *southern* spatial resonant orbits. Selected families of three-dimensional resonant orbits as plotted in the CR3BP rotating frame are illustrated in Figure 3.8. Table 3.4 summarizes the initial conditions, values of the Jacobi constant, and the periods for selected members from each family of spatial resonant orbits.

## 3.7 Invariant Manifold Theory

Solutions to differential equations are explored via classical analysis techniques and a global geometric approach. The former, which involves analyzing individual trajectories and their properties, is detailed in the previous sections. The latter approach is based in the phase space of a dynamical system, and involves understanding the global behavior of the flow. The structure and geometry of the phase space is investigated by considering equilibrium points and periodic solutions as well as the local flow associated with these particular solutions [25]. The knowledge of the flow structure is frequently leveraged towards trajectory design, especially involving un-

Table 3.4. Initial Conditions for Selected Spatial Resonant Orbits in the Earth-Moon System.

| **Resonance Ratio** | $x_0$ $[nd]$ | $z_0$ $[nd]$ | $\dot{y}_0$ $[nd]$ | $C$ | **Period [days]** |
|---|---|---|---|---|---|
| 1:1 | 0.23194 | -0.04950 | 2.39606 | 2.27756 | 27.17505 |
| 1:2 | 0.86671 | -0.09899 | 0.58415 | 2.79918 | 49.90111 |
| 1:3 | 3.30648 | -0.49499 | -2.96886 | 2.71778 | 78.56741 |
| 2:1 | 0.18779 | -0.00099 | 2.68094 | 2.75952 | 27.24767 |
| 2:3 | 0.89202 | -0.09899 | 0.53269 | 2.86043 | 75.52696 |
| 3:1 | -0.77817 | -0.09899 | 0.05450 | 3.17423 | 27.18625 |
| 3:2 | 0.42394 | -0.09899 | 1.33542 | 2.85688 | 54.33685 |
| 3:4 | 0.90596 | -0.09899 | 0.51463 | 2.88458 | 101.89412 |
| 3:5 | 0.88019 | -0.09899 | 0.54910 | 2.83993 | 130.64942 |

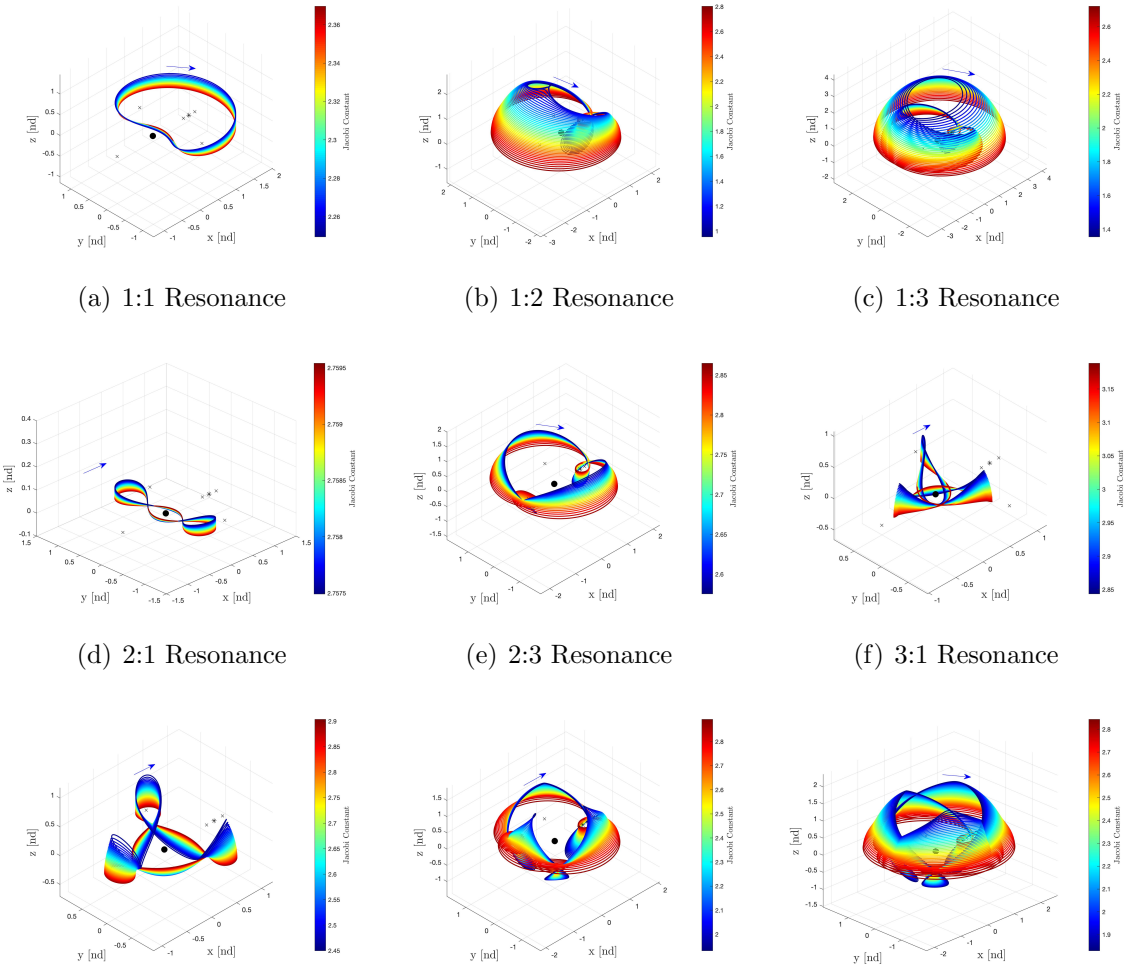


(a) 1:1 Resonance (b) 1:2 Resonance (c) 1:3 Resonance

(d) 2:1 Resonance (e) 2:3 Resonance (f) 3:1 Resonance

(g) 3:2 Resonance (h) 3:4 Resonance (i) 3:5 Resonance

Figure 3.8. Members of Spatial Resonant Orbit Families in the Earth-Moon CR3BP Rotating Frame.

stable orbits [30]. The following sections introduce the invariant manifold theory and the methodology to compute stable and unstable manifolds for fixed points and periodic orbits.

### 3.7.1 Manifolds of Fixed Points

Consider the equilibrium solutions in the CR3BP, represented by $L_i$ and state $\bar{x}_L$. The trajectories with initial conditions near $\bar{x}_L$, i.e., $\bar{x} = \bar{x}_L + \delta\bar{x}$, represent the phase portrait of the flow near $L_i$. This phase portrait is obtained by linearizing the nonlinear equations about $L_i$ such that,

$$\delta\dot{\bar{x}}(\tau) = A\delta\bar{x}(\tau) \tag{3.13}$$

where $A$ is the Jacobian matrix evaluated at $L_i$, and is constant. The solution, then, to Equation (3.13) is derived as,

$$\delta\bar{x}(\tau) = e^{A(t-t_0)}\delta\bar{x}(\tau_0) \tag{3.14}$$

Assuming that the matrix $A$ possesses $n$ distinct eigenvalues and $n$ linearly independent eigenvectors, Equation (3.14) is rewritten as,

$$\delta\bar{x}(\tau) = \sum_{j=1}^{n} c_j e^{\lambda_j(t-t_0)}\bar{v}_j \tag{3.15}$$

where $c_j$ are the coefficients determined using initial conditions, $\lambda_j$ are the eigenvalues of the $A$ matrix, and $\bar{v}_j$ are the corresponding eigenvectors. The eigenvalues of $A$, $\lambda_j$, are characteristic multipliers of the local flow that determine the linear stability of the equilibrium points. Depending on the form of the eigenvalues, the following three cases occur [11]:

- $\mathbf{\Re[\lambda_j] < 0}$ **for all** $\boldsymbol{\lambda_j}$: Sufficiently small perturbations tend to zero as $t \to \infty$. The equilibrium point is asymptotically stable.

- $\mathbf{\Re[\lambda_j] > 0}$ **for all** $\boldsymbol{\lambda_j}$: Any perturbation grows as $t \to \infty$. The equilibrium point is unstable.

- $\mathbf{\Re[\lambda_i] < 0}$ **and** $\mathbf{\Re[\lambda_j] > 0}$: The equilibrium point is non-stable and is a saddle point.

Stable or unstable points with no complex eigenvalues are denoted as *nodes*. An equilibrium point is *hyperbolic* if all the eigenvalues of $A$ possess non-zero real parts [31]. In addition to the eigenvalues, the eigenvectors associated with each $\lambda_j$ are used to introduce the linear subspaces of $\mathbb{R}^n$. Consider the $n$ distinct eigenvalues of $A$; let $n_s$ be the eigenvalues with negative real parts, $n_u$ be the eigenvalues with positive real parts, and $n_c$ be the eigenvalues without real parts, such that:

$$n = n_s + n_u + n_c \tag{3.16}$$

Then, the eigenvectors associated with each $\lambda_j$ are linearly independent and, therefore, span $\mathbb{R}^n$. Thus, $\mathbb{R}^n$ is represented in terms of three fundamental spaces, $E^S$, $E^U$, and $E^C$, which are the invariant subspaces corresponding to the linearized system. The subspaces $E^S$, $E^U$, and $E^C$ are termed the stable, unstable, and center subspaces, respectively. Their invariance arises from the fact that a solution that exists initially in a given subspace remains in that subspace for all time. This concept leads to the definitions of local stable, unstable, and center manifolds [32]. For an equilibrium solution represented by $\bar{x}_L$, i.e.,

- **Local Stable Manifold,** $\boldsymbol{W^S_{loc}}$, is the local stable manifold associated with $\bar{x}_L$. It is the set of all initial conditions in the vicinity of $\bar{x}_L$, such that flow initiated at these states asymptotically approach $\bar{x}_L$ as $t \to \infty$.

- **Local Unstable Manifold,** $\boldsymbol{W^U_{loc}}$, is the local unstable manifold associated with $\bar{x}_L$. It is the set of all initial conditions in the vicinity of $\bar{x}_L$, such that flow initiated at these states asymptotically approach $\bar{x}_L$ as $t \to -\infty$.

Recall that an equilibrium point is termed hyperbolic if all the eigenvalues of $A$ possess non-zero real parts, i.e., $n_C = 0$. The relationship between the invariant manifolds and the stable and unstable subspaces of the system is then expressed using the Stable Manifold Theorem [32] as,

**Theorem 3.7.1 (Stable Manifold Theorem)** *Suppose $\dot{\bar{x}} = \bar{f}(\bar{x})$ possesses a hyperbolic equilibrium point $\bar{x}_{eq}$. Then, there exist local stable and unstable manifolds $W^S_{loc}(\bar{x}_{eq})$, $W^U_{loc}(\bar{x}_{eq})$ of the same dimension $n_S$, $n_U$ as that of the eigenspaces $E^S$ and $E^U$ of the linearized system in Equation (3.13),* and *tangent to $E^S$ and $E^U$ at $\bar{x}_{eq}$.*

Theorem 3.7.1 allows the stable and unstable subspaces to serve as linear approximations for the stable and unstable manifolds, respectively. To demonstrate the relationship between manifolds and subspaces, consider the $L_2$ libration point in the Earth-Moon system. The stable and unstable manifolds $W^S_{loc}$ and $W^U_{loc}$ corresponding to $L_2$ are depicted in Figure 3.9, in blue and magenta, respectively. The stable and unstable subspaces $E^S$ and $E^U$ are represented as lines along the stable and unstable eigenvectors, $\bar{v}_S$ and $\bar{v}_U$, since by definition, these are structures in the linear system. The $\pm$ sign indicates the direction of the eigenvector along which the positive and negative half-manifold branches are constructed. Conforming to the Stable Manifold Theorem, the manifold structures are tangent to their corresponding subspaces at the equilibrium point. The local invariant manifolds $W^S_{loc}$ and $W^U_{loc}$ also possess global analogs, $W^S$ and $W^U$, that extend further from the vicinity of the equilibrium solutions. The global stable manifold is generated by propagating flow backwards in time along $W^S_{loc}$, and the global unstable manifold by propagating flow forwards in time along $W^U_{loc}$.

Assuming that $\bar{x}_{eq}$ is a non-hyperbolic equilibrium point, i.e., $n_S$, $n_U$, and $n_C$ are all non-zero, the structure of the local flow is characterized by the Center Manifold Theorem [32] as,

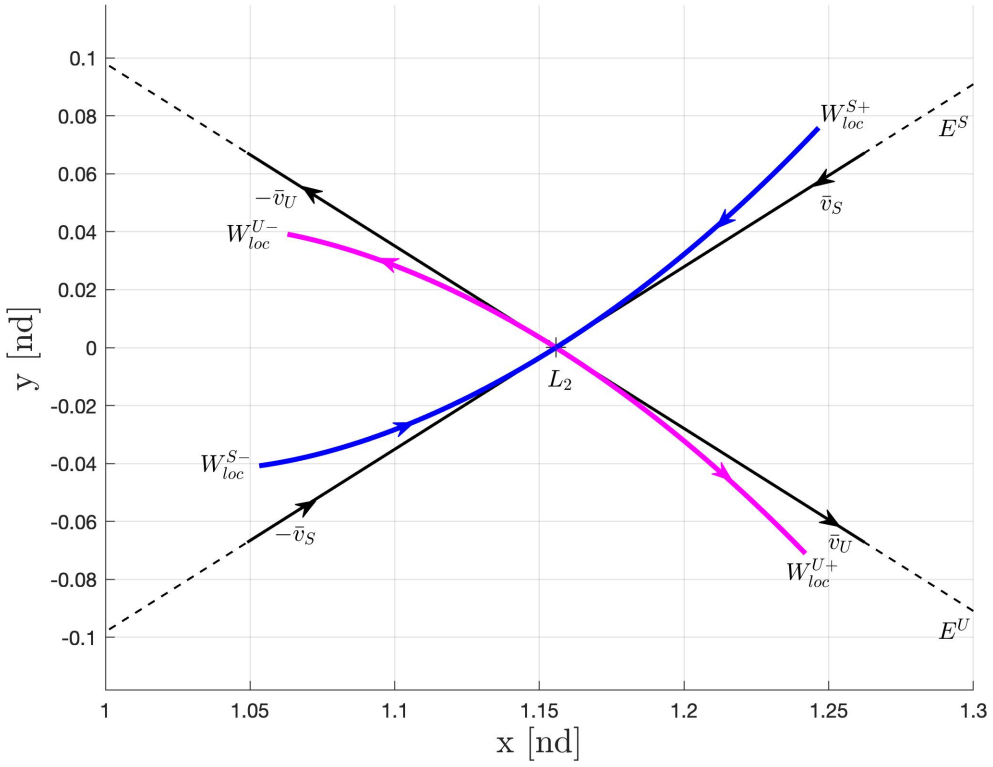


Figure 3.9. Stable and Unstable Local Manifolds for $L_2$ in the Earth-Moon System.

**Theorem 3.7.2 (Center Manifold Theorem)** *Let $\bar{f}$ be a vector field on $\mathbb{R}^n$ vanishing at the origin $\left(\bar{f}(\bar{x}_{eq}) = \bar{0}\right)$ and $A = F\bar{f}(\bar{x}_{eq})$. The spectrum of $A$ is divided into $n_S$, $n_U$, and $n_C$ with*

$$\begin{aligned} \Re[\lambda_j] < 0 &\rightarrow \lambda_j \in n_S \\ \Re[\lambda_j] = 0 &\rightarrow \lambda_j \in n_C \\ \Re[\lambda_j] > 0 &\rightarrow \lambda_j \in n_U \end{aligned} \tag{3.17}$$

*Let the generalized eigenspaces be $E^S$, $E^C$, and $E^U$, respectively. Then, there exist stable and unstable manifolds $W^S$ and $W^U$ tangent to $E^S$ and $E^U$ at $\bar{x}_{eq}$, and a center manifold $W^C$ tangent to $E^C$ at $\bar{x}_{eq}$. The manifolds $W^S$, $W^U$, and $W^C$ are all invariant for the flow $\bar{f}$. The stable and unstable manifolds are unique, but the center manifold need not be.*

The existence of center manifolds implies that the structure of the flow near $\bar{x}_{eq}$, possessing at least some zero eigenvalues, is more diverse than an equilibrium point with no center subspace. Some examples of the types of motion that might exist in the center subspace near the equilibrium point include periodic orbits and quasi-periodic trajectories. Specifically, the in-plane Lyapunov orbits and nearly vertical out-of-plane orbits exist in $W^C$ near $L_i$.

### 3.7.2 Manifolds of Periodic Orbits

Similar to the computation of manifolds for equilibrium points, manifolds for points along periodic orbits are also produced. Recall that the stability of periodic orbits is determined from the eigenvalues of the monodromy matrix for the orbit. The eigenvalues are categorized as stable, unstable, or marginally stable depending on their individual values. Extending that analysis, the number of eigenvalues corresponding to each of the three subspaces are defined,

$$\begin{aligned} |\lambda_j| < 1 &\rightarrow \lambda_j \in n_S \\ |\lambda_j| = 1 &\rightarrow \lambda_j \in n_C \\ |\lambda_j| > 1 &\rightarrow \lambda_j \in n_U \end{aligned} \tag{3.18}$$

where $n_S$, $n_C$, and $n_U$ correspond to the dimensions of the stable, center, and unstable subspaces. For a periodic orbit represented as $\Gamma$ and its evolving state vector $\bar{x}$, there exist local stable, center, and unstable manifolds, $W^S_{loc}(\Gamma)$, $W^C_{loc}(\Gamma)$, and $W^U_{loc}(\Gamma)$, respectively, that are tangent to the stable, center, and unstable eigenspaces, $E^S(\Gamma)$, $E^C(\Gamma)$, and $E^U(\Gamma)$. These manifolds also possess global analogs, represented by $W^S(\Gamma)$, $W^C(\Gamma)$, and $W^U(\Gamma)$. Consistent with the Stable Manifold Theorem for Periodic Orbits, the stable manifold associated with the periodic orbit possesses a dimension equal to $n_S + 1$; the unstable manifold possesses a dimension equal to $n_U + 1$. Thus, the dimensions of the periodic orbit manifolds are greater than the dimension of their corresponding eigenspaces by one. Finally, the rate of arrival and

departure along the stable and unstable manifolds, respectively, for a periodic orbit is determined by the size of the stability index evaluated for the orbit [33].

### 3.7.3 Computation of Manifolds for Resonant Orbits

Invariant manifolds corresponding to an unstable periodic orbit are computed by discretizing the orbit into a specified number of *fixed points*, represented by $\bar{x}^*$. Recall from Section 3.4, that the eigenvalues of the monodromy matrix as computed at any fixed point along a periodic orbit, remain precisely the same along the orbit. The eigenvectors, however, corresponding to each point on the orbit reflect the natural flow near a specific fixed point and, thus, vary along the orbit. Therefore, the eigenvectors are determined along each fixed point to accurately determine the manifolds. The components of each eigenvector are decomposed as,

$$\bar{v}_S = [x_S \; y_S \; z_S \; \dot{x}_S \; \dot{y}_S \; \dot{z}_S]^T \tag{3.19}$$

$$\bar{v}_U = [x_U \; y_U \; z_U \; \dot{x}_U \; \dot{y}_U \; \dot{z}_U]^T \tag{3.20}$$

Next, the tangency of the eigenspaces to the invariant manifolds is exploited in the construction of the stable and unstable manifolds associated with a specific fixed point. The local stable manifold $W^U_{loc}$ is tangent to the stable subspace $E^S$, while the local unstable manifold $W^U_{loc}$ is tangent to the unstable subspace $E^U$ at the location of the fixed point. The stable and unstable eigenspaces themselves lie along the stable and unstable eigenvectors of the monodromy matrix, respectively. An important component in the approximation to the nonlinear flow is the direction along the eigenvector. The eigenvectors are normalized in terms of three position components, three velocity components, or the full six element state. Normalization along the position components allows the physical characterization of the states, and is the

strategy for normalization implemented for this investigation. Then, the normalized states of the stable and unstable eigenvectors are evaluated as,

$$\bar{v}^{W_S} = \frac{\bar{v}_S}{[x_S^2 + y_S^2 + z_S^2]^{\frac{1}{2}}} \tag{3.21}$$

$$\bar{v}^{W_U} = \frac{\bar{v}_U}{[x_U^2 + y_U^2 + z_U^2]^{\frac{1}{2}}} \tag{3.22}$$

A point on a half-manifold is located by stepping off the fixed point along the direction of the stable and unstable eigenvectors. The positive half branch of the stable manifold, $W_{loc}^{S+}$, departs the fixed point along the positive direction of the stable eigenvector, $\bar{v}_S$, while the negative half branch, $W_{loc}^{S-}$, departs along the negative direction of the stable eigenvector, $-\bar{v}_S$. Similarly, the positive half branch of the unstable manifold, $W_{loc}^{U+}$, departs along the positive direction of the unstable eigenvector, $\bar{v}_U$, while the negative half branch, $W_{loc}^{U-}$, departs along the negative direction of the unstable eigenvector, $-\bar{v}_U$. A nondimensional perturbation, denoted by $d$, is introduced relative to the fixed point in the direction of the eigenvectors. The selection for the value of $d$ is imperative: if the value of $d$ is too large, the resulting point might not lie on the manifold itself; if the value is too small, the trajectory remains in the vicinity of the fixed point for a longer interval, leading to little progress along the manifold path and the accumulation of integration error. Once an appropriate value of $d$ is selected, the point on the local half-manifold is evaluated as,

$$\bar{x}_{S_\pm} = \bar{x}^* \pm d \cdot \bar{v}^{W_S} \tag{3.23}$$

$$\bar{x}_{U_\pm} = \bar{x}^* \pm d \cdot \bar{v}^{W_U} \tag{3.24}$$

where $\pm$ corresponds to the positive and negative directions along each manifold. This process is repeated for each fixed point along the periodic orbit to produce the stable and unstable manifolds corresponding to the orbit.

The computation of periodic orbit manifolds is illustrated within the context of the 3:4 resonant orbit in the Earth-Moon system represented in Figure 3.3. The orbit is discretized into 100 fixed points spaced evenly in time, and a step-off distance of $d = 40$ km is selected [15]. The initial states corresponding to the stable and unstable half-manifolds are propagated for $\tau = 100$ [nd], i.e., approximately four times the period of the resonant orbit. Figure 3.10 illustrates the global stable manifolds plotted in blue and the global unstable manifolds plotted in magenta. The projections of the manifolds initially appear to shadow the resonant orbit, but become tangled and chaotic as the propagation time increases. Thus, this approach for visualizing manifolds is not informative towards trajectory design, and other schemes of analyzing flow characteristics must be explored.

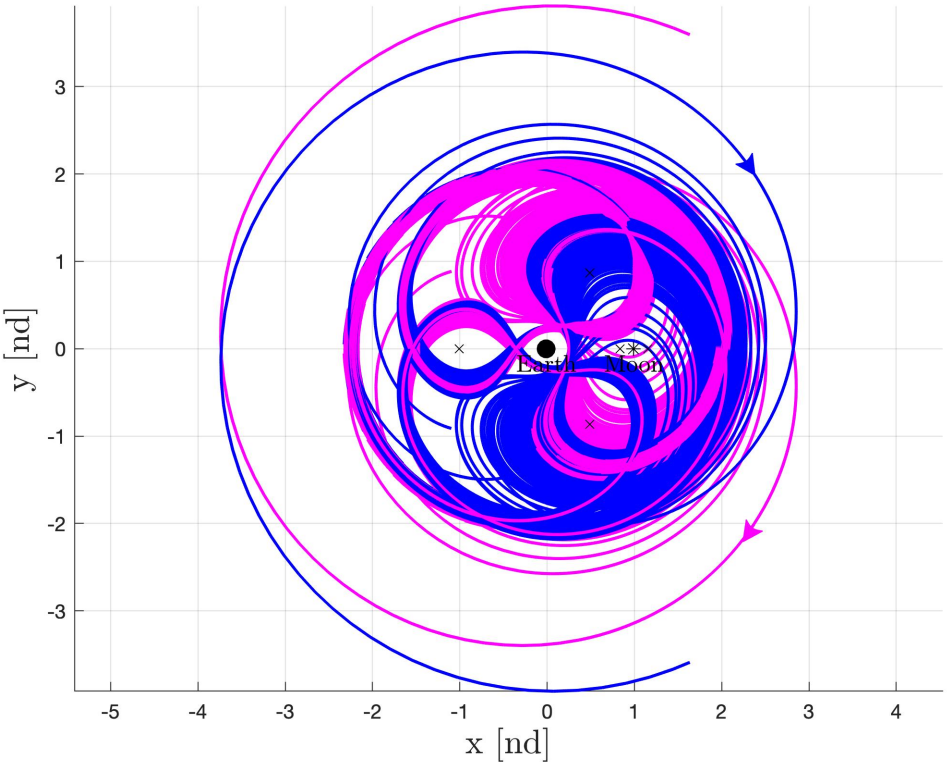


Figure 3.10. Stable and Unstable Global Manifolds for the 3:4 Resonant Orbit in the Earth-Moon System.

## 3.8 Poincaré Maps

There exist two main representations of dynamical systems for analysis: systems of differential equations of the form $\dot{\bar{x}} = \bar{f}(\bar{x}, t)$, or mappings of the form $\bar{x}_{n+1} = \bar{f}(\bar{x}_n)$. The latter describes the time evolution of a vector $\bar{x}$ at discrete time intervals $t$ (integer). Both representations are deterministic systems, and their similarities allow the use of maps for the illustration of properties for generic dynamical systems that are described by differential equations. Specifically, the utilization of maps to understand chaos has been extensively explored in the last few decades.

Systems of differential equations are represented as maps on a *Poincaré surface of section*, a concept first utilized by Henri Poincaré in his analysis of the CR3BP [34]. This type of formulation allows a continuous time system (flow) to be reduced to the examination of an associated discrete time system (map). The advantages of this technique include:

- **Reduction of Dimension**: The construction of a Poincaré map eliminates at least one variable in the problem, reducing the study to a lower dimensional system.

- **Understanding of Global Dynamics**: In a lower dimensional study, Poincaré maps provide insight into the global dynamics of a system, often highlighting trends that might not be apparent otherwise.

- **Conceptual Clarity**: Concepts that otherwise might be too complex to state for ordinary differential equations can be concisely stated for the corresponding Poincaré map.

Unfortunately, there currently exist no general methods for the construction of a Poincaré map associated with a set of differential equations, since some knowledge of the geometrical structure of the phase space is necessary. The process of construction of a Poincaré map requires technical insight into the specific problem. Within the context of the CR3BP, however, three special cases of interest arise frequently: orbit

structure near a periodic orbit, periodically forced oscillators, or orbit structure near a homoclinic or heteroclinic orbit. The relevant application in this investigation is the orbit structure near a periodic orbit, which is explored in detail via maps [25].

Consider an autonomous system defined in an $m$-dimensional phase space ($\mathbb{R}^m$). A vector field $\bar{f}$ generates a flow $\bar{x}(\bar{x}_0, t) = \bar{K}(\bar{x}, t)$, or $\varphi_t(\bar{x}_0)$. The mapping $\bar{K}(\bar{x}, t)$ defines a solution curve, orbit, or trajectory corresponding to the differential equation based at $\bar{x}_0$. In that phase space, an $(m-1)$ dimensional hyperplane $\Sigma$ is defined such that the flow is transversal to $\Sigma$, that is, the trajectory possesses some component normal to the plane. The hyperplane $\Sigma$ is defined after specific time intervals, or after specific geometries. Consider a periodic orbit $\Gamma$, and let $\bar{x}^*$ be a fixed point along the orbit. The hyperplane $\Sigma$ is transversal to $\Gamma$ at $\bar{x}^*$. A trajectory through $\bar{x}^*$ crosses $\Sigma$ at $\bar{x}^*$ in time $T$, where $T$ is the period of the orbit. Since the flow $\varphi_t$ is continuous with respect to the initial conditions, trajectories that originate on $\Sigma$ in a sufficiently small neighborhood of $\bar{x}^*$ will intersect $\Sigma$ in the vicinity of $\bar{x}^*$ in approximately the time $T$. Thus, $\varphi_t$ and $\Sigma$ define a mapping $P$ in some neighborhood of $\bar{x}^*$ ($U \subset \Sigma$) onto another neighborhood of $\mathbf{x}^*$ ($V \subset \Sigma$). Then, $P$ is the Poincaré map for the autonomous system, represented as,

$$P(\bar{x}_0) = \bar{x}(\bar{x}_0) \tag{3.25}$$

where $\bar{x}$ is the state vector that results from the application of the nonlinear map to $\bar{x}_0 \in \Sigma$.

Poincaré maps are particularly useful towards understanding the stability of periodic solutions in the CR3BP. The stability properties of a fixed point on a Poincaré map are closely associated with the stability of the associated periodic orbit. For a fixed point $\bar{x}^*$ on a hyperplane $\Sigma$, consider an initial state $\bar{x}_0$ in the vicinity of the fixed point. The initial state is propagated numerically, and its intersections with the hyperplane are recorded as $P_1(\bar{x}_0)$, $P_2(\bar{x}_0)$, and so on, until the last return $P_n(\bar{x}_0)$. If subsequent returns to the map approach the fixed point $\bar{x}^*$ on the hyperplane, the

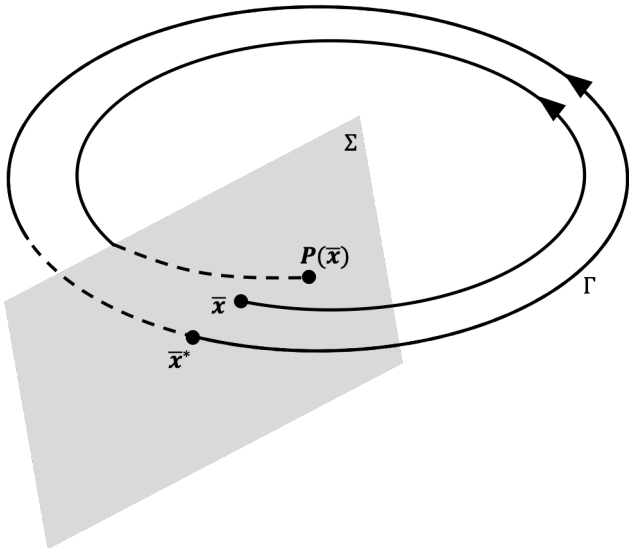


Figure 3.11. Poincaré Map of an Autonomous Section.

orbit is considered stable. If the returns appear to diverge from the fixed point, the periodic orbit is unstable. If the returns to the map are disordered, the orbit is considered to be chaotic. The first case corresponds to stable manifolds associated with the fixed point and is illustrated in Figure 3.12(a). The second case corresponds to unstable manifolds and is illustrated in Figure 3.12(b). The final scenario, e.g., in the case of center manifolds of the fixed point, is illustrated in Figure 3.12(c). Therefore, the manifolds for a fixed point are not trajectories, rather returns to the hyperplane $\Sigma$ resulting from perturbations.

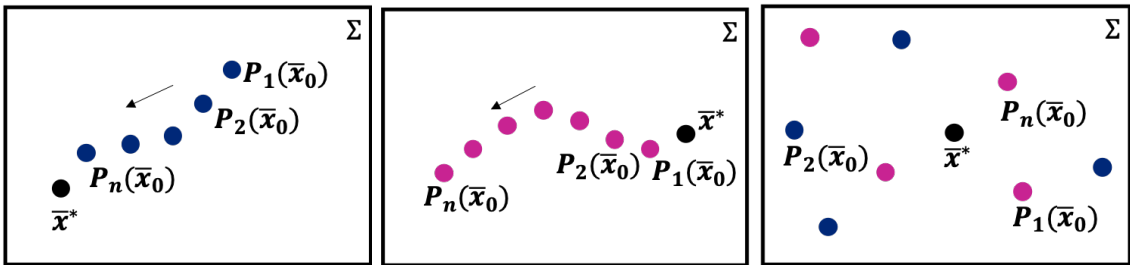


(a) Stable (b) Unstable (c) Chaos

Figure 3.12. Poincaré Map Returns for Stable, Unstable, and Chaotic Cases.

Recall the invariant manifolds for the 3:4 resonant orbit illustrated in Figure 3.10. In configuration space, the manifolds appear tangled and do not offer insight into the global dynamics near the orbit. Other methods of visualization, such as Poincaré maps, reflect trends in stability and the nearby dynamics that are not apparent otherwise. For the planar resonant orbit in consideration in $\mathbb{R}^4$, a geometric hyperplane $\Sigma$ is defined by fixing one of the four coordinates, reducing the problem to a surface in $\mathbb{R}^3$. In this case, $\Sigma$ is defined to be $y = 0$. The local stable and unstable manifolds computed from fixed points along the resonant orbit are then propagated numerically, and the intersections with the hyperplane of the global stable and unstable manifolds are recorded. The values of $x$ and $\dot{x}$ at each intersection are used to plot the returns to the map, but other variables may also be employed. Figure 3.13 illustrates the Poincaré map, with the zoomed in views of different regions on the map represented in Figure 3.14. Each point on the map corresponds to a subsequent return. The blue points are associated to returns of the stable manifolds, while the magenta ones correspond to returns of unstable manifolds. The black marker indicates the initial state of the 3:4 resonant orbit on the $x$-axis. From the plot, it is immediately apparent that the returns of the manifolds are more clearly identified than their projections in configuration space. Some of the regions of interest on the map include locations where the stable and unstable manifolds intersect, which correspond to homoclinic connections. Maps are now frequently employed in the computation of low-cost and even natural transfers between orbits representing different resonances in the CR3BP. Such maps and methodologies are leveraged extensively in the computation of inexpensive transfers and the determination of relevant dynamical tools for trajectory design in the CR3BP.

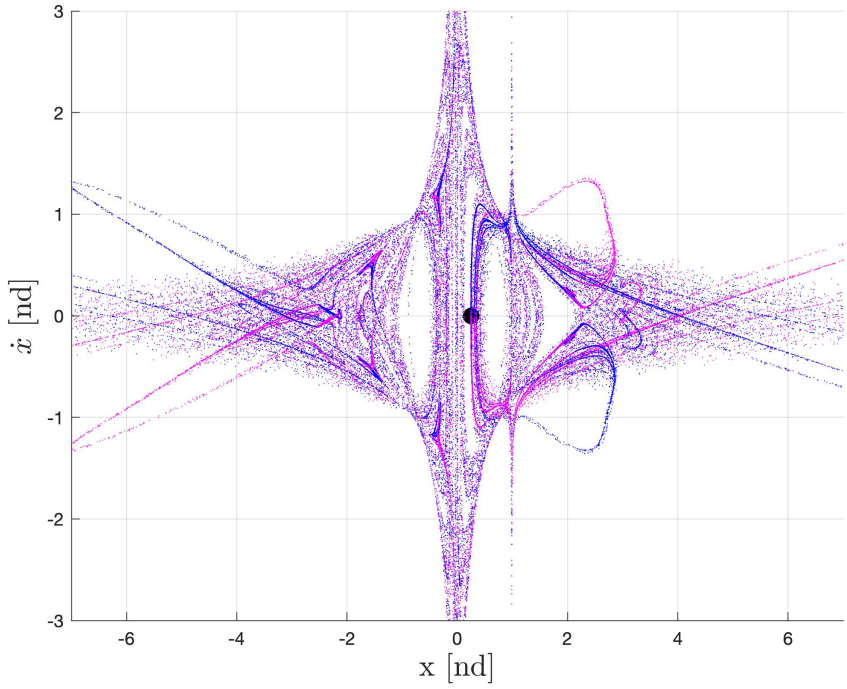


Figure 3.13. Poincaré Map for Stable and Unstable Manifold Returns of the 3:4 Resonant Orbit in the Earth-Moon System.

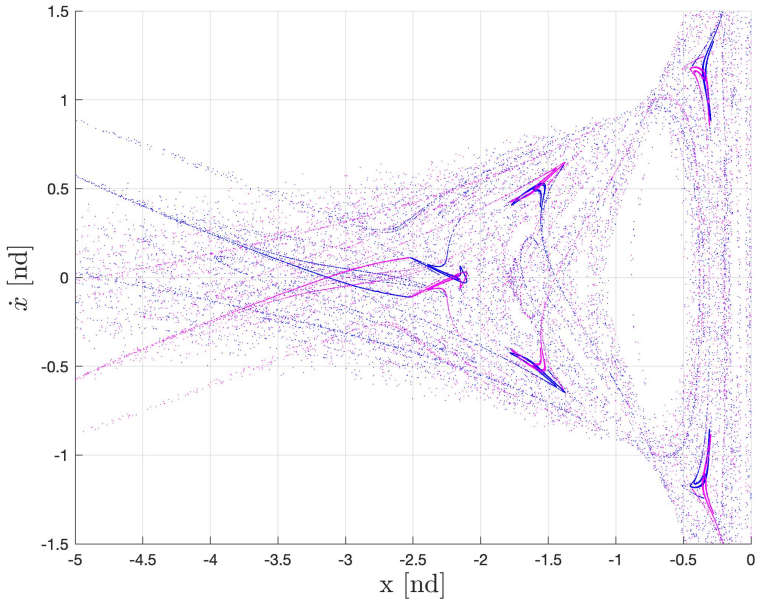


(a) $x < 0$

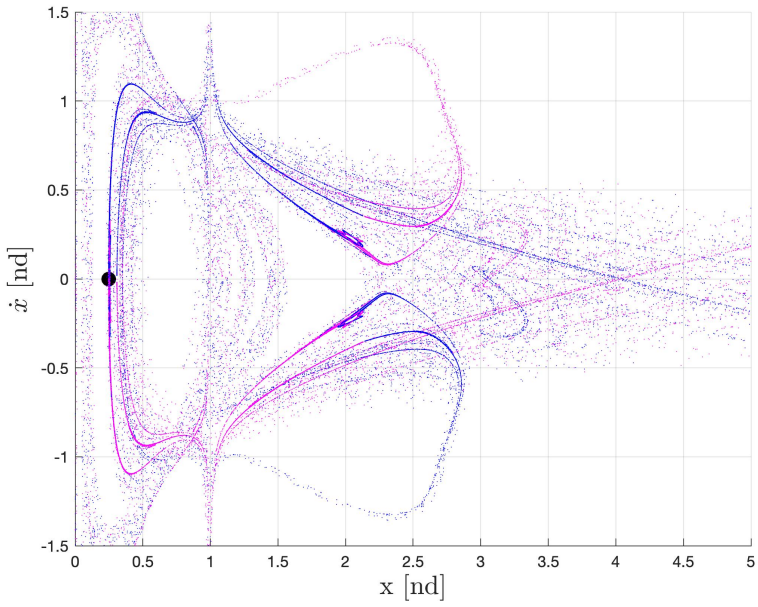


(b) $x > 0$

Figure 3.14. Zoomed in Views of the Poincaré Map for the 3:4 Resonant Orbit in the Earth-Moon System.

# 4. RESONANT ORBITS FOR TRAJECTORY DESIGN

The focus of this investigation is a strategy to leverage resonant orbits for transfer trajectory design utilizing the dynamical systems techniques. The properties associated with the planet-moon systems for this investigation are introduced as well as the concept of the theoretical minimum transfer cost. Most resonant trajectories offer expansive coverage of configuration space in a CR3BP system, and that characteristic is exploited in the design of transfers between various periodic orbits. Scenarios in which resonant orbits are employed as intermediaries are demonstrated. Techniques to apply unstable resonant orbits and their manifolds to the computation of natural planar transfers follow, aided by Poincaré mapping. Finally, homoclinic connections linking resonant orbits and other periodic orbits are detailed, along with the computation of homoclinic-type resonant orbit chains.

## 4.1 Relevant Physical Parameters and CR3BP Quantities

The CR3BP systems of interest in this investigation are the following planet-moon combinations: Earth-Moon, Saturn-Titan, and Mars-Deimos. It is, therefore, useful to summarize the physical parameters and the CR3BP quantities associated with these systems. The gravitational parameter, $GM$, corresponding to each planet and moon, along with their mean radii, are listed in Table 4.1. The CR3BP characteristic quantities, i.e., the $\mu$, $l^*$, and the $t^*$ values associated with these systems, are also included in Table 4.2. Recall that these quantities are evaluated employing Equations (2.7)-(2.12). Also recall that Table 2.1 lists the values for the Jacobi constant corresponding to the libration points in these systems.

Table 4.1. Physical Parameters for Relevant Bodies.

| **Planet** | **GM** $[km^3/s^2]$ | **Radius** $[km]$ |
|---|---|---|
| Earth | 398600.448 | 6478.137 |
| Moon | 4902.799 | 1737.400 |
| Saturn | 37931284.499 | 58300.000 |
| Titan | 8978.138 | 2574.799 |
| Mars | 42828.374 | 3389.527 |
| Deimos | 0.0000962 | 6.299 |

Table 4.2. CR3BP Quantities Corresponding to Relevant Systems.

| **System** | $\mu$ | $l^*$ $[km]$ | $t^*$ $[s]$ |
|---|---|---|---|
| Earth-Moon | $1.21506 \times 10^{-2}$ | 384388.174 | 375172.943 |
| Saturn-Titan | $2.36639 \times 10^{-4}$ | 1221865.000 | 219272.755 |
| Mars-Deimos | $2.24514 \times 10^{-9}$ | 23457.075 | 17359.811 |

## 4.2 Theoretical Minimum $\Delta$V

An essential consideration in the design of trajectories with multiple segments is the change in the value of the Jacobi constant as the spacecraft propagates along a path. Impulsive maneuvers along the trajectory are employed to achieve such a change in the Jacobi constant value. The maneuvers are quantified as the magnitude of $\Delta V$, that is, equal to the change in velocity required by the spacecraft to achieve the required change in energy and direction. Evaluating the theoretical minimum $\Delta V$ assesses the corresponding maneuver to accommodate only the energy change; such a reference number allows the comparison of the efficacy of the actual maneuver against a benchmark [16], [35].

Consider a spacecraft moving along a trajectory segment with a Jacobi constant value of $C_1$, and let the Jacobi constant of the next arc in the trajectory sequence

be $C_2$. Assuming the two arcs intersect in configuration space, the corresponding values of the pseudo-potential at the intersection point are equal, and this value is represented by $U^*$. Let $\bar{v}_1$ and $\bar{v}_2$ denote the velocities at the point of intersection of the arcs, with $\alpha$ representing the angle between the velocity vectors. Then, rewriting Equation (2.40) yields,

$$C_1 = 2U^* - v_1^2 \tag{4.1}$$

$$C_2 = 2U^* - v_2^2 \tag{4.2}$$

where $v_1$ and $v_2$ are the magnitudes of the velocity vectors corresponding to each segment at the time of intersection. Representing the difference in the Jacobi constant value as $\Delta C = C_1 - C_2$, Equations (4.1) and (4.2) are reduced to,

$$\Delta C = v_2^2 - v_1^2 \tag{4.3}$$

The change in velocity between the two arcs, $\Delta V$, is then computed as,

$$\Delta V = \sqrt{v_1^2 + v_2^2 - 2v_1 v_2 cos\alpha} \tag{4.4}$$

Clearly, the value of $\Delta V$ as computed in Equation (4.4) is a minimum when the value of $cos\alpha$ is equal to one, i.e., when the velocity vectors are parallel. Consequently, the minimum $\Delta V$ is represented as,

$$\Delta V_{min} = \sqrt{v_1^2 + v_2^2 - 2v_1 v_2} \tag{4.5}$$

Rewriting Equation (4.5) in terms of the change in Jacobi constant value, $\Delta C$, yields the expression for the theoretical minimum $\Delta V$, that is, the cost to accommodate the energy difference,

$$\Delta V_{min} = \sqrt{2v_1^2 + \Delta C - 2v_1\sqrt{\Delta C + v_1^2}} \tag{4.6}$$

Equation (4.6) suggests that tangential maneuvers correspond to the lowest values of $\Delta V$. This conclusion aids in the selection of trajectory segments that result in lower maneuver costs.

## 4.3 Transfers Incorporating Resonant Arcs

The versatility of resonant orbits is apparent in their coverage, both planar and spatial, in various CR3BP systems. This property is leveraged in designing low-cost transfers between other periodic orbits. Specifically, in the cases where periodic orbit manifolds cannot be employed due to orbital stability considerations, incorporating sections along resonant orbits as transfer arcs is favorable [16], [15].

To understand the methodology behind designing periodic orbit transfers utilizing resonant orbit arcs, consider a planar transfer between an $L_3$ Lyapunov orbit and a Distant Retrograde Orbit (DRO) in the Earth-Moon system [36]. The DROs are planar, stable orbits that surround the smaller primary [22]. Let an $L_3$ Lyapunov orbit be the departure orbit with arrival into the DRO. The initial conditions, the period, and the Jacobi constant value corresponding to the two orbits are summarized in Table 4.3. Figure 4.1 illustrates the orbits plotted as in the CR3BP rotating frame, where the $L_3$ orbit is plotted in blue, and the DRO is represented in red.

Table 4.3. Initial Conditions and Jacobi Constant Values for the Departure and Arrival Orbits.

| **Orbit** | $\boldsymbol{x}$ **[nd]** | $\boldsymbol{\dot{y}}$ **[nd]** | $\boldsymbol{C}$ | **Period [nd]** |
|---|---|---|---|---|
| $L_3$ Lyapunov | $-1.3868$ | 0.7209 | 2.8510 | 6.2240 |
| DRO | 0.6731 | 0.7500 | 2.8510 | 5.1283 |

An appropriate resonant orbit for incorporation as a transfer arc is determined as the first step in the transfer design process. Note that the $L_3$ Lyapunov orbit and the DRO, both, cross the $\hat{x}$-axis perpendicularly. Given that resonant orbits also possess perpendicular $\hat{x}$-axis crossings, the locations of the crossings are analyzed

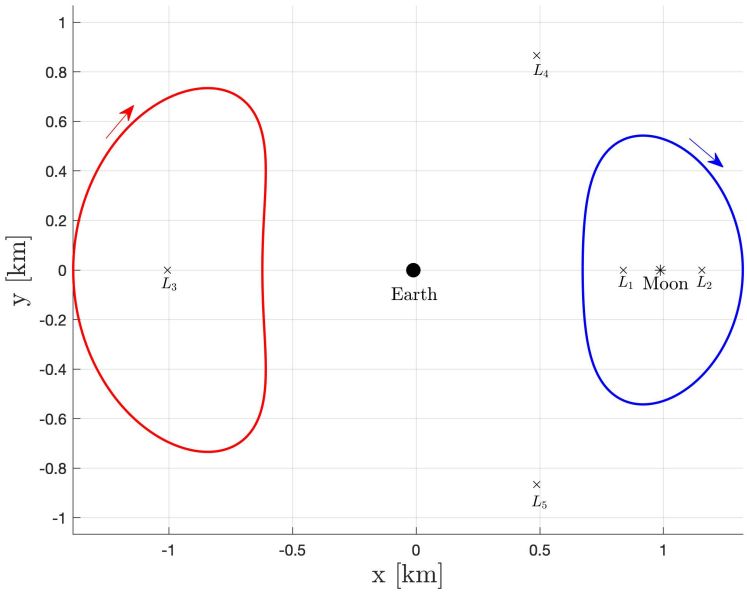


Figure 4.1. The $L_3$ Lyapunov and DRO for Departure and Arrival in the Earth-Moon System.

to locate intersections with the departure and arrival orbits in configuration space. Noting the perpendicular crossings limits the search for intersections to tangential intersections only; tangential intersections are known to be favorable for low-cost maneuvers. Figure 4.2 illustrates the perpendicular crossings for resonant orbits that intersect the $\hat{x}$-axis at the same location as the DRO, with the Jacobi constant values corresponding to each orbit plotted on the $\hat{y}$-axis. It is evident from the plot that orbits from the 3:4, 2:3, 3:5, and 1:2 planar resonant families are potential candidates for intermediate arcs, with the 3:4 resonance requiring the least, and the 1:2 orbit requiring the most change in energy. Although any of the four orbits are employable, the 2:3 resonant orbit offers a convenient, near-tangential intersection with the $L_3$ Lyapunov orbit as well, allowing the orbit to provide both the departure and arrival legs along the transfer. Therefore, the 2:3 resonant orbit is selected to construct an intermediate transfer arc from the departure to the arrival orbits. The initial conditions, the Jacobi constant value, and the period of the selected 2:3 resonant

orbit are listed in Table 4.4. Figure 4.3 represents the 2:3 resonant orbit, plotted in black, with the departure and arrival orbits illustrated as dashed grey curves.

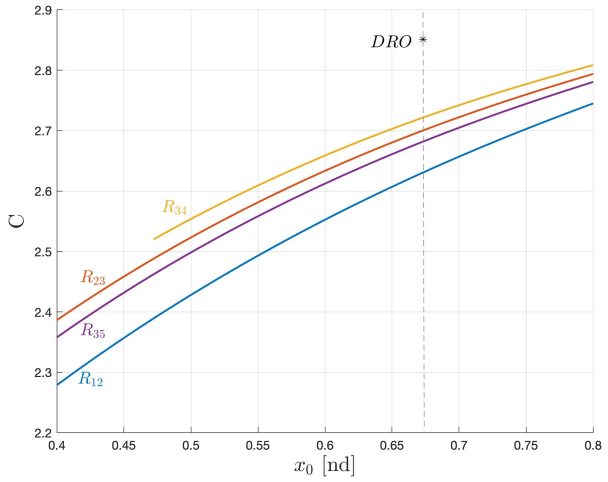


Figure 4.2. Resonant Orbit Perpendicular Crossings for Intermediate Arc Selection.

Table 4.4. Initial Conditions and Jacobi Constant Value for the Selected 2:3 Resonant Orbit in the Earth-Moon System.

| $x$ $[nd]$ | $\dot{y}$ $[nd]$ | $C$ | Period $[nd]$ |
|---|---|---|---|
| 0.6729 | 0.8450 | 2.7001 | 18.1759 |

To depart the $L_3$ orbit on a segment of the resonant 2:3 orbit, a departure maneuver of magnitude $\Delta V_D$ is applied. Similarly, to arrive at the DRO on the 2:3 resonant arc, an arrival maneuver of magnitude $\Delta V_A$ is necessary. Note that, in spite of the near-tangential intersections, the departure and arrival maneuvers are not zero, due to the difference in the Jacobi constant values of the three orbits. Additionally, since the intersection of the transfer arc with the $L_3$ orbit is not perfectly tangential, involving a directional change of the velocity vector of approximately 5°, the departure maneuver is significant as well. The computed values of $\Delta V_D$ and $\Delta V_A$, along with the theoretical $\Delta V_{min}$ at the maneuver locations, are included in Table 4.5. As expected, at arrival, the $\Delta V_A$ is equal to the value of $\Delta V_{min}$ owing to the tangential

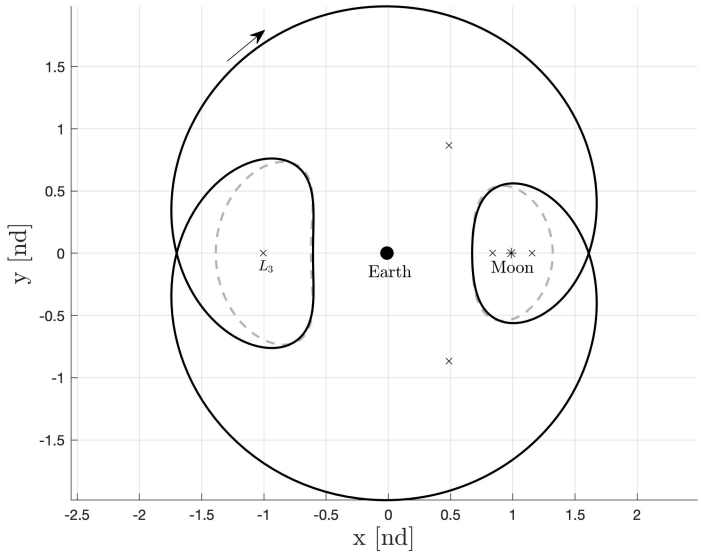


Figure 4.3. 2:3 Resonant Orbit as an Intermediate Transfer Arc in the Earth-Moon System.

intersection. The values of $\Delta V_D$ and the $\Delta V_{min}$ at the departure location, however, do differ significantly. The time of flight for the transfer is 37.344 *days*, and the total $\Delta V$ is 0.2243 $km/s$. Figure 4.4 illustrates the complete transfer sequence, with the departure and arrival orbits plotted in black, and the transfer arc represented in purple. Solid purple points indicate the locations of the departure and arrival maneuvers. Note that the transfer is an exterior transfer, since it propagates through the exterior region of the Earth-Moon system. Also, this feasible transfer is not optimized.

Table 4.5. Departure and Arrival Maneuver Magnitudes for Transfer using a 2:3 Resonant Orbit Arc in the Earth-Moon System.

| | $\boldsymbol{\Delta V_D}$ $\boldsymbol{[km/s]}$ | $\boldsymbol{\Delta V_A}$ $\boldsymbol{[km/s]}$ |
|---|---|---|
| **Actual** | 0.1274 | 0.0969 |
| **Theoretical Minimum** | 0.1141 | 0.0969 |

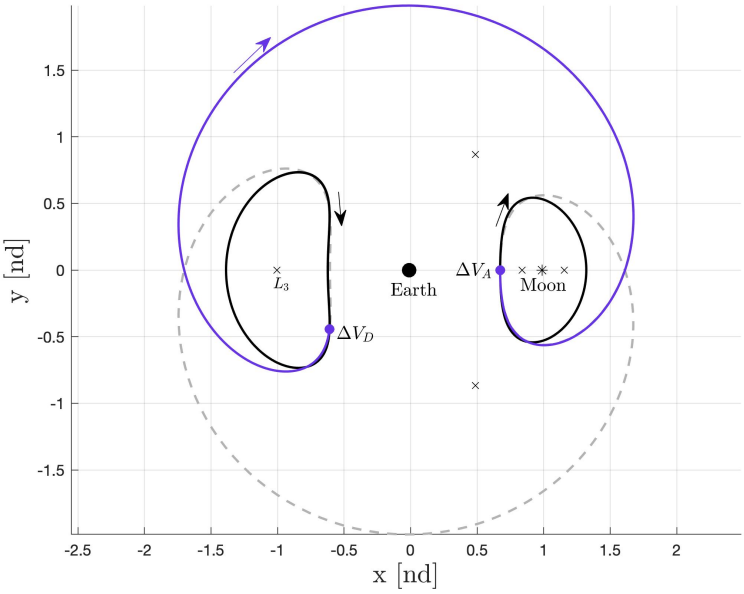


Figure 4.4. Transfer between $L_3$ Lyapunov Orbit and DRO employing a 2:3 Resonant Orbit Arc in the Earth-Moon System.

### 4.3.1 Tour of the Mars-Deimos System

Another application of resonant orbits is in the design of system tours [15], [37]. Such tours are characterized by close approaches to the primaries, shorter periods, and generally stable orbits [38], [39]. These criteria are favorable for flybys and orbiter-based mission scenarios, and allow for lower maintenance orbits that are not sensitive to orbital perturbations. For demonstration, consider resonances in the Mars-Deimos system. Families of resonant orbits computed in the Earth-Moon system are also computed in the Mars-Deimos system. A consequence of the low $\mu$ value of the system is that most resonant orbits are highly stable. The process of incorporating resonant orbits as intermediate transfer arcs is extended to the design of stable tours of the Martian system.

Resonant orbits that facilitate the tour of the system are selected on the basis of their orbital stability and passage through the system. For instance, stable orbits that provide both, circumlunar and cislunar passages, are candidates for a tour trajectory.

To construct a tour, consider a 3:2 resonant orbit and a 2:1 resonant orbit in the Mars-Deimos system. The initial conditions, the Jacobi constant value, and the period corresponding to these orbits are summarized in Table 4.6. Note that, in spite of a tangential intersection between the two orbits in configuration space, a maneuver is necessary to obtain a continuous trajectory due to the difference in their Jacobi constants. The magnitude of the maneuver is computed as $\Delta V = 266.95\ m/s$, which is approximately equal to the theoretical minimum value of $266.92\ m/s$. The resulting trajectory that meets the system tour design criteria is illustrated in Figure 4.5, with the maneuver necessary to shift to the 2:1 resonant orbit from the 3:2 resonant orbit as indicated by a solid purple point. The total time of flight for the trajectory is 3.787 *days*; the cislunar passages requires 1.262 *days*. The trajectory allows for a Deimos flyby at a relative radius of 610.40 $km$ at a velocity of 0.5741 $km/s$.

Table 4.6. Initial Conditions and Jacobi Constant Values for the 3:1 and 2:1 Resonant Orbits.

| **Resonance** | $\boldsymbol{x}$ $[\boldsymbol{nd}]$ | $\boldsymbol{\dot{y}}$ $[\boldsymbol{nd}]$ | $\boldsymbol{C}$ | **Period** $[\boldsymbol{nd}]$ |
|---|---|---|---|---|
| 3:2 | 0.4999 | 1.1402 | 2.9503 | 12.5664 |
| 2:1 | −1.0262 | 0.4249 | 2.8215 | 6.2832 |

## 4.4 Transfers Utilizing Resonant Orbit Manifolds

Incorporating invariant manifolds into transfers can substantially reduce transfer costs, potentially allowing for natural, cost-free transfers [4], [40]. Since the focus of this study is resonant orbits, invariant manifolds associated with unstable resonant orbits are investigated for use as intermediate arcs to create transfers from resonant orbits to other periodic orbits. In particular, resonances in the Saturn-Titan system are examined, and Poincaré sections are employed to produce useful transfer arcs [41]. Consider the unstable 5:6 resonant orbit in the Saturn-Titan system, as illustrated in Figure 4.6. The nondimensional initial conditions, the Jacobi constant value, and

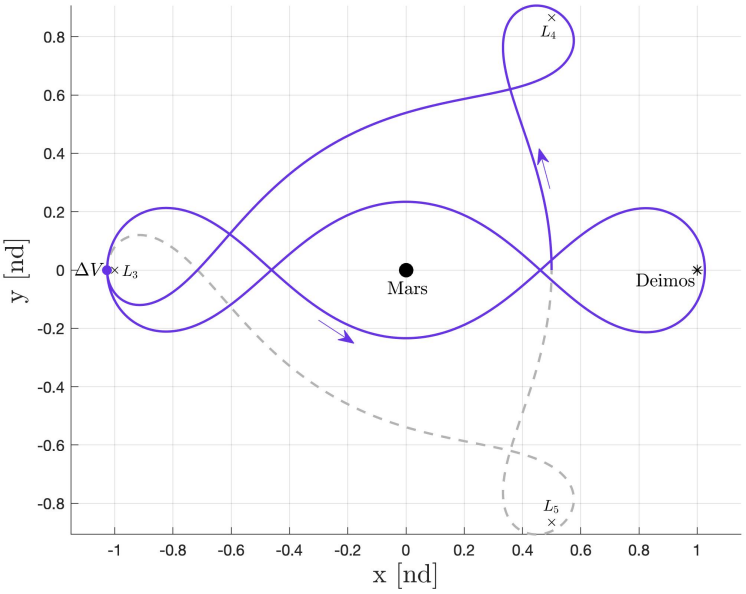


Figure 4.5. 3:2 and 2:1 Resonant Tour Trajectory in the Mars-Deimos System.

the period of the orbit are listed in Table 4.7. A distinctive feature of the orbit is the double-loop geometry in the vicinity of Titan [42]. The unstable eigenvalue associated with the orbit possesses a magnitude of 290.5564, indicative of the instability of the orbit. Therefore, it is relevant to investigate the invariant manifolds associated with the orbit for transfers to other periodic orbits.

Table 4.7. Initial Conditions and Jacobi Constant Value for the 5:6 Resonant Orbit in the Saturn-Titan System.

| $x$ $[nd]$ | $\dot{y}$ $[nd]$ | $C$ | Period $[nd]$ |
|---|---|---|---|
| 1.0905 | $-0.1621$ | 3.0013 | 42.9871 |

To compute the manifolds, the orbit is discretized into $10,000$ fixed points. Using a step-off value of 40 $km$, the stable and unstable manifolds for each fixed point along the orbit are propagated for $\tau = 100$ [nd], that is, 253.7879 $days$. A Poincaré section for manifold crossings is then constructed with the hyperplane $\Sigma$ defined at $y = 0$. The values of $x$ and $\dot{x}$ at each return to the hyperplane are recorded. Since the problem

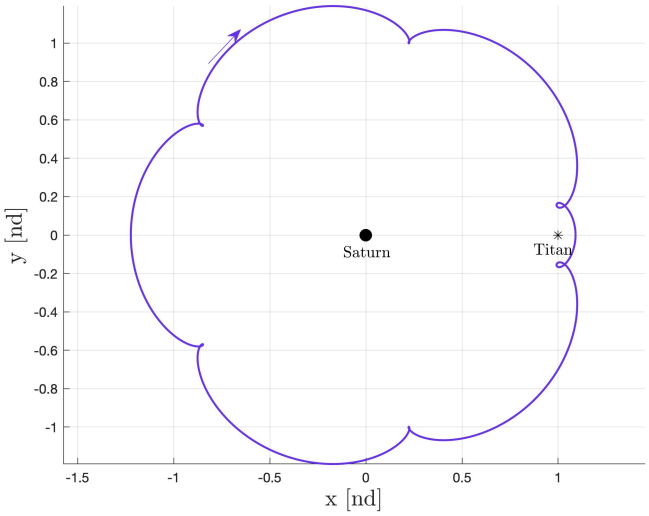


Figure 4.6. Double-Loop 5:6 Resonant Orbit in the Saturn-Titan System.

is planar, $z_0$ and $\dot{z}_0$ are zero. Recall that the value of the Jacobi constant is fixed for the map, allowing the computation of the only remaining unknown in the problem, $\dot{y}$. Figure 4.7 illustrates the Poincaré section produced for the returns of the invariant manifolds associated with the 5:6 resonant orbit. Magenta corresponds to the returns of unstable manifold, and blue represents the returns of the stable manifold. The black curves highlight the bounds that restrict the motion at this value of the Jacobi constant. Note that the map is double-sided, that is, both positive and negative returns to the map are represented.

In the design of trajectories that depart from the resonant 5:6 orbit along invariant manifolds, the arrival orbit must possess the same value of the Jacobi constant as the resonant orbit. Consider, then, the $L_1$ and $L_2$ Lyapunov orbits in the Saturn-Titan system at $C = 3.0013$. The orbits are illustrated in Figure 4.8. The $L_1$ Lyapunov orbit is plotted in purple; the $L_2$ Lyapunov orbit appears in green. The orbital parameters for the two orbits are summarized in Table 4.8. The unstable eigenvalue of the $L_1$ orbit has a magnitude of 220.4960, and that of the $L_2$ orbit is nearly the same at a magnitude of 205.0309. The computation of manifolds for these orbits and the subsequent Poincaré mapping of the manifolds reveals a structure that is similar

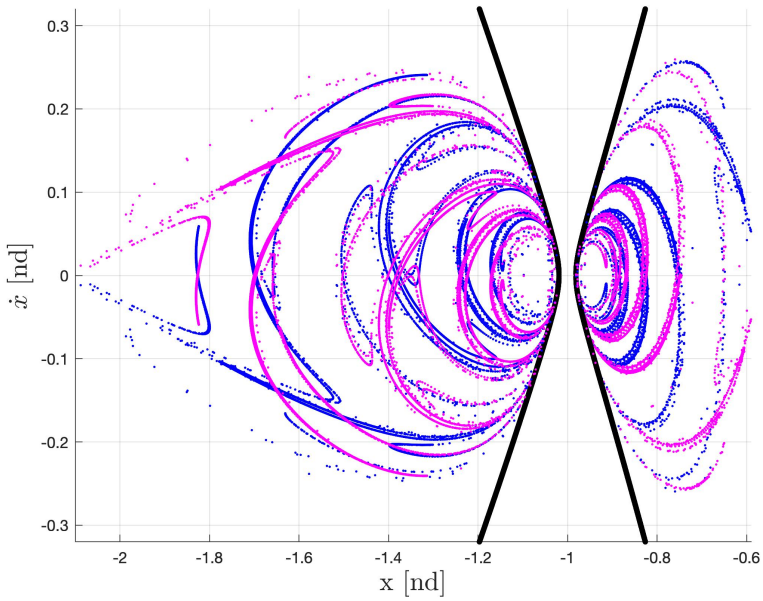


(a) $x < 0$

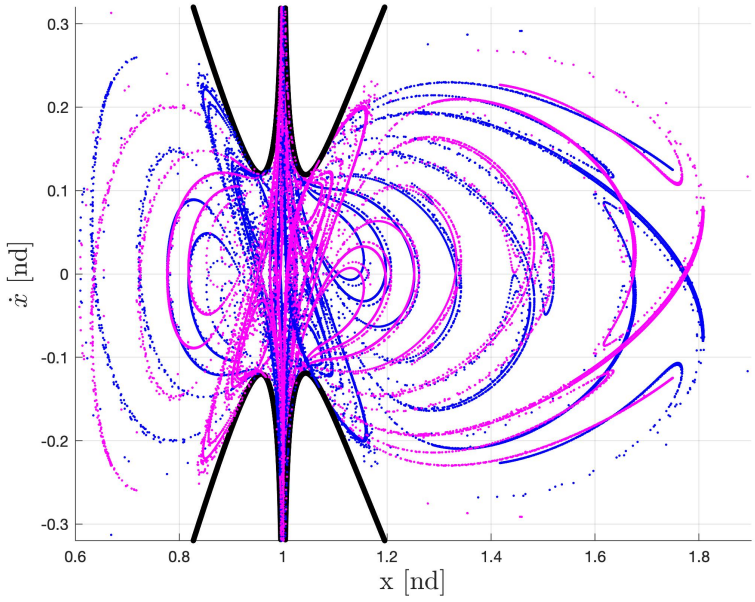


(b) $x > 0$

Figure 4.7. Poincaré Map for the Stable Manifolds (Blue) and Unstable Manifolds (Magenta) of the 5:6 Resonant Orbit in the Saturn-Titan System.

to the 5:6 resonant orbit manifolds [41]. Therefore, it is reasonable to search for invariant manifolds that result in natural transitions from the 5:6 resonant orbit to these libration point orbits.

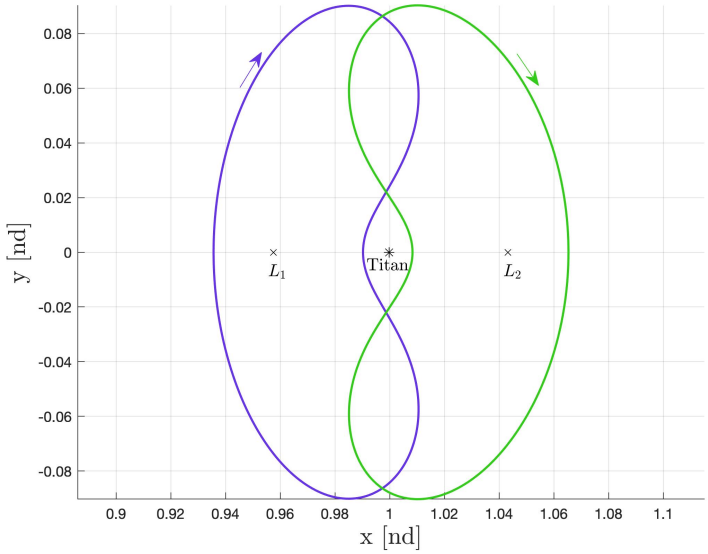


Figure 4.8. $L_1$ and $L_2$ Lyapunov Orbits at $C = 3.0013$ in the Saturn-Titan System.

Table 4.8. Initial Conditions and Jacobi Constant Values for the $L_1$ and $L_2$ Lyapunov Orbits in the Saturn-Titan System.

| **Orbit** | $\boldsymbol{x}$ **[nd]** | $\boldsymbol{\dot{y}}$ **[nd]** | $\boldsymbol{C}$ | **Period [nd]** |
|---|---|---|---|---|
| $L_1$ Lyapunov | 0.9356 | 0.1343 | 3.0013 | 4.7470 |
| $L_2$ Lyapunov | 1.0083 | 0.2307 | 3.0013 | 4.8009 |

The Poincaré sections in Figure 4.7 are employed in the identification of a transfer arc to the Lyapunov orbits. First, the fixed points corresponding to the perpendicular $\hat{x}$-axis crossings for the arrival orbit are also plotted on the map. Then, a return on the map closest to those specified fixed points is selected and, depending on the application, propagated forwards or backwards in time. In this instance, the goal is an arc that departs the 5:6 resonant orbit and arrives at the $L_1$ or $L_2$ Lyapunov

orbits. Therefore, the points on the map corresponding to returns of the unstable manifold are the focus, since those trajectories diverge from the resonant orbit as $t \to \infty$. Once the intermediate arc is computed, a corrections scheme is applied to enforce continuity in position and velocity states along the trajectory [41].

One sample transfer scenario, from the 5:6 resonant orbit to the $L_1$ Lyapunov orbit, is plotted in Figure 4.9(a). The purple curve corresponds to the intermediate transfer arc from the unstable manifold of the resonant orbit. Figure 4.9(b) illustrates the transfer arc as it approaches Titan and the $L_1$ Lyapunov orbit. After the application of the corrections scheme, the resulting transfer is a natural, maneuver-free trajectory between the two unstable periodic orbits, with a time of flight of 45.6818 *days*. Another transfer scenario, this time from the 5:6 resonant orbit to the $L_2$ Lyapunov orbit, is illustrated in Figure 4.10. Similar to the transfer to the $L_1$ Lyapunov orbit, an unstable resonant manifold is employed to construct an intermediate transfer arc. Interestingly, the time of flight of the converged transfer trajectory is the same as the first case, i.e., 45.6818 *days*.

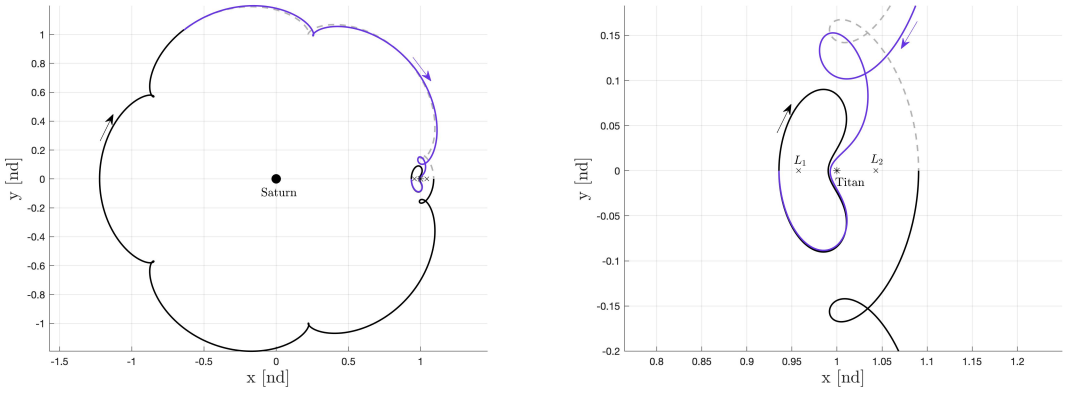


(a) Overview of the Transfer Trajectory.

(b) Trajectory in the Vicinity of Titan.

Figure 4.9. Transfer from a 5:6 Resonant Orbit to an $L_1$ Lyapunov Orbit in the Saturn-Titan System.

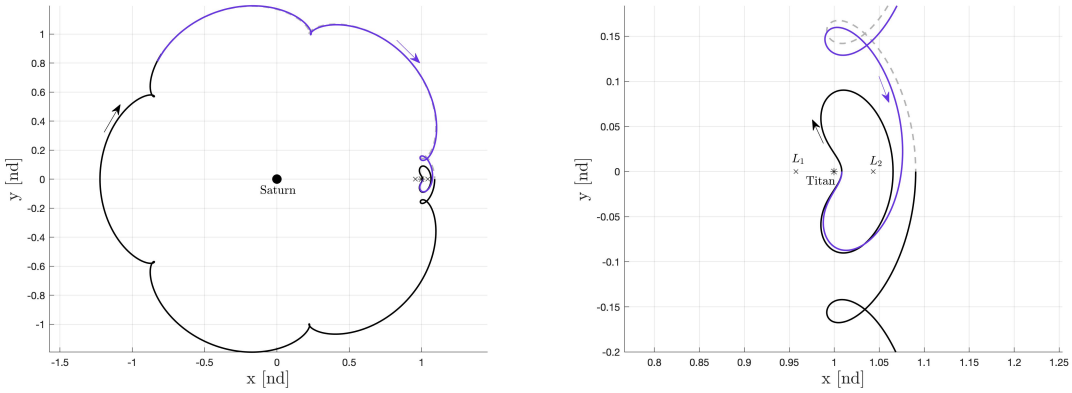


(a) Overview of the Transfer Trajectory.

(b) Trajectory in the Vicinity of Titan.

Figure 4.10. Transfer from a 5:6 Resonant Orbit to an $L_2$ Lyapunov Orbit in the Saturn-Titan System.

## 4.5 Similarities in Invariant Manifold Structure

The comparison of the invariant manifolds evolving from different periodic solutions at the same Jacobi constant value offers insight into the relationships between such periodic solutions [43], [41]. In the Saturn-Titan system, consider the resonant 3:5 and 3:4 orbits at $C = 3.0013$, that is, the Jacobi constant value at which the 5:6 resonant trajectory and the $L_1$ and $L_2$ Lyapunov orbits are available. The initial conditions and the periods associated with the 3:5 and 3:4 resonant orbits are summarized in Table 4.9. The two orbits are plotted in Figure 4.11, as viewed in the rotating frame, with the resonant 3:5 orbit represented in purple and the resonant 3:4 appearing in green. Consistent with the 5:6 resonant orbit, these orbits are also unstable. The unstable eigenvalues possess magnitudes equal to 709.6140 and 1660.3383 for the resonant 3:5 and 3:4 orbits, respectively.

For the computation of the stable and unstable manifolds of the resonant orbits, the orbits are discretized into $10,000$ fixed points spaced equally in time. The stable and unstable manifolds corresponding to each of those points are then propagated for $\tau = 100$ [nd], and their returns to the hyperplane defined by $y = 0$ are recorded. The

Table 4.9. Initial Conditions and Jacobi Constant Values for the 3:5 and 3:4 Resonant Orbits in the Saturn-Titan System.

| **Resonance** | $\boldsymbol{x}$ $[\boldsymbol{nd}]$ | $\boldsymbol{\dot{y}}$ $[\boldsymbol{nd}]$ | $\boldsymbol{C}$ | **Period** $[\boldsymbol{nd}]$ |
|---|---|---|---|---|
| 3:5 | 1.0279 | 0.1299 | 3.0013 | 31.8237 |
| 3:4 | 1.0176 | 0.1587 | 3.0013 | 25.6848 |

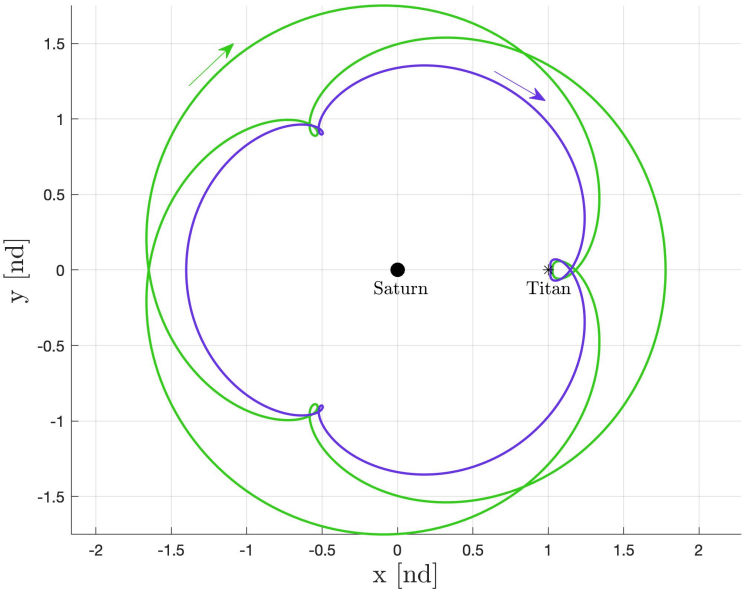


Figure 4.11. The 3:5 and 3:4 Resonant Orbits at $C = 3.0013$ in the Saturn-Titan System.

Poincaré section appears in Figure 4.12 for the manifold returns associated with the 3:5 resonant orbit, with the stable returns plotted in blue and the unstable returns plotted in pink. The section associated with the manifold returns of the 3:4 resonant orbit are then plotted in Figure 4.13, with cyan representing stable and orange reflecting unstable returns. For reference, the Poincaré sections corresponding to the manifolds of the $L_1$ and $L_2$ Lyapunov orbits are illustrated in Figures 4.14 and 4.15 as well. For the $L_1$ Lyapunov orbit, the stable returns are plotted in blue, and the unstable returns appear in gold. For the $L_2$ Lyapunov orbit, the stable returns are

plotted in green, and the unstable returns in dark red. The four Poincaré sections, along with those of the 5:6 resonant orbit illustrated in Figure 4.7, are plotted on the same axes scales for comparison. The maps expose the similarities in the manifold structures of the five orbits, as the manifolds appear to shadow each other closely in all five cases. This similarity guarantees the existence of dynamical relationships between the periodic orbits and allows for the computation of transfer trajectories and connections between these orbits with initial guesses seeded from the Poincaré sections [41], [15].

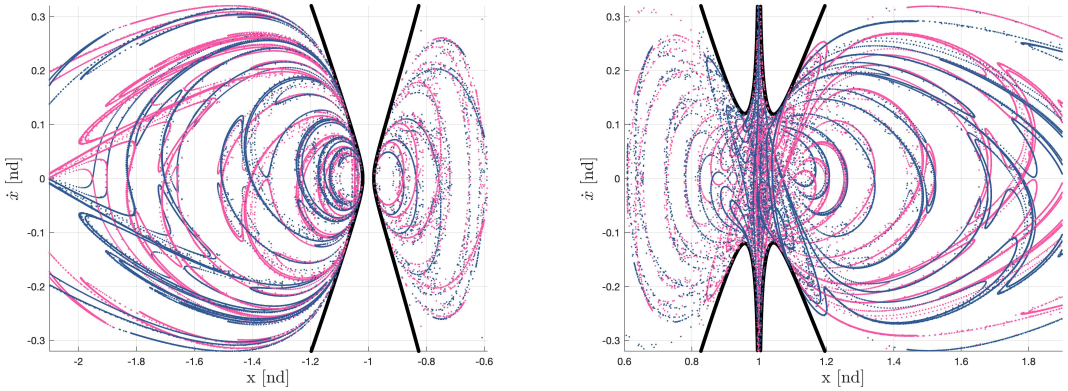


(a) $x < 0$ (b) $x > 0$

Figure 4.12. Poincaré Map for the Stable Manifolds (Blue) and Unstable Manifolds (Pink) of the 3:5 Resonant Orbit in the Saturn-Titan System.

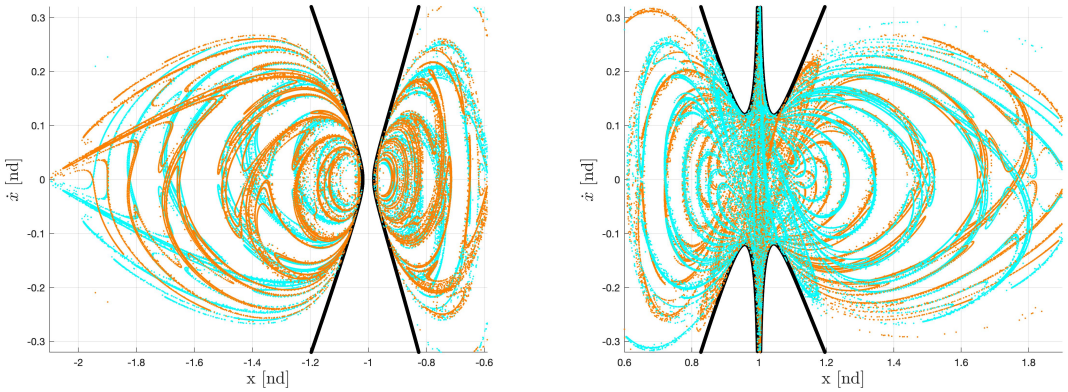


(a) $x < 0$ (b) $x > 0$

Figure 4.13. Poincaré Map for the Stable Manifolds (Cyan) and Unstable Manifolds (Orange) of the 3:4 Resonant Orbit in the Saturn-Titan System.

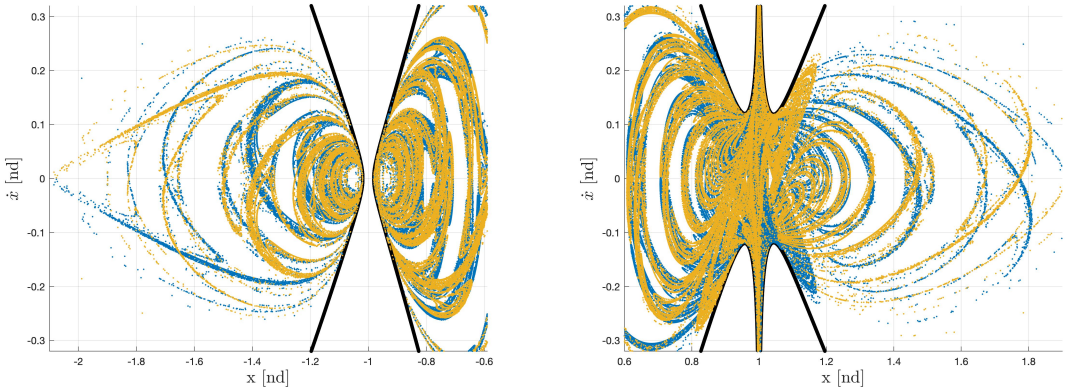


(a) $x < 0$ (b) $x > 0$

Figure 4.14. Poincaré Map for the Stable Manifolds (Blue) and Unstable Manifolds (Gold) of the $L_1$ Lyapunov Orbit in the Saturn-Titan System.

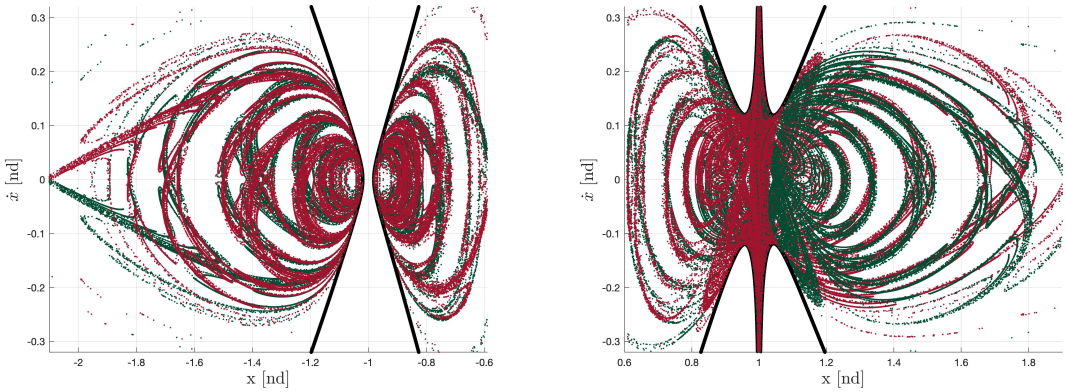


(a) $x < 0$ (b) $x > 0$

Figure 4.15. Poincaré Map for the Stable Manifolds (Green) and Unstable Manifolds (Red) of the $L_2$ Lyapunov Orbit in the Saturn-Titan System.

## 4.6 Homoclinic and Heteroclinic Connections

The computation of invariant manifolds leads to the analysis of the relationships between the stable and unstable manifolds for both the same periodic orbit or different periodic orbits in the system at the same Jacobi constant value [44]. For a periodic orbit $\Gamma$, the intersection of its unstable and stable manifolds, i.e., $W^U(\Gamma) \cap W^S(\Gamma)$, is defined as a *homoclinic connection*. When propagated in both forward and reverse time, a homoclinic connection approaches the orbit itself. Alternatively, the intersection of the stable and unstable manifolds for two different orbits is termed a *heteroclinic connection*. For two distinct periodic orbits denoted $\Gamma_1$ and $\Gamma_2$, a heteroclinic connection is represented as $W^U(\Gamma_1) \cap W^S(\Gamma_2)$, or $W^U(\Gamma_2) \cap W^S(\Gamma_1)$, and is a trajectory that approaches one orbit in forward time and the other orbit in reverse time. Heteroclinic connections offer natural, maneuver-free transfers between two periodic orbits at the same Jacobi constant value. In this investigation, Poincaré sections are leveraged for the identification of homoclinic and heteroclinic connections.

### 4.6.1 Homoclinic Connections in the Saturn-Titan System

Homoclinic connections in the Saturn-Titan system are computed employing Poincaré mapping. Consider the Poincaré section for the resonant 3:5 orbit, illustrated in Figure 4.12. There exist multiple intersections of the stable and unstable manifolds, implying the existence of homoclinic connections to/from the resonant orbit. At a point of intersection between the manifolds, the stable manifold is propagated in backward time and the unstable manifold in forward time until the trajectories intersect the 3:5 resonant orbit [3]. The initial conditions and orbital parameters for the homoclinic connection are listed in Table 4.10. Figure 4.16 illustrates the homoclinic connection plotted in the Saturn-Titan rotating frame. The asymptotic departure from the 3:5 resonant orbit is plotted in Figure 4.16(a), while Figure 4.16(b) represents the asymptotic arrival to the 3:5 resonant orbit. In both the cases, the resonant 3:5 orbit is also plotted in black, and the initial and final positions are indicated by

black stars. The complete trajectory is corrected for continuity in position and velocity at the initial and final points along each manifold arc, and the resulting homoclinic trajectory appears in Figure 4.16(c).

Table 4.10. Initial Conditions and Jacobi Constant Value for the 3:5 Resonant Homoclinic Connection in the Saturn-Titan System.

| $x$ $[nd]$ | $\dot{y}$ $[nd]$ | $C$ | Period $[nd]$ |
|---|---|---|---|
| $-2.1046$ | 1.5423 | 3.0013 | 44.2305 |

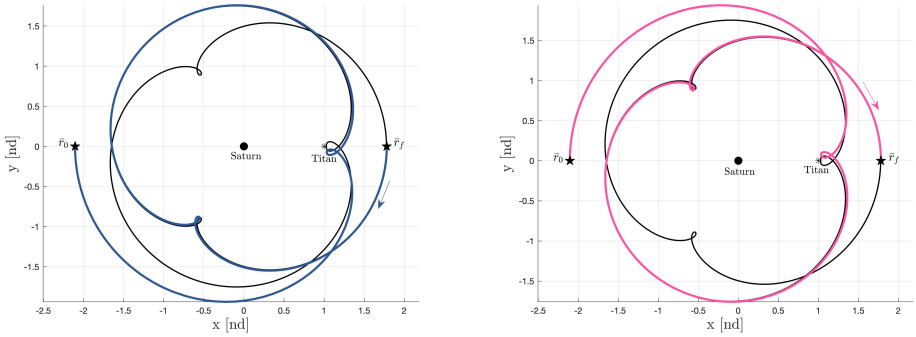


(a) Stable Manifold Propagated in Backward Time.

(b) Unstable Manifold Propagated in Forward Time.

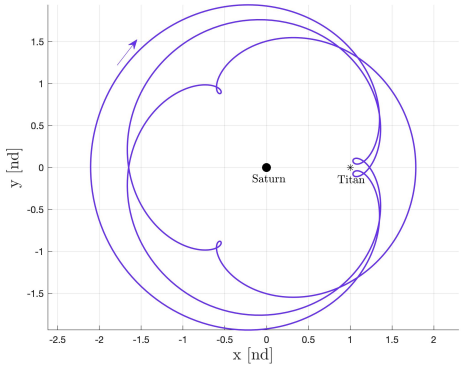


(c) Corrected Homoclinic Trajectory.

Figure 4.16. Homoclinic Connection for the 3:5 Resonant Orbit in the Saturn-Titan System.

### 4.6.2 Heteroclinic Connections in the Saturn-Titan System

Poincaré sections are leveraged in the computation of heteroclinic connections as well. Recall that a heteroclinic connection is constructed from the intersection of the unstable manifold of one orbit with the intersection of the stable manifold along a different periodic orbit [13]. To achieve such a connection, consider the Poincaré section for the unstable manifold of the 3:4 resonant orbit and the stable manifold for the 5:6 resonant orbit. The resulting Poincaré section is illustrated in Figure 4.17, with orange representing the unstable manifold returns of the 3:4 resonant orbit and blue indicating the stable manifold returns of the 5:6 resonant orbit. The map exposes several intersections of the stable and unstable manifolds and therefore, heteroclinic connections between the two resonant orbits are likely available. Again, a point of intersection of the manifolds is selected from the map. The unstable manifold is then propagated backward in time until the trajectory intersects the resonant 3:4 orbit, and the stable manifold is propagated forward in time until the trajectory intersects the resonant 5:6 orbit [15]. The trajectory is corrected for continuity in position and velocity at the initial and final states along the two orbits. The resulting heteroclinic trajectory, that is, a natural, maneuver-free transfer from the resonant 3:4 to the resonant 5:6 orbit, is illustrated in Figure 4.18. The time of flight of the transfer is 125.3712 *days*.

## 4.7 Resonant Orbit Chains

Homoclinic connections, in some cases, suggest chains of periodic orbits that traverse extensively throughout a system [45], [41]. Similar to periodic orbit families, such orbit chains exist in families as well. To construct a periodic orbit chain, a homoclinic connection to a periodic orbit is first identified. If the homoclinic connection exists near the fixed point of a different periodic orbit, an orbit chain linking the two periodic orbits is determined via differential corrections. Since the focus of this study is resonant orbits, chains of resonant orbits are investigated.

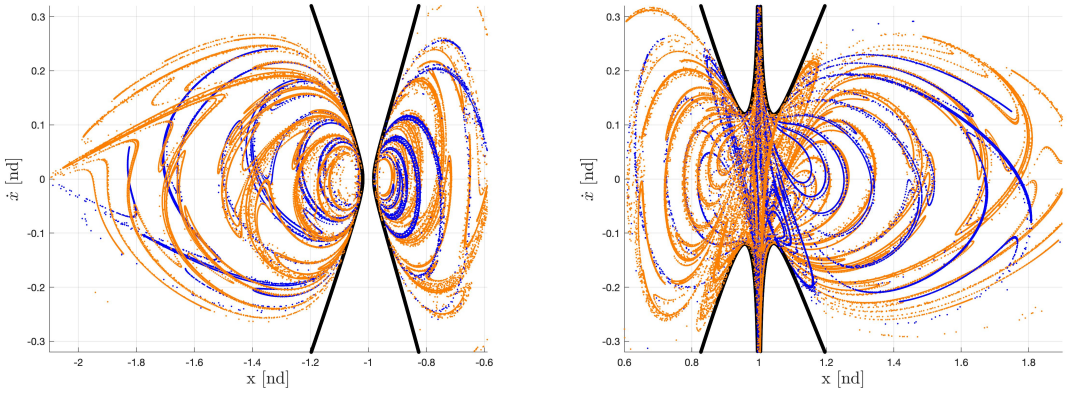


(a) $x < 0$ (b) $x > 0$

Figure 4.17. Poincaré Map for the Stable Manifolds (Blue) of the 5:6 Resonant Orbit and the Unstable Manifolds (Orange) of the 3:4 Resonant Orbit.

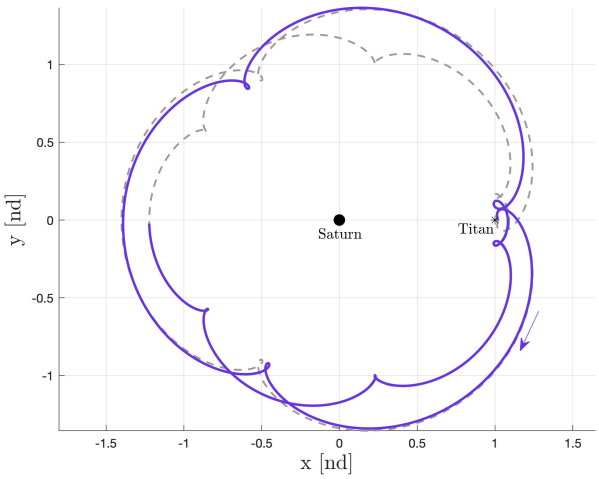


Figure 4.18. Heteroclinic Connection between the 3:4 and the 5:6 Resonant Orbits in the Saturn-Titan System.

Recall the Poincaré section for the resonant 3:4 orbit in the Saturn-Titan system, as plotted in Figure 4.13. There exist several intersections of the stable and unstable manifolds of the orbit, some that pass through the interior region of the system. Selecting one such intersection and propagating the state forward and backward in time yields a homoclinic connection to the 3:4 resonant orbit. Let the homoclinic

connection, in this case, be an intersection close to the fixed point corresponding to the resonant 9:8 orbit. The fixed point, along with the closest homoclinic connection, are illustrated in Figure 4.19. Consequently, the homoclinic connection passes through the interior region of the system and appears to follow the geometry of the 9:8 resonant orbit. Such behavior is illustrative of a periodic orbit chain that shadows the dynamics of its original orbits [41]. The resulting homoclinic trajectory is illustrated in Figure 4.20, where the orange trajectory corresponds to the unstable manifold arc, and the cyan curve represents the stable manifold arc. The grey curve serves to identify the zero velocity curve at this value of the Jacobi constant, i.e., $C = 3.0013$. The unstable and stable trajectory arcs are together corrected for continuity in position and velocity, resulting in a continuous periodic orbit chain that cycles between two different resonance ratios, 3:4 and 9:8. This orbit is a resonant orbit chain, and because the underlying trajectory originates from a homoclinic connection, it is termed a *homoclinic-type* resonant orbit chain. The orbital parameters, the Jacobi constant value, and the period of the orbit are summarized in Table 4.11. Following the methodology behind the computation of families of planar resonant orbits, families of this resonant orbit chain are also computed. Figure 4.21(a) illustrates members of the same family that also includes the periodic orbit chain. In a zoomed view, the evolution of the family in the vicinity of Titan appears in Figure 4.21(b). The orbits in the family are colored according to their Jacobi constant value.

Table 4.11. Initial Conditions and Jacobi Constant Value for the 3:4 Resonant Homoclinic Connection in the Saturn-Titan System.

| $x$ $[nd]$ | $\dot{y}$ $[nd]$ | $C$ | Period $[nd]$ |
|---|---|---|---|
| $-1.3993$ | 0.6214 | 3.0013 | 68.6009 |

Another example of a homoclinic-type resonant orbit chain in the Saturn-Titan system arises from a homoclinic connection for the 3:5 resonant orbit. Leveraging the Poincaré section for the orbit, illustrated in Figure 4.12, homoclinic connections are identified. A homoclinic connection close to a fixed point corresponding to the

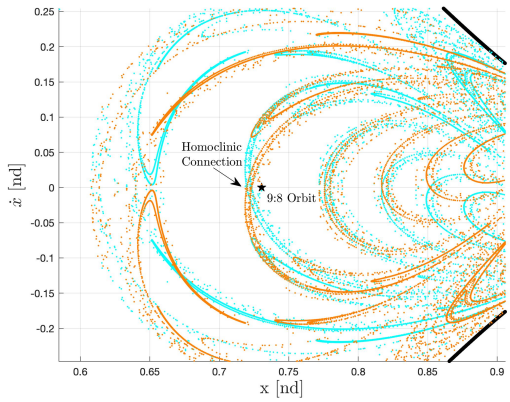


Figure 4.19. Poincaré Section for the Stable and Unstable Manifolds of the 3:4 Resonant Orbit with the Fixed Point for the 9:8 Resonant Orbit.

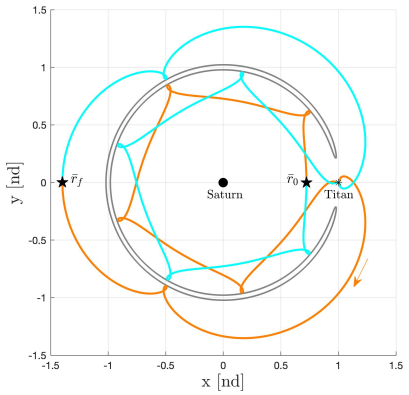


(a) Overview of the Homoclinic Connection.

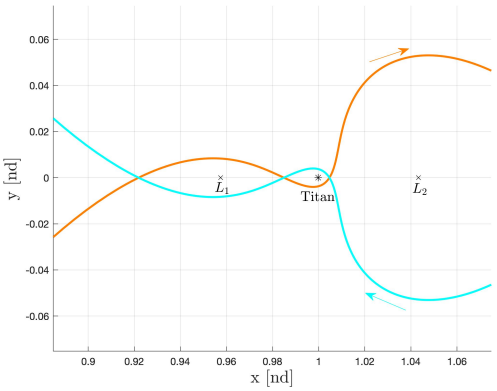


(b) Trajectory in the Vicinity of Titan.

Figure 4.20. Homoclinic Connection for the 3:4 Resonant Orbit in the Saturn-Titan System.

perpendicular crossing of an 9:10 resonant orbit is selected, as illustrated in Figure 4.22. Consistent with the previous case, the resulting homoclinic trajectory traces out the geometry of the exterior 9:10 orbit in connecting the resonant 3:5 orbit to itself. The trajectory, plotted in Figure 4.23, follows the unstable manifold as well as the stable manifold of the 3:5 resonant orbit, in pink and blue, respectively. The corrected homoclinic-type resonant orbit chain cycles between the 3:5 and 9:10 resonant orbits. The initial conditions, the Jacobi constant value, and the period for the periodic

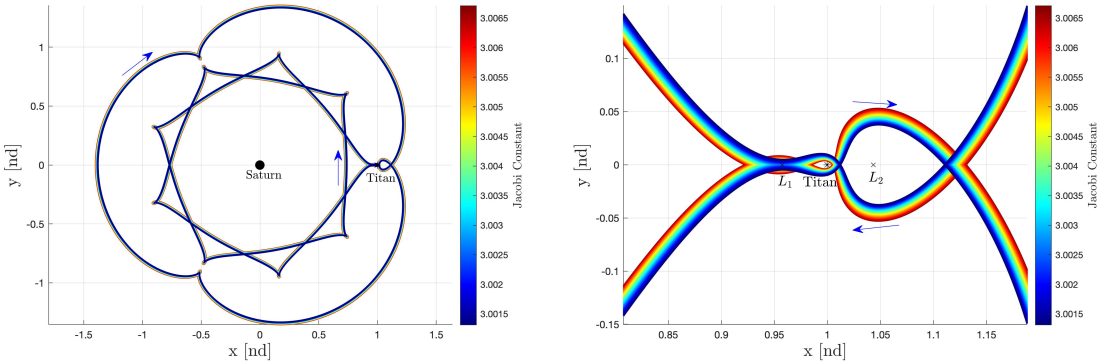


(a) Representative Members from the Orbit Family.

(b) Orbits in the Vicinity of Titan.

Figure 4.21. Family of the 3:4-9:8 Resonant Orbit Chain in the Saturn-Titan System.

orbit chain appear in Table 4.12. In this case as well, employing natural parameter continuation, a family of periodic orbit chains is computed. Figure 4.24 illustrates some members of the resulting family, with each orbit colored according to its value of Jacobi constant.

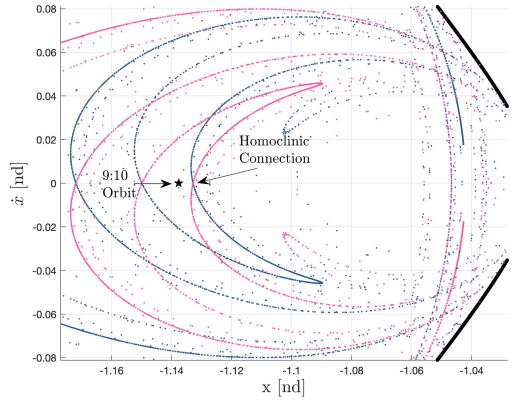


Figure 4.22. Poincaré Section for the Stable and Unstable Manifolds of the 3:5 Resonant Orbit with the Fixed Point for the 9:10 Resonant Orbit.

Table 4.12. Initial Conditions and Jacobi Constant Value for the 3:5 Resonant Homoclinic Connection in the Saturn-Titan System.

| $x$ $[nd]$ | $\dot{y}$ $[nd]$ | $C$ | Period $[nd]$ |
|---|---|---|---|
| 1.7697 | −1.1229 | 3.0013 | 93.8197 |

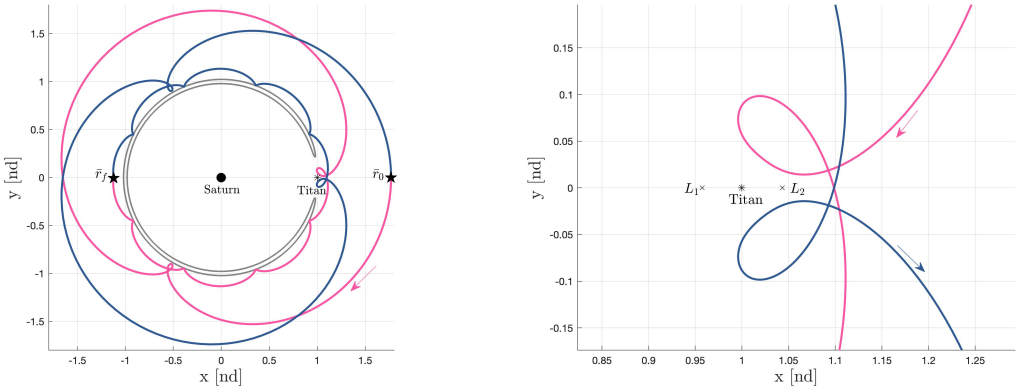


(a) Overview of the Homoclinic Connection.

(b) Trajectory in the Vicinity of Titan.

Figure 4.23. Homoclinic Connection for the 3:5 Resonant Orbit in the Saturn-Titan System.

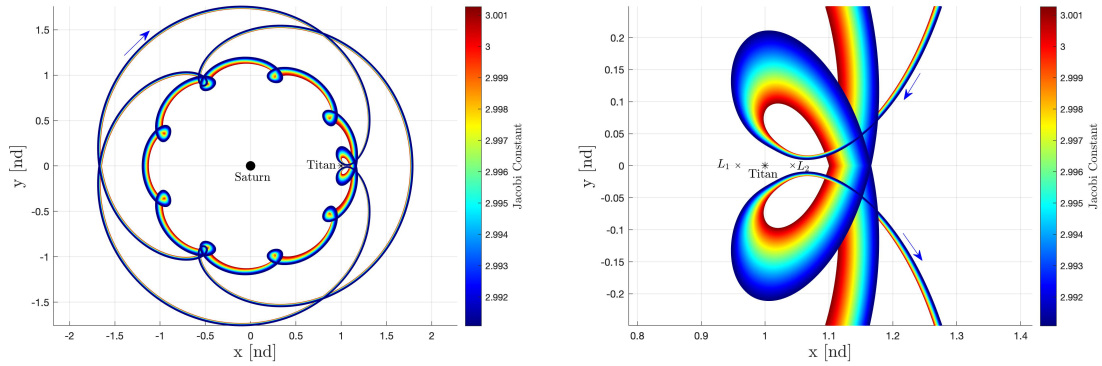


(a) Representative Members from the Orbit Family.

(b) Orbits in the Vicinity of Titan.

Figure 4.24. Family of the 3:5-9:10 Resonant Orbit Chain in the Saturn-Titan System.

# 5. CONCLUDING REMARKS

## 5.1 Summary

The focus of this investigation is an analysis of resonant orbits and their associated properties for incorporation into future mission scenarios. Although the original foundation for resonant orbits is the two-body problem, this work expands the basis for resonant orbits. Specifically, the dynamics of resonant orbits in the higher-fidelity Circular Restricted Three-Body Problem (CR3BP) are detailed in various planet-moon systems in the solar system. The tools and techniques necessary to explore periodic orbits in the CR3BP are developed, and their functionality, specifically within the context of resonant orbits, is illustrated via demonstrative examples. Resonant orbits that exhibit both stable and unstable behaviors, are leveraged for the appropriate applications.

The first objective of this investigation is the characterization and cataloging of resonant orbits in various systems within a multi-body environment. To meet this objective, the CR3BP is first introduced. The underlying assumptions, equations of motion, and the mathematical framework for the computation of equilibrium solutions in the CR3BP are detailed. Dynamical tools that offer additional insight into the properties of motion in the CR3BP, such as zero velocity surfaces and zero velocity curves, are illustrated in the Earth-Moon system. Next, numerical methods, namely, single shooting algorithms and natural parameter continuation are employed in the determination of periodic solutions in the CR3BP. Coordinate transformations that allow visualization of orbital motion in the inertial and rotating frames are also detailed. These tools are then implemented in the computation of resonant orbits. Since the two-body model serves as a first introduction to resonance, resonant orbits are first computed in this model in the Earth-Moon system. Those solutions are then

translated into the CR3BP, and families of planar resonant orbits are constructed and catalogued. Then, the stability properties of such orbits are explored for the determination of spatial resonant orbit families in the CR3BP. Therefore, the primary objective of this investigation is met via the application of the dynamical systems theory.

The second objective of this investigation is the representation of resonant orbits and their invariant manifolds as efficient tools in the design of transfer trajectories. An observation regarding the extensive reach of orbits for various different resonances in several CR3BP systems is useful. This feature of resonant orbits is leveraged in the selection of intermediate arcs for transfer between non-resonant orbits. Suitable resonant arcs are incorporated into transfer trajectories for relatively low maneuver costs in the Earth-Moon system. In another application, resonant orbits are exploited for the design of a tour of the Mars-Deimos system. Given the benefits of resonant orbits for trajectory design, techniques to reduce the cost of transfers between periodic orbits in the CR3BP are pursued via the application of Poincaré sections and invariant manifold arcs. Low cost and, in some cases, free transfer scenarios emerge after leveraging the properties of resonant orbits. Therefore, the second objective of this investigation is met with the utilization of resonant orbits and their invariant manifolds for transfer trajectory design.

The final aim of this investigation is to incorporate Poincaré sections associated with resonant orbit manifolds into the search for novel trajectories in the CR3BP. Poincaré sections are, first, utilized for the visualization of the global dynamics of the stable and unstable manifolds for various different resonant orbits. This concept is demonstrated within the context of the Saturn-Titan system for both resonant and non-resonant orbits. The similarity in structure of the resulting Poincaré sections is noted, and relationships between different orbits are obtained. The concept of homoclinic trajectories obtained via Poincaré mapping is illustrated for various resonant orbits in the Saturn-Titan system. The existence of natural, maneuver-free transfers between resonant orbits is validated. Finally, families of periodic orbits that cycle

between multiple different resonances are computed for different sets of resonance ratios.

## 5.2 Recommendations for Future Work

The techniques exploited in this investigation lay the groundwork for the further incorporation of resonant orbits into trajectory design. Specifically, such orbits that traverse throughout numerous CR3BP systems are available to be exploited in the design of trajectories that are valuable for various additional mission scenarios. One such area of exploration is the further incorporation of resonant orbits for the design of tours in the Mars-Deimos system, with added mission constraints, including but not limited to flybys of the Martian moon Phobos. Another area of exploration within the context of resonant orbits is Poincaré mapping of the manifolds associated with spatial resonant orbits, and the subsequent incorporation of resulting trajectories into low cost transfer scenarios between spatial periodic orbits. A methodology of system translation for easier computation of resonant orbits in different planet-moon systems within the CR3BP is also warranted.

# REFERENCES


[1] Jon A. Sims. Jupiter Icy Moons Orbiter Mission Design Overview. *16th AAS/AIAA Space Flight Mechanics Conference*, 2006.

[2] National Aeronautics and Space Administration. Planetary Science Decadal Survey: Jupiter Europa Orbiter Component of EJSM, 2010.

[3] Mar Vaquero. Poincaré Sections and Resonant Orbits in the Restricted Three-Body Problem. M.S. Thesis, Purdue University, West Lafayette, Indiana, 2010.

[4] Rodney L. Anderson. *Low Thrust Trajectory Design for Resonant Flybys and Captures Using Invariant Manifolds*. Ph.D. Dissertation, University of Colorado, Boulder, Colorado, 2005.

[5] Donald J. Dichmann, Ryan Lebois, and John P. Carrico. Dynamics of Orbits Near 3:1 Resonance in the Earth-Moon System. *The Journal of the Astronautical Sciences*, 60(1):51–86, 2013.

[6] Joseph W. Gangestad, Gregory A. Henning, Randy Persinger, and George R. Ricker. A High Earth, Lunar Resonant Orbit for Lower Cost Space Science Missions. In *Advances in the Astronautical Sciences*, 2014.

[7] Donald J. Dichmann, Joel J.K. Parker, Trevor W. Williams, and Chad R. Mendelsohn. Trajectory Design for the Transiting Exoplanet Survey Satellite. *International Symposium on Space Flight Dynamics*, 2014.

[8] Cody Short, Kathleen Howell, Amanda Haapala, and Donald Dichmann. Mode Analysis for Long-Term Behavior in a Resonant Earth-Moon Trajectory. In *Advances in the Astronautical Sciences*, 2016.

[9] Carl D. Murray and Stanley F. Dermott. *Solar System Dynamics*. Cambridge University Press, 2000.

[10] Isaac Newton. *Philosophiae naturalis principia mathematica*. Jussu Societatis Regiae ac Typis Josephi Streater, 1687.

[11] Victor Szebehely. Theory of Orbits: The Restricted Problem of Three Bodies. *American Journal of Physics*, 1968.

[12] Edward Belbruno and Brian G. Marsden. Resonance Hopping in Comets. *Astronomical Journal*, 1997.

[13] Wang Sang Koon, Martin W. Lo, Jerrold E. Marsden, and Shane D. Ross. Heteroclinic Connections between Periodic Orbits and Resonance Transitions in Celestial Mechanics. *Chaos: An Interdisciplinary Journal of Nonlinear Science*, 10(2):427–469, 2000.

[14] K. C. Howell, B. G. Marchand, and M. W. Lo. Temporary Satellite Capture of Short-Period Jupiter Family Comets from the Perspective of Dynamical Systems. *Journal of the Astronautical Sciences*, 2001.

[15] Tatiana Mar Vaquero Escribano. *Spacecraft Transfer Trajectory Design Exploiting Resonant Orbits in Multi-Body Environments*. Ph.D. Dissertation, Purdue University, West Lafayette, Indiana, 2013.

[16] Anish Vutukuri. Spacecraft Trajectory Design Techniques Using Resonant Orbits. M.S. Thesis, Purdue University, West Lafayette, Indiana, 2018.

[17] C. T. Kelley. *Iterative Methods for Optimization*. Society for Industrial and Applied Mathematics, 1999.

[18] A. E. Roy and M. W. Ovenden. On the Occurrence of Commensurable Mean Motions in the Solar System: The Mirror Theorem. *Monthly Notices of the Royal Astronomical Society*, 1955.

[19] Michel Hénon. *Generating Families in the Restricted Three-Body Problem*, volume 1. Springer-Verlag, 1997.

[20] Renu Malhotra. Orbital Resonances and Chaos in the Solar System. *Solar System Formation and Evolution: ASP Conference Series*, 149(iii):37, 1998.

[21] A Lemaître. High-Order Resonances in the Restricted Three-Body Problem. *Celestial Mechanics*, 32:109–126, 1983.

[22] Emily Zimovan. Characteristics and Design Strategies for Near Rectilinear Halo Orbits within the Earth-Moon System. M.S. Thesis, Purdue University, West Lafayette, Indiana, 2017.

[23] Elis Strömgren. Eine Klasse unsymmetrischer librationsähnlicher periodischer Bahnen im Probleme Restreint und ihre Entwicklungsgeschichte (Klasse n). *Copenhagen Obs.*, 94, 1934.

[24] Aurel Wintner. Grundlagen einer Genealogie der periodischen Bahnen im restringierten Dreikörperproblem. *Mathematische Zeitschrift*, 34:321–402, 1931.

[25] Thomas S. Parker and Leon O. Chua. Practical Numerical Algorithms for Chaotic Systems. *Mathematics of Computation*, 1989.

[26] Natasha Bosanac. *Leveraging Natural Dynamical Structures to Explore Multi-Body Systems*. Ph.D. Dissertation, Purdue University, West Lafayette, Indiana, 2016.

[27] Daniel Grebow. Generating Periodic Orbits in the Circular Restricted Three-Body Problem with Applications to Lunar South Pole Coverage. M.S. Thesis, Purdue University, West Lafayette, Indiana, 2006.

[28] Natasha Bosanac. Exploring the Influence of a Three-Body Interaction Added to the Gravitational Potential Function in the Circular Restricted Three-Body Problem: A Numerical Frequency Analysis. M.S. Thesis, Purdue University, 2012.

[29] Mar Vaquero and Kathleen C. Howell. Design of Transfer Trajectories between Resonant Orbits in the Earth-Moon Restricted Problem. *Acta Astronautica*, 2014.

[30] Brian T. Barden. *Using Stable Manifolds to Generate Transfers in the Circular Restricted Problem of Three Bodies*. Ph.D. Dissertation, Purdue University, West Lafayette, Indiana, 1994.

[31] Lawrence Perko. *Differential Equations and Dynamical Systems*. Springer-Verlag, New York, 1991.

[32] John Guckenheimer and Philip Holmes. Nonlinear Oscillations Dynamical Systems, and Bifurcations of Vector Fields. *Journal of Applied Mechanics*, 1983.

[33] K. C. Howell. Three-Dimensional, Periodic, 'Halo' Orbits. *Celestial Mechanics*, 32:53–71, 1984.

[34] H. Poincaré. *Les Méthodes Nouvelles de la Mécanique Céleste*. Gauthier-Villars, 1893.

[35] Matthew Bolliger. Cislunar Mission Design: Transfers Linking Near Rectilinear Halo Orbits and the Butterfly Family. M.S. Thesis, Purdue University, 2019.

[36] David C. Folta, Natasha Bosanac, Davide Guzzetti, and Kathleen C. Howell. An Earth-Moon System Trajectory Design Reference Catalog. *Advances in the Astronautical Sciences*, 153:191–210, 2015.

[37] Amanda F. Haapala, Mar Vaquero, Thomas A. Pavlak, Kathleen C. Howell, and David C. Folta. Trajectory Selection Strategy for Tours in the Earth-Moon System. In *Advances in the Astronautical Sciences*, 2014.

[38] Jordi Casoliva, Josep M. Mondelo, Benjamin F. Villac, Kenneth D. Mease, Esther Barrabes, and Merce Olle. Two Classes of Cycler Trajectories in the Earth-Moon System. *Journal of Guidance, Control, and Dynamics*, 2010.

[39] Ryan P. Russell and Nathan J. Strange. Cycler Trajectories in Planetary Moon Systems. *Journal of Guidance, Control, and Dynamics*, 2009.

[40] Kathryn E. Davis, Rodney L. Anderson, Daniel J. Scheeres, and George H. Born. The use of invariant manifolds for transfers between unstable periodic orbits of different energies. *Celestial Mechanics and Dynamical Astronomy*, 107:471–485, 2010.

[41] Mar Vaquero and Kathleen C. Howell. Transfer Design Exploiting Resonant Orbits and Manifolds in the Saturn-Titan System. *Journal of Spacecraft and Rockets*, 2013.

[42] Rodney L. Anderson, Stefano Campagnola, and Gregory Lantoine. Broad Search for Unstable Resonant Orbits in the Planar Circular Restricted Three-Body Problem. *Celestial Mechanics and Dynamical Astronomy*, 124(2):177–199, 2016.

[43] Rodney L. Anderson. Approaching Moons from Resonance via Invariant Manifolds. *Journal of Propulsion and Power*, 31(5):1097–1109, 2015.

[44] Wayne Schlei. *Interactive Spacecraft Trajectory Design Strategies Featuring Poincaré Map Topology*. PhD thesis, Purdue University, 2017.

[45] J. S. Parker, K. E. Davis, and G. H. Born. Chaining Periodic Three-Body Orbits. *Acta Astronautica*, 67(5):623–638, 2010.